UNIVERSITY OF SOUTHAMPTON

Faculty of Physical Sciences and Engineering
Department of Physics and Astronomy

Multi-wavelength observations of Galactic black hole X-ray transients

by

Aarran Shaw

A thesis submitted in partial fulfillment for the degree of Doctor of Philosophy

October 2016

UNIVERSITY OF SOUTHAMPTON

Abstract

Faculty of Physical Sciences and Engineering
Department of Physics and Astronomy

Doctor of Philosophy

Multi-wavelength observations of Galactic black hole X-ray transients

by Aarran Shaw

Galactic black hole X-ray transients (BHXRTs) represent the ideal opportunity to study accretion physics in extreme environments. Questions relating to accretion geometry, the mass of the compact object, how transient outbursts start and how jets form and evolve can only be answered by observing BHXRTs across multiple wavelengths. In this thesis I take a multi-wavelength approach to studying BHXRTs, and attempt to reconcile many aspects of accretion physics using a number of techniques.

I have used timing analysis techniques to discover a super-orbital periodicity of ~ 420 days in the X-ray and optical light curves of the BHXRT Swift J1753.5-0127, whilst also uncovering the likely orbital period of the candidate BHXRT MAXI J1305-704. X-ray spectral observations of Swift J1753.5-0127 revealed its first ever transition to a soft accretion state. This was found to be one of the lowest luminosity soft states ever recorded in such a system, at $< 1\%$ the Eddington luminosity, which proved crucial in the subsequent radio observations. Collaborators and I found that the compact jet had been quenched by a factor > 25, indicating that jet quenching was not dependent on accretion rate.

In the optical regime, spectroscopy can reveal details about the mass of the compact object, which is important for population studies of black holes (BHs). I place a lower limit on the mass of Swift J1753.5-0127at $M_1 > 7.4 \pm 1.2 M_{\odot}$, confirming it as a BH and removing it from the so-called 'mass gap.' However, optical observations can also reveal details about the accretion geometry of a source, as in the case of the BHXRT V404 Cyg, in which collaborators and I combined optical spectroscopy and photometry and found evidence for the 2015 outburst initiating ~ 1 week before the X-ray outburst was detected. Our results were found to be consistent with the current disc instability model for transient outbursts.

I summarise these findings and suggest avenues for future work in the closing pages of this thesis. Overall, this work shows that we can only truly understand BHXRTs once we have studied them across multiple wavelengths, and only in doing so can we discuss the underlying physics behind some of the most extreme regions of the Universe.

Contents

List of Figures

List of Tables

Declaration of Authorship

I, AARRAN SHAW, declare that this thesis titled, 'MULTI-WAVELENGTH OBSERVATIONS OF GALACTIC BLACK HOLE X-RAY TRANSIENTS' and the work presented in it are my own. I confirm that:

- This work was done wholly or mainly while in candidature for a research degree at this University.
- Where any part of this thesis has previously been submitted for a degree or any other qualification at this University or any other institution, this has been clearly stated.
- Where I have consulted the published work of others, this is always clearly attributed.
- Where I have quoted from the work of others, the source is always given. With the exception of such quotations, this thesis is entirely my own work.
- I have acknowledged all main sources of help.
- Where the thesis is based on work done by myself jointly with others, I have made clear exactly what was done by others and what I have contributed myself.
- This thesis contains work which has been previously published in the following works:
  - A. W. Shaw et al. 2013, MNRAS, 433, 740, *A 420-day X-ray/optical modulation and extended X-ray dips in the short-period transient Swift J1753.5-0127*
  - A. W. Shaw et al. 2016, MNRAS, 458, 1636, *A low-luminosity soft state in the short period black hole X-ray binary Swift J1753.5-0127*
  - F. Bernardini, D. M. Russell, A. W. Shaw et al. 2016, ApJ, 818, L5, *Events leading up to the Jun 2015 outburst of V404 Cyg*
  - A. P. Rushton, A. W. Shaw et al. 2016, MNRAS, 463, 628, *Disk-jet quenching of the Galactic black hole Swift J1753.5-0127*
  - A. W. Shaw et al. 2016, MNRAS, 463, 1314, *No evidence for a low-mass black hole in Swift J1753.5-0127*

Signed:

Date:

"You people have stood in my way long enough. I'm going to clown college!"

Homer Simpson - The Simpsons (Homie the Clown)

Acknowledgements

First and foremost, I would like to thank my supervisor, Phil Charles, for all the support and direction he has given me throughout my studies. He has allowed me freedom to develop as a graduate student, giving me the responsibility for writing and leading observing proposals and journal papers, whilst always offering his invaluable insight. I would also like to take this opportunity to thank my collaborators for their support and direction. Poshak Gandhi, Diego Altamirano and Jorge Casares stand out in particular, for without them and their insight, I would have been completely lost.

In Southampton I would like to thank the staff, postdocs, PhD students and associated wives and girlfriends for the laughs, pub trips and nights out. The past four years would not have been nearly as fun without them. In particular I'd like to thank Rob Firth, Sam Connolly, James Matthews and Keira Rowsome for being some of the greatest friends I could ever hope to have. Thanks to Andy Smith for the lifts to cricket, Stew, Mat, Boon and CFro for helping me improve my squash game significantly, Liz Bartlett for keeping me sane during times of crisis, Sadie Jones for the outreach opportunities and everybody else who has even slightly contributed to my Southampton experience.

Fred, you're an absolutely phenomenal housemate, thanks for making the last two years so much fun, and for doing all my washing up. You're always there to chat, dispense good advice, talk in multiple languages and indulge my mildly offensive Swedish caricature. I'm so happy to call you one of my best friends.

Of course, I wouldn't be here if it weren't for my family. Thank you dad for driving me to PhD interviews, driving all my belongings down to Southampton from Leeds and, of course, the constant love and support from the moment I was born. Mum, thank you for the love and support, the long distance Skype catch-up calls and for bringing me into the world. Finally, Joanna Shaw, my incredible step-mother who, unfortunately, will not be able to see this Acknowledgments page, thank you for everything. You inspired me to go to University in the first place, I would not be here if it weren't for you. Thank you for your advice, your unconditional love and for always having a gin and tonic waiting for me when I came home. I love you and I miss you.

For Jo

Chapter 1

Introduction

"Everything's in order in a black hole
Nothing seems as pretty as the past though."

Arctic Monkeys - Fluorescent Adolescent

1.1 Basic Concepts

In this thesis I will discuss multi-wavelength observations of black holes. Here I define the concept of black holes before discussing X-ray binaries and transients in more detail in sections 1.2 and 1.3. It is important to note that I define an X-ray as electromagnetic radiation in the energy range $\sim$0.1 – $\sim$100 keV and optical light in the UBVRIZ wavelength range ($\lambda\lambda$ $\sim$3000 – $\sim$10000 Å).

1.1.1 Detecting X-rays

In the long history of astronomy, the view of the Universe has mostly been a narrow one, restricted to the optical waveband for the majority of this time - the Earth's atmosphere is almost transparent to optical light and it is easy to focus with mirrors or lenses. Broadening this view has been the privilege of the last century, with advances in detector technology opening up previously unobserved wavebands in radio and infrared (IR) astronomy. The end of the space race brought with it the ability to place telescopes in orbit, removing the restrictions of the Earth's atmosphere (which absorbs the majority of high energy electromagnetic radiation) and introducing astronomers to the concept of ultraviolet (UV) and X-ray astronomy. Parallel to this, ground based optical astronomy improved at a rapid pace with the introduction of the charge-coupled device (CCD) and the construction of larger telescopes. Nowadays, astronomers have access to almost the entire electromagnetic spectrum through a suite of space and ground-based observatories, providing unparalleled coverage of astronomical objects across all wavelengths. In this section I will detail how such technological advances have improved X-ray astronomy, which was non-existent before the 1960s.

Once an X-ray telescope is placed above the atmosphere, the next problem is actually detecting the X-ray photons. X-rays interact with matter in a number of ways. In the energy range 0.1–10 keV, the main interaction mechanism is the photoelectric effect in which an atom absorbs the incoming photon and ejects an electron with energy equal to that of the photon minus the binding energy of the electron. At high energies ($\gtrsim 10$ keV), the photoelectric effect becomes less important and X-ray interactions become dominated by the process of Compton scattering. In this process, photons scatter from individual electrons and the energy of the incident X-ray is shared between the scattered photon and the electron. The electron energy depends on the scattering angle and is at a maximum when the photon is scattered back in the incident direction. The maximum energy a Compton electron can have is much higher for high energy incident photons than for low energy, which is why the process is much more efficient for high energy astrophysics.

The majority of X-ray detectors utilise the photoelectric effect in their instruments, as one can increase the photoelectric cross section (the probability of interaction) by increasing the Z (number of protons) of the absorbing material. I will provide here a brief description of the three main types of detector utilised in past and current X-ray missions: proportional counters, scintillation counters and CCDs.

Proportional counters typically consist of a gas-filled detector, at the centre of which is a wire or anode with a large (~ 2 kV) potential. Incoming photons enter the detector through a thin window and are absorbed by the gas and the resultant photoelectrons produce short tracks of ions and electrons inside the gas. The photoelectrons rapidly accelerate towards the anode, dispensing of the additional energy from acceleration through collisions with other atoms, causing further ionisation tracks and resulting in an avalanche of electrons that is collected at the anode. The number of electrons collected by the anode is recorded as a single pulse, the height of which is proportional to the energy of the incident X-ray photon and hence a proportional counter can be used for X-ray spectroscopy. Proportional counter arrays were used on *Uhuru* (Giacconi et al., 1971), *ROSAT* (Pfeffermann et al., 1987) and more recently the *Rossi X-ray Timing Explorer (RXTE)* (Glasser et al., 1994).

Scintillation counters use crystals of sodium iodide or caesium iodide, high-Z materials which can efficiently detect higher energy photons than gas-filled proportional counters.

The photon energy is absorbed by an atom in the crystal and some of the energy appears as a pulse of light known as a scintillation. The amount of light produced is proportional to the energy of the incident photon and is detected by photomultiplier tubes (PMTs) in the detector. A scintillation counter was used as the detector for the High Energy X-ray Timing Experiment on board *RXTE* (Gruber et al., 1996) as well as the high energy detector of *BeppoSAX* (Boella et al., 1997). The scintillation phenomenon can also be combined with the proportional counter concept in which a PMT detects the flash of UV light that is produced when the atoms in the gas that have been excited by the photoelectrons return to their rest energy. Such gas scintillation proportional counters (GSPCs) have been utilised on board the Japanese *ASCA* mission (Tanaka et al., 1994) and *BeppoSAX*.

By far the most common X-ray detector now is the CCD. CCDs consist of an array of millions of pixels of a high-Z material (such as silicon) which, when hit by an X-ray, produces photoelectrons. X-rays are capable of producing hundreds of photoelectrons and the total charge produced is proportional to the energy of the incident photon, allowing CCDs to be used as X-ray spectrometers. CCDs are present on the current X-ray missions *Chandra* (Weisskopf et al., 2002), *Suzaku* (Mitsuda et al., 2007) and *XMM-Newton* (Jansen et al., 2001). However, CCDs do present a problem when observing bright (e.g. > 0.7 count s^{-1} for *XMM-Newton* MOS cameras) sources in that sometimes more than one X-ray photon can reach a CCD pixel before it is read out. This has the effect of adding the energies of each photon together which registers as a single event at that total, combined energy. This is known as photon pile-up and can affect X-ray spectra of some sources. Pile-up can be accounted for by removing the central few pixels (where the majority of multi-photon events will be detected) from subsequent analysis, but it still remains a problem in modern-day X-ray astronomy (see e.g. Jethwa et al., 2015).

1.1.1.1 Finding the location of X-ray sources

To find the position of an X-ray source, one needs to accurately determine the direction from which the incident X-rays are arriving. Early X-ray missions such as *Uhuru* (Giacconi et al., 1971) utilised honeycomb shaped slat collimators which restricted the detector field of view. Early slat collimator detectors could determine the location of a source by scanning a strip of the sky in one dimension to produce a 1-d position along the strip, then scanning the sky again at a different spacecraft orientation, allowing triangulation of the source's 2-d position. Such collimators could crudely extract the location of sources on the sky but the accuracy of this positioning was dependent on the source strength and the dimensions of the collimator. Improvements to the collimator concept came with the advent of the scanning modulation collimator, in which the collimator would simply consist of two 1-d wire grids, separated by a certain distance (Oda, 1965). A source's signal would be modulated by the shadow pattern of the front wire grid on the rear grid as the spacecraft rotated, producing a modulated count rate as a function of time. The excellent time resolution of the proportional counters meant that a detector utilising a scanning modulation collimator could extract spatial information accurate to $\sim 2'$ from a temporal signal (see e.g. Ariel V; Smith & Courtier, 1976).

To obtain the greatest positional accuracy, X-rays need to be focussed with a mirror, much like in optical astronomy. Softer X-rays (up to $\sim$ 10 keV) can be focussed this way. However, the incidence angle must be small ($< 1^{\circ}$) for the reflection efficiency to be high. X-ray telescope mirrors can therefore focus X-rays to a point on a small detector at the focal point using mirrors in what is known as the Wolter type 1 configuration (Wolter, 1952). In this configuration, X-rays are first reflected from the inside of a parabolic surface before a second reflection from the inside of a hyperbolic surface on to the detector. Several Wolter mirrors are used in a nested configuration in order to collect more light and increase the effective area of the telescope. Fig. 1.1 illustrates the geometry of the mirrors in *Chandra*.

It becomes increasingly hard to reflect X-rays from a mirrored surface with increasing photon energy, making high energy X-ray imaging difficult (though not impossible, see *NuSTAR*, which can focus X-rays up to $\sim$ 79 keV; Harrison et al., 2013). Therefore to improve the location accuracy of harder ($\gtrsim$ 10 keV) X-rays the coded mask was developed. A coded mask is a sheet of absorbent material (e.g. tungsten) with a random pattern of openings which allow X-rays to cast a shadow on a position-sensitive detector (Fenimore & Cannon, 1978). The pattern cast by the X-rays on the detector is dependent on source position and is correlated with the known pattern of the coded mask to find the direction of the incident X-rays. Coded masks are in place on many large area hard X-ray detectors which scan large portions of the sky at once, such as the *Swift* Burst Alert Telescope (BAT; Barthelmy et al., 2005).

1.1.2 Optical Astronomy

Though X-ray astronomy is important for probing astronomical objects at high energies, to truly understand physics of a source, we must adopt a multi-wavelength approach. Many sources, such as the binary systems that are the subject of this thesis, emit light across the entire electromagnetic spectrum. In this thesis I mainly focus on X-rays and optical wavelengths, so here I will provide a brief introduction to techniques used in optical astronomy, in particular optical spectroscopy.

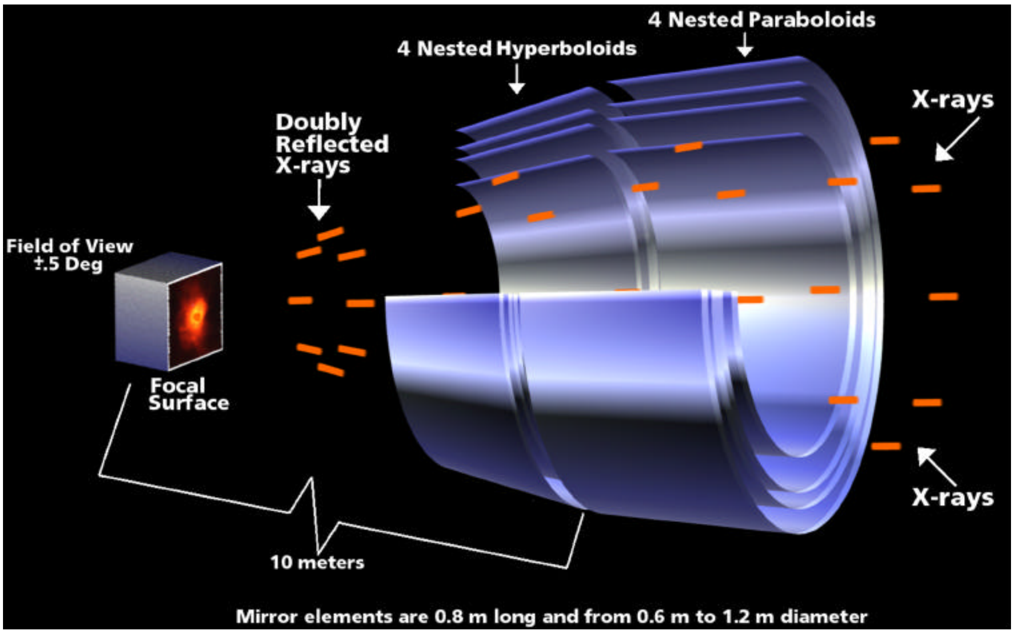

FIGURE 1.1: A schematic of the *Chandra* mirrors, illustrating the nested Wolter Type 1 configuration. X-rays are reflected from the first, parabolic mirror and then from the inner surface of the second, hyperbolic mirror before coming to a focus at the detector. Image credit NASA/CXC/D. Berry.

Whilst optical photometry can provide a measure of the flux of a star in several broad-band filters, to study the flux of the light as a function of wavelength and hence isolate individual features, we need spectroscopy. A schematic of a typical spectrograph is shown in Fig. 1.2, showing how light enters the instrument through a slit. The slit not only masks regions of the sky that are not interesting to the observer but also provides stable spectral resolution by negating variations in the astronomical seeing. The wider the slit, the worse the spectral resolution, but the higher the signal-to-noise ratio (S/N) of the spectrum, so an optimum width needs to be chosen.

The diverging light from the slit is then collimated, making it parallel, in order to evenly illuminate the diffraction grating, which splits the light into its component wavelengths according to the grating equation:

$$n\lambda = d(\sin\theta + \sin\phi) \tag{1.1}$$

where n is the order of the diffracted light, d is the grating spacing and θ and ϕ are diffraction angle and the incident angle of the beam with the grating, respectively.

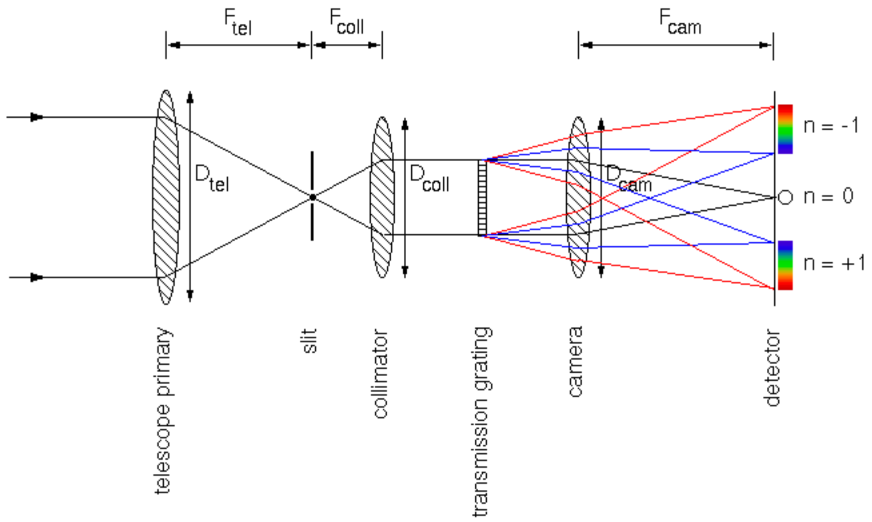

FIGURE 1.2: Schematic of a spectrograph incorporating a transmission grating. Arrows show the direction of the light through the labelled components. F_{tel}, F_{coll} and F_{cam} are the focal lengths of the telescope, the collimator and the camera, respectively. The order of the diffracted spectrum is denoted by n. Image credit Vik Dhillon.

Changing the angle of the incident light (e.g. by tilting the grating) adjusts the wavelength range of the spectrum. The resultant dispersed light is then focussed onto the CCD detector, with the direction along the slit representing the spatial axis – allowing the sky background and multiple sources to be measured – and the direction along the grating representing the dispersion, or wavelength axis.

Extracting a spectrum from a two-dimensional CCD image such as the one shown in Fig. 1.3 first requires the raw image to be corrected for CCD bias and pixel-to-pixel sensitivity of the detector (flat fielding). The spectrum is then extracted by choosing an aperture that optimally encompasses the one-dimensional profile of the spectrum in the spatial dimension, varying it as a function of wavelength so as to maximise S/N ('optimal extraction;' Horne, 1986). Sky lines are removed from the resultant one-dimensional spectrum by subtracting a background spectrum, extracted from the regions of the CCD on which no source is detected. Wavelength calibration is achieved by extracting spectra of 'arc lamps', which exhibit strong emission lines of known wavelength, and comparing the wavelengths of the emission features to their pixel values on the dispersion axis. The spectrum, now a function of wavelength, is now ready for analysis. Flux calibration can be performed by extracting the spectrum of a star, observed under the same conditions, with a very well known spectrum and flux as a function of wavelength (e.g. Oke, 1990) and comparing it to the target spectrum. However, this is not essential for studying spectral features.

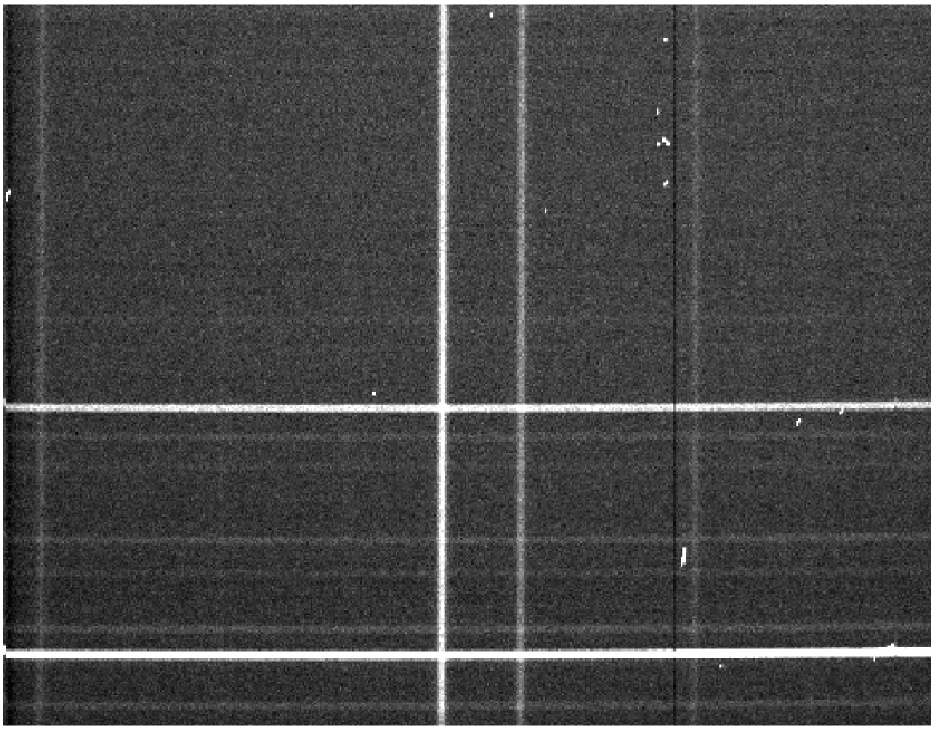

FIGURE 1.3: A two-dimensional raw spectrum of V404 Cygni. The horizontal axis is the spatial direction and the vertical axis is the dispersion axis, with wavelength increasing upwards. The target spectrum is a vertical strip near the centre of the image. Also visible are horizontal strips which represent sky emission features, and cosmic ray interactions with the detector.

1.1.3 Black Holes and Neutron Stars

During the early days of X-ray astronomy, the nature of the X-ray sources discovered was unclear. The huge X-ray power but relatively low optical flux (the brightest X-ray source in the sky, Sco X-1, has an optical magnitude of just 12) suggested a compact nature for these objects. The confirmation came with *Uhuru* observations of another bright source, Cen X-3, which uncovered 4.84 second X-ray pulsations, which could only be produced by a rapidly rotating neutron star (Schreier et al., 1972). The compact nature of these bright X-ray sources was confirmed, but the question remains, how are such objects formed?

When a massive star ($\gtrsim 8M_{\odot}$) reaches the end of its life, nuclear fusion will no longer be able to sustain the core against the influence of the star's own gravity. The subsequent collapse of the star induces a violent ejection of the star's outer layers, known as a core-collapse supernova. What remains after a supernova is dependent on the initial mass of the progenitor star, but is always a compact, degenerate stellar remnant; either a neutron star (NS) or a black hole (BH).

NSs are the smallest and densest stars known to exist in the Universe. They are composed almost entirely of neutrons and have a similar mass to that of the Sun. However, this mass is compressed to a radius of only $\sim$ 10km (Pacini, 1967). A main-sequence star with an initial mass $\gtrsim 8M_\odot$ may become a NS at the end of its life.

On the main sequence, a star generates energy in the core by fusing hydrogen to helium, but when the supply of hydrogen is depleted, the star contracts, raising the temperature high enough to fuse helium to carbon and oxygen. At the same time, the increased pressure in the core will be enough to initiate hydrogen burning in its outer layers, resulting in a shell of helium surrounding the core of heavier elements – the so-called 'horizontal branch' of the Hertzsprung-Russell diagram. At the end of this process, the star, if it is massive enough, will have a central core of iron, surrounded by onion-like layers of lighter elements and an outermost shell of hydrogen. Iron cannot be fused any further, however mass is still deposited on to the core by the fusion of the adjacent shell of silicon, causing it to exceed the Chandrasekhar mass limit:

$$M_{\text{limit}} = \frac{\omega_3^0 \sqrt{3\pi}}{2} \left(\frac{\hbar c}{G}\right)^{3/2} \frac{1}{(\mu_e m_H)^2} \text{kg} \tag{1.2}$$

(Chandrasekhar, 1931, 1935) where μ_e is the average molecular weight per electron (dependent on the chemical composition of the star), $\omega_3^0 \approx 2$ is a constant, $\hbar = 1.054 \times 10^{-34}$ J s is the reduced Planck constant, $c = 2.998 \times 10^8$ m s^{-1} is the speed of light, $G = 6.674 \times 10^{-11}$ m^3 kg^{-1} s^{-2} is the gravitational constant and $m_H = 1.674 \times 10^{-27}$ kg is the mass of a hydrogen atom. M_{limit} is the maximum mass at which *electron degeneracy pressure* can prevent the star from gravitational collapse. Electron degeneracy pressure is a manifestation of the Pauli exclusion principle which states that no more than two electrons can simultaneously occupy the same quantum state (Pauli, 1925), resulting in an outward pressure against the compression of matter. Beyond the Chandrasekhar mass limit, gravity overcomes electron degeneracy pressure and the core contracts further, causing the internal temperature to rise and some of the iron to emit alpha radiation (photodisintegration). As the temperature continues to rise, protons combine with electrons to form neutrons (electron capture) causing the pressure to drop even further. The core collapses until nuclear density is reached and is supported by neutron degeneracy pressure. The energy from the in-falling matter produces a shock which propagates outwards from the core, ejecting the material outwards in a Type II or Ib/c supernova. Only the neutron rich core remains at the centre of the explosion, which retains most of the angular momentum of the progenitor and is therefore rapidly rotating due to its much smaller radius.

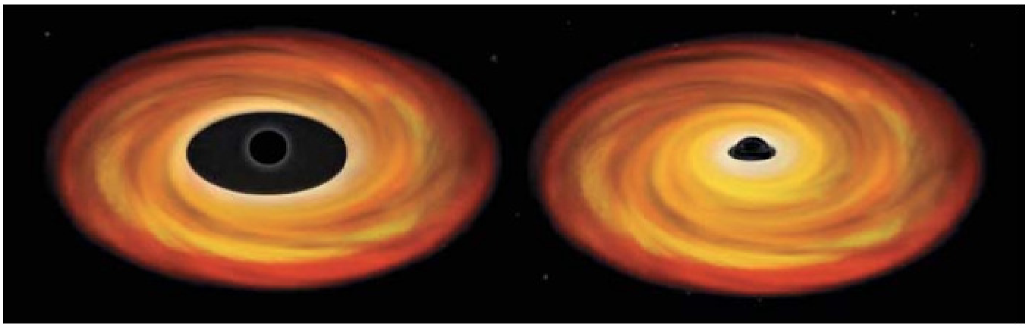

FIGURE 1.4: Schematic of the accretion disc surrounding a BH highlighting the innermost stable circular orbit. Within this radius, material must spiral rapidly into the BH. The ISCO of a non-rotating (Schwarzschild) BH (left) is located at larger radii than for a maximally rotating (Kerr) BH (right). Adapted from Seward & Charles (2010).

If the mass of the NS exceeds the Tolman-Oppenheimer-Volkoff limit ($\sim 1.5 - 3M_{\odot}$; Tolman, 1939; Oppenheimer & Volkoff, 1939) then neutron degeneracy pressure is not sufficient to prevent further collapse and the core becomes a BH. The theory of general relativity describes a BH as containing a gravitational singularity at its centre - an infinitely small (zero volume) region containing all the mass of the BH where spacetime curvature becomes infinite. Because it is not practical to refer to an infinitely small region, the size of a BH is usually defined by the Schwarzshild radius:

$$R_{\mathrm{S}} = \frac{2GM}{c^2} \tag{1.3}$$

(Schwarzschild, 1916a,b), where M is the mass of the BH. For a non-rotating (Schwarzschild) BH, R_{S} acts as a boundary, known as the Event Horizon, beyond which no information can escape and is defined as the point at which the escape velocity = c. In general relativity there exists an innermost stable circular orbit (ISCO; see Fig. 1.4), inside of which any perturbations would cause an orbiting particle to spiral into the BH. For a Schwarzschild BH, $R_{\mathrm{ISCO}} = 3R_{\mathrm{S}}$. This value decreases as the spin of the BH increases, with the ISCO of a maximally rotating (Kerr) BH calculated to be $1.24R_g$, where $R_g = \frac{R_{\mathrm{S}}}{2}$ is the gravitational radius of the BH (Fabian & Miniutti, 2005).

By their very nature, BHs do not emit any electromagnetic radiation and are therefore invisible. However, since they interact gravitationally with their surroundings, it is possible to infer the existence of BHs through indirect means. It is now thought that supermassive BHs exist at the centre of every galaxy, and the masses of a number of BHs have been measured through observations of X-ray binaries (see section 1.3.1). We have even observed the merging of two BHs through the recent detection of gravitational waves (Abbott et al., 2016), providing the scientific community with the most direct evidence for the existence of such objects to date.

1.1.4 The Eddington Limit

Matter falling onto a compact object (e.g. through accretion; section 1.3) will encounter a radiation pressure from the electromagnetic radiation that is being emitted by the compact object (e.g. X-rays from the accretion disc of an X-ray binary; section 1.3.2). If the source is luminous enough, the radiation pressure can overcome the gravitational potential of the compact object and stop the accretion of matter on to the compact object. This luminosity limit is called the Eddington luminosity and is determined by the mass, M of the compact object:

$$\begin{aligned} L_{\mathrm{Edd}} &= \frac{4\pi G M m_p c}{\sigma_T} \\ &\approx 1.3 \times 10^{38} \left(\frac{M}{M_\odot}\right) \mathrm{erg\ s^{-1}} \end{aligned} \tag{1.4}$$

where $\sigma_T = 6.652 \times 10^{-29}$ m^2 is the Thomson scattering cross-section and $m_p = 1.673 \times 10^{-27}$ kg is the mass of a proton. The effect of L_{Edd} is important in the generation of X-rays by compact objects as very few NSs and BHs are observed to have luminosities higher than this limit. Super-Eddington luminosities are seen in a number of gamma-ray bursts and supernovae, though these are only super-Eddington for a short time, as a significant amount of mass is lost from the system during such events.

1.2 X-ray Binaries

The discovery of X-ray binaries (XRBs) represents the beginning of X-ray astronomy, through the detection of Sco X-1, the first extrasolar X-ray source ever discovered (Giacconi et al., 1962). Since then, the field has rapidly advanced, with 3–5 minute observations with rocket-borne instruments giving way to dedicated X-ray astronomy satellite missions such as *XMM-Newton* (Jansen et al., 2001) and *NuSTAR* (Harrison et al., 2013). XRBs consist of a compact, degenerate stellar remnant in a gravitationally bound system with a stellar companion. The X-ray emission we see is a result of matter being transferred from the stellar companion onto the compact object through the process of accretion.

There are two main classes of XRB, Low-Mass X-ray Binaries (LMXBs) and High-Mass X-ray Binaries (HMXBs), so named after the mass of the companion (donor) star. HMXBs transfer matter on to the compact object through a powerful stellar wind via the process of Bondi-Hoyle accretion, the process of mass transfer on to a compact object travelling through a uniform density medium (Bondi & Hoyle, 1944). All the mass-losing stars in HMXBs are optically bright and are of early spectral type (generally OB stars), massive (M $\gtrsim$ 10M$_\odot$) and generate stellar winds with typical mass-loss rate $\dot{M}_w \sim 10^{-6} M_\odot$ yr^{-1} (Castor et al., 1975). Not all of this mass is accreted by the much smaller compact object (typically a NS) as the stellar wind flows out uniformly in all directions, allowing only a cylindrical region of the outflow to be transferred on to the NS. The fraction of the wind accreted on to the NS $\frac{\dot{M}}{\dot{M}_w}$ is typically $\sim 10^{-3}$–10^{-5}, leading to mass transfer rates of $\dot{M} \sim 10^{-9} M_\odot$ yr^{-1}, consistent with the observed luminosity ($L \sim 10^{37}$ erg s^{-1}) of such sources (Davidson & Ostriker, 1973).

LMXBs are comprised of a compact object in orbit with a stellar companion of low mass (M $\lesssim$ 1M$_\odot$). The companion stars of LMXBs are not massive enough to generate powerful stellar winds like in HMXBs, the mass-loss rate of a typical low-mass star (e.g. the Sun) is $\dot{M}_w \sim 10^{-14} M_\odot$ yr^{-1} and therefore not powerful enough to drive the typical X-ray luminosities seen in LMXBs (which are similar to those seen in HMXBs). The X-ray luminosity of LMXBs is instead driven by the process of Roche lobe overflow (RLO), in which the companion fills its Roche lobe. The Roche lobe of each binary component is defined by the equipotential surface that envelopes both stars and intersects at L_1, the inner Lagrangian point at which the net force is zero. Material from the secondary star that expands beyond the Roche lobe then falls on to the compact object and forms an accretion disc, which generates X-ray emission. Fig. 1.5 highlights the different mechanisms of mass transfer of LMXB and HMXB systems.

It has been shown that the two distinct classes of XRB exist *because of* the two different accretion mechanisms that power them. Sources which accrete via RLO are only long-lived (lifetimes $\gtrsim 10^3$ yr) if the companion mass is $< 2.1 M_\odot$ whilst systems accreting via a stellar wind can only exist as X-ray sources if the companion is of a high enough mass ($M > 20 M_\odot$) to drive a powerful enough wind. Systems with companions between these two mass ranges are not expected to have long X-ray producing lifetimes as the RLO accretion rate is so large ($\dot{M} = 10^{-6} - 10^{-3} M_\odot$ yr^{-1}) that the X-ray emission would be extinguished rather quickly (van den Heuvel, 1975). However, there are a small number of Intermediate-Mass X-ray Binaries (IMXBs) whose companions are in the $1 - 10$M$_\odot$ mass range, although such systems are rare (see e.g. SAX J1819.3-2525 Orosz et al., 2001). This thesis will focus on LMXBs and thus more details on the process of accretion are given in Section 1.3.

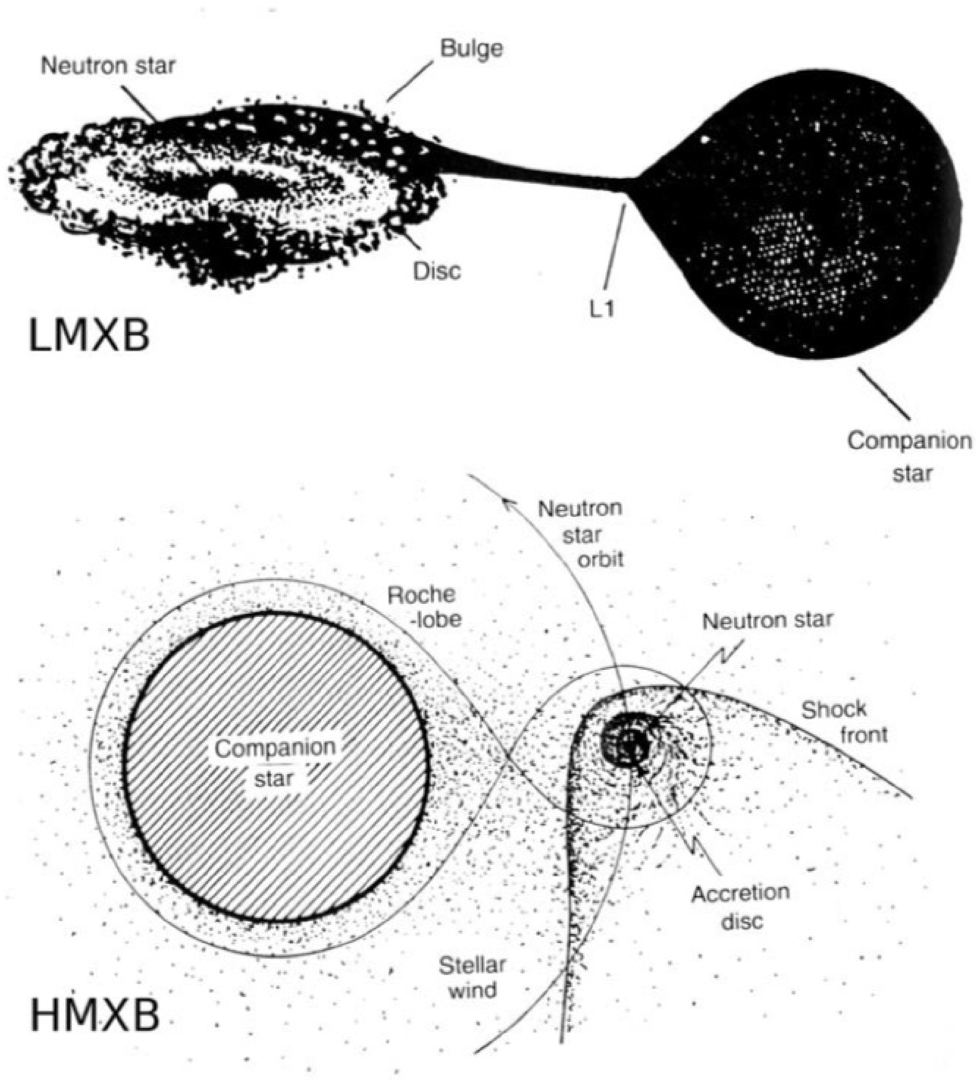

FIGURE 1.5: Artist's impression of the two mechanisms of mass transfer from the companion star on to the compact object by LMXBs (top) and HMXBs (bottom). In the LMXB case, a low-mass star is filling its Roche lobe and mass flows through the inner Lagrangian (L_1) point on to the primary. In HMXBs, the compact object is orbiting a massive star with a very powerful stellar wind. The material ejected by the massive star is accreted by the compact object as it orbits, producing X-rays. Image credit: EXOSAT/ESA.

1.3 Low Mass X-ray Binaries

LMXBs are some of the most luminous observed in the X-ray sky. In fact, Sco X-1 – the prototypical LMXB – remains the brightest persistent extrasolar X-ray source ever discovered. The compact object in luminous LMXBs ($> 10^{35}$erg s^{-1}) is either a BH or a NS; compact binary systems below this luminosity limit usually harbour a white dwarf (WD) and are known separately as Cataclysmic Variable (CV) or Accreting White Dwarf (AWD) systems. This thesis focusses primarily on BH systems and as such, AWDs will not be discussed in any great depth but to contrast against the properties of other

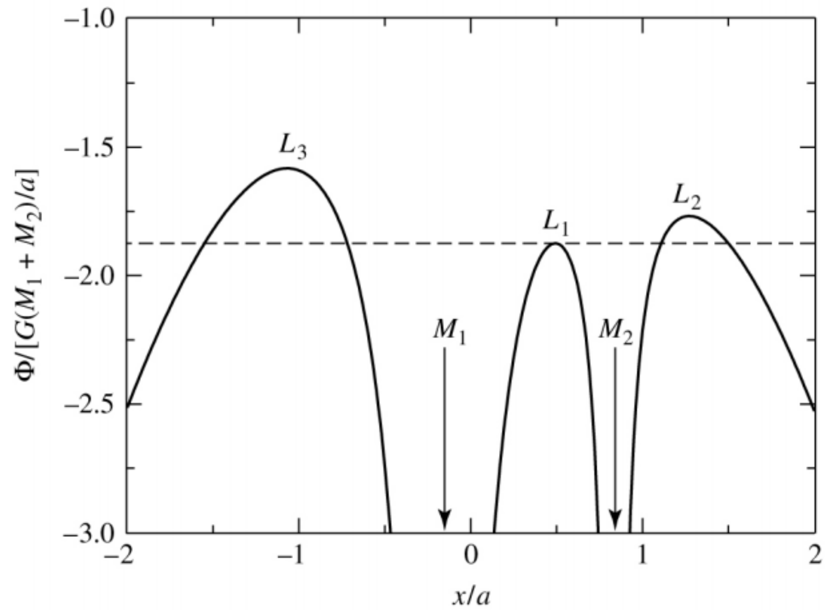

FIGURE 1.6: The effective gravitational potential, Φ, plotted along the line connecting the primary and secondary of a binary system with masses $M_1 = 0.85 M_\odot$ and $M_2 = 0.17 M_\odot$ separated by a distance $a = 0.718 R_\odot$. Three of the Lagrangian points (L_1 to L_3), where the net force is equal to zero, are also marked. If star M_2 fills its Roche lobe, and hence the total energy per unit mass of a particle exceeds the value of Φ marked by the dashed line, then matter will pass through L_1 and into the potential well of M_1 (since $L_1 < L_3$). Image credit Max Pettini, Structure and Evolution of Stars lectures, University of Cambridge.

LMXBs. However, it is acknowledged that much of our current knowledge of accretion disc properties stems from studies of AWDs (Warner, 1995).

As discussed in section 1.2, the companion stars of LMXBs do not have powerful enough stellar winds for Bondi-Hoyle accretion to be responsible for the observed X-ray luminosity and are instead driven by RLO, which is subject to the compbined gravitational potential of the pair of stars. Close to the centre of each star, the potentials are almost spherical. However, approaching the centre of mass of the binary, the potentials are distorted into a 'pear' shape, with the critical equipotential being that which includes the L_1 point. The one-dimensional shape of the equipotential surface is plotted in Fig. 1.6 illustrating that as the secondary star expands, matter will be transferred through L_1 into the potential well of the compact object. An accretion stream forms as the stellar material flows through this saddle point on to the compact object at a rate of $\dot{M} \sim 10^{-8} M_\odot\ \mathrm{yr}^{-1}$ (van den Heuvel, 1975).

To be able to initiate RLO, LMXBs must be more compact than HMXBs, and as a result tend to have much shorter periods (tens of minutes to several hours). However in order to form the compact object (a BH or NS), the progenitor must have been a massive supergiant with a radius much larger than the present separation of the compact object and its companion. Such systems must therefore lose a large amount of angular momentum during their evolution into the LMXB phase. This shrinking of the orbit is attributed to a 'Common Envelope' (CE) phase in which the low-mass companion orbits within the envelope of the supergiant primary and, due to frictional forces cause it to rapidly spiral in while, at the same time, ejecting the envelope of the supergiant. This leaves the low-mass companion orbiting the stripped helium core of the progenitor which then undergoes a core-collapse supernova explosion, forming the NS or BH primary. The LMXB phase is then initiated when the orbit shrinks enough to allow mass transfer through RLO either through the process of magnetic braking, or the energy loss through gravitational wave radiation. Magnetic braking is the process by which material coupled to magnetic field lines of the star (such as a stellar wind) will co-rotate with the star as if it were a solid body until the material exerts enough pressure on the magnetic field lines to escape, carrying angular momentum away from the system. This has the effect of slowing the spin of the star down since the binary components are tidally locked (the star's rotation period is equal to the orbital period), the orbit will therefore shrink to conserve angular momentum. Gravitational radiation, on the other hand, is a result of the two binary components causing periodic distortions of spacetime as they orbit. These distortions manifest as gravitational waves which carry angular momentum away from the system, shrinking the orbit (Faulkner, 1971). Fig 1.7 illustrates an example of the evolution of an LMXB that results in a binary millisecond pulsar (Tauris & van den Heuvel, 2006).

The optical light emitted by LMXBs is normally dominated by the accretion disc (see section 1.3.2 for more details), which forms around the compact object in order to conserve angular momentum of the material flowing through the L_1 point. Since total angular momentum in the whole disc must be conserved, the angular momentum must be transported from the innermost regions of the accretion disc to the outermost regions. The α-disc model (Shakura & Sunyaev, 1973) introduced the concept of the α parameter which describes the efficiency of angular momentum transport connected with viscous processes in the disc. The Shakura & Sunyaev (1973) disc model, now widely accepted and the best studied theoretical model of accretion discs, argued that the magnetic fields are responsible for the transport of angular momentum outwards through the disc. This was given a boost by the discovery that a weakly magnetised accretion disc is subject to a powerful instability (the magnetorotational instability; MRI) which provides the necessary mechanism for angular momentum redistribution (Balbus & Hawley, 1991; Balbus & Hawley, 1998). An artist's impression of a typical LMXB is shown in Fig. 1.8.

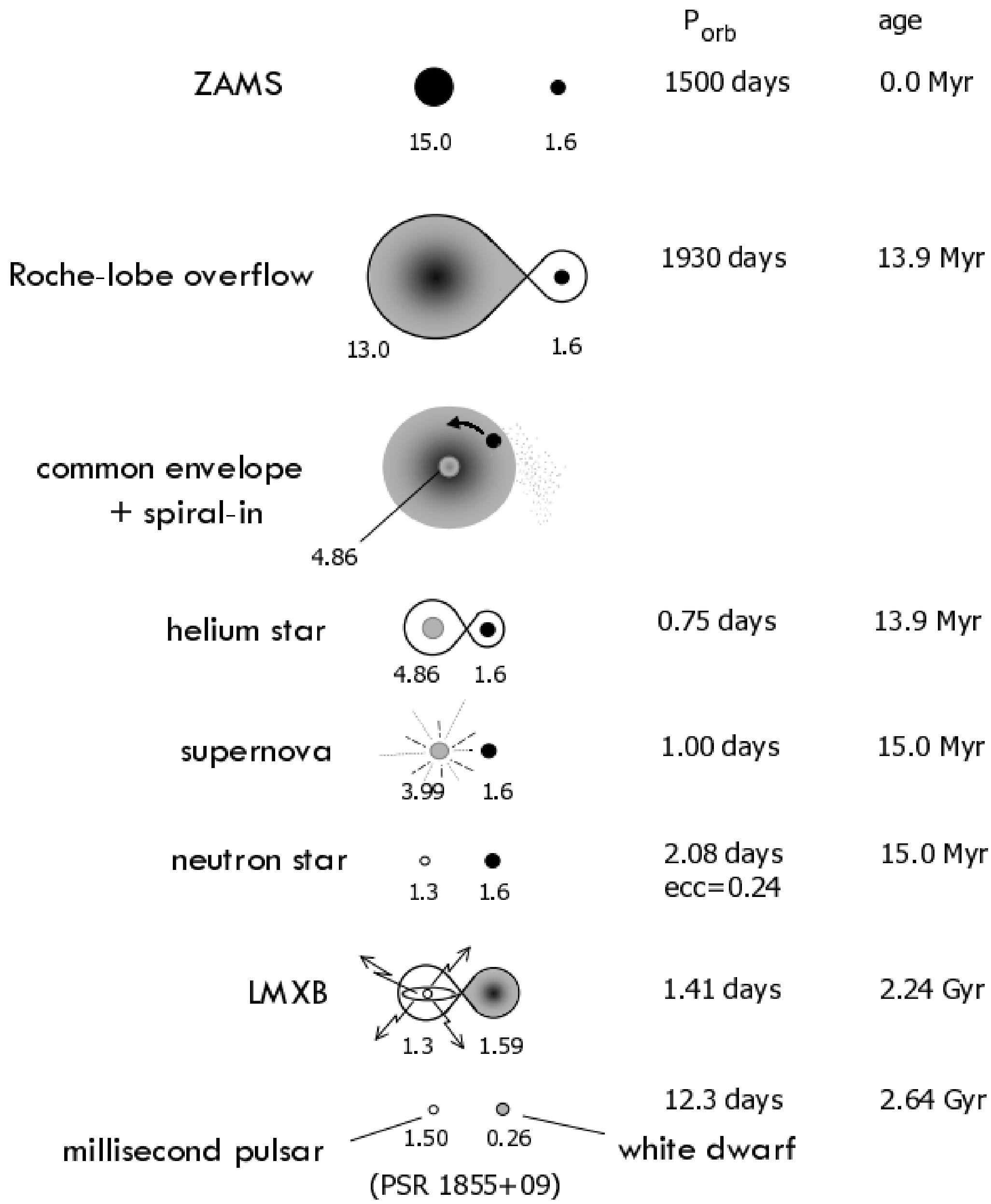

FIGURE 1.7: A cartoon depicting the evolution of a zero age main sequence (ZAMS) binary system eventually leading to the LMXB phase and finally the formation of a binary millisecond pulsar (Tauris & van den Heuvel, 2006).

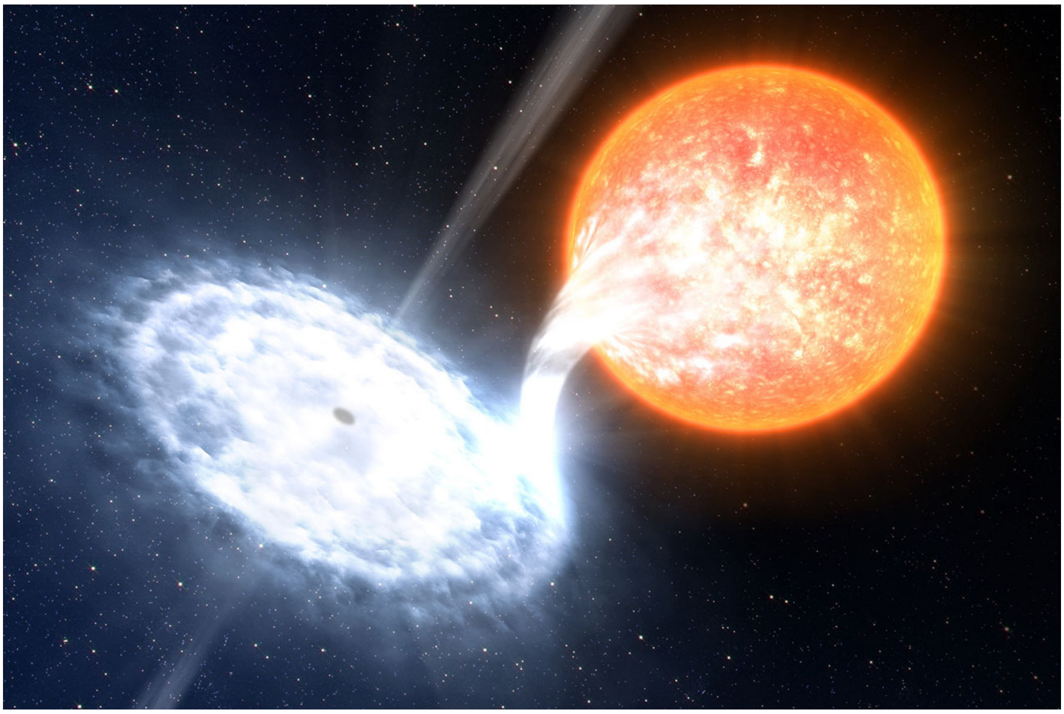

FIGURE 1.8: An artist's impression of a Low Mass X-ray Binary showing the blue accretion disc which forms as a result of the transfer of matter from the low mass, red companion star. Also shown are jets extending from the poles of the central compact object. Image Credit: ESO/L. Calcada.

1.3.1 X-ray transients

In the 1960s, X-ray astronomy was mostly conducted using X-ray detectors on sounding rockets, which only offered limited observation time (~ 5 mins) per flight. However, by the late 1960s there were enough flights to provide regular sampling of the Galactic plane to identify, in May 1967, a source that had not been seen when the region was previously scanned in 1965 and which had disappeared when the position was scanned again in September 1967. This source, designated Cen X-2, is known to be the first transient X-ray source ever discovered (Harries et al., 1967). More discoveries soon followed, with Cen X-4 discovered in 1969 as the second transient X-ray source (Conner et al., 1969). By the mid-1970s enough sources with similar characteristics had been discovered that X-ray transients (XRTs) formed a new class of X-ray source.

The key to understanding XRTs came with the realisation that almost all extrasolar XRTs are XRBs (see e.g. Elvis et al., 1975). Identification of the optical counterparts allowed astronomers to divide XRTs into two distinct classes, HMXB and LMXB transients. HMXB transients almost all contain a NS in a wide (orbital period $P_{\rm orb} \sim 10$'s of days), eccentric orbit around a high mass early-type star. Some of these stars (B emission line stars; Be) possess a dense, equatorial outflow due to spinning very close to their break-up velocity (Corbet, 1984). Mass transfer only occurs when the NS passes

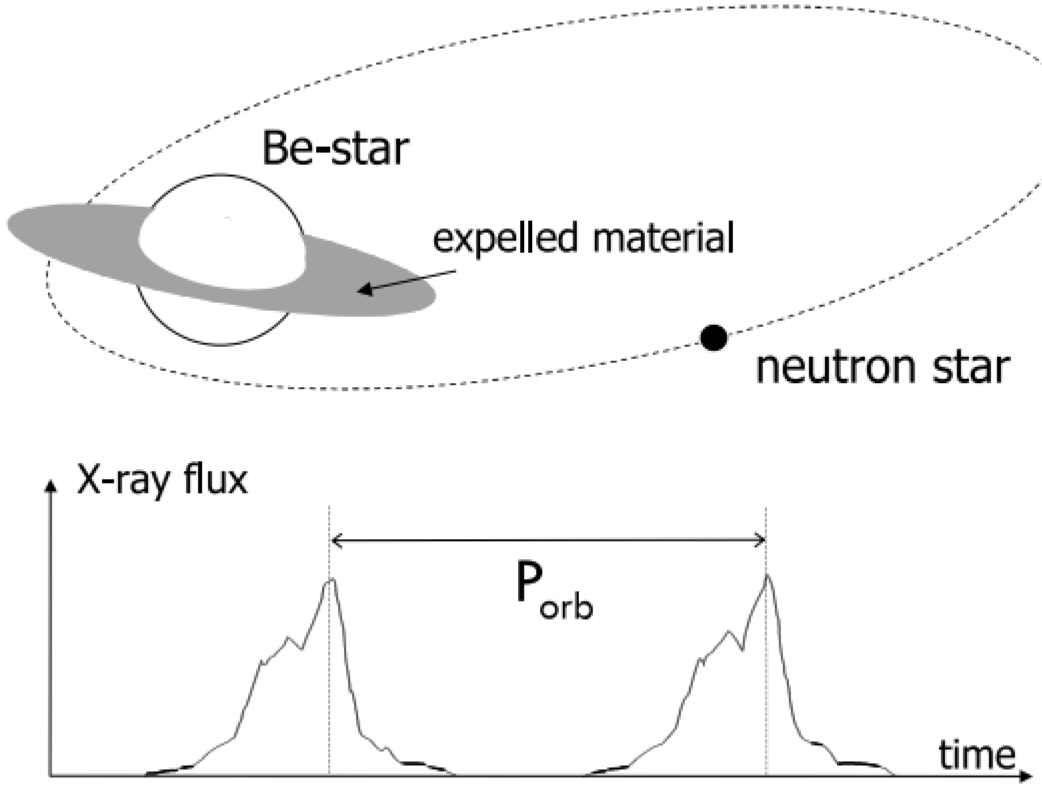

FIGURE 1.9: Schematic of a Be XRT in which a NS is in an eccentric orbit with a Be star which posseses a dense equatorial outflow. At periastron the NS accretes circumstellar matter, resulting in an X-ray outburst that repeats on the $P_{\rm orb}$ of the system, shown in the accompanying light curve. Adapted from Tauris & van den Heuvel (2006).

through periastron and accretes from the 'disc-wind' of the Be star. Be XRT outbursts therefore occur regularly, on the $P_{\rm orb}$ of the system (see Fig. 1.9). HMXB XRTs containing O/B supergiant companions can often be detected as transient X-ray pulsars, in which the strong magnetic field of the NS directs in-falling matter towards the poles as it passes close to periastron. We see X-ray pulsations if the magnetic and rotational axes of the NS are misaligned as the magnetic poles sweep through Earth's line of sight (see e.g. Cen X-3; Schreier et al., 1972).

LMXB transients accrete via RLO, as with the persistent sources. LMXB transients (often called soft X-ray transients; SXTs) are indistinguishable from LMXBs described in Section 1.3. However, they exist for years (often decades) at a time in a low, *quiescent* state yielding very low X-ray and optical fluxes. At some point in the lifetime of a SXT, mass transfer on to the compact object will increase dramatically and a powerful X-ray outburst occurs and the accretion disc brightens by factors of up to $\sim$ 1000 in X-ray intensity and $\sim$ 7 magnitudes in optical wavebands (see e.g. the case of A0620-00; Kuulkers 1998).

The erratic mass transfer on to the compact object is a subject of much debate but the most successful model to explain the behaviour of LMXB outbursts has been the thermal-viscous disc instability model (DIM; see e.g. Cannizzo, 1993; Lasota, 2001), which is represented in Fig. 1.10 by the 'S-curve'. The S-curve represents the locus at which the accretion disc is in thermal equilibrium. Any deviation from this curve will be corrected quickly on the thermal timescale as the disc tries to attain equilibrium again. A Shakura-Sunyaev disc at low mass-accretion rates contains mostly neutral hydrogen but is unstable both thermally and viscously such that a small increase in temperature (associated with increasing disc mass from steady mass transfer by RLO) produces a huge increase in opacity. This increased opacity means that the higher energy photons in the disc begin to ionise the hydrogen, meaning that their energy remains in the disc, increasing its temperature, rather than escaping to cool it. This, in turn, provides more high energy photons to ionise more hydrogen, meaning more photons are trapped in the disc and a thermal runaway occurs until hydrogen is almost fully ionised (the first 'bend' in the S-curve). The thermal instability then triggers a viscous instability, as the increased disc temperature causes an increased rate of mass accretion on to the compact object which exceeds the rate at which it is replenished by RLO from the companion star. The disc therefore starts to cool until hydrogen recombines (the second 'bend') and the disc returns to a quiescent state until mass builds up enough to trigger the instability again. The DIM has been shown to describe the outburst-quiescence cycle of many LMXB transients (a sample of 29 transients were tested by Coriat et al., 2012). An in depth investigation of the DIM is presented in Chapter 6.

The regularity at which new transients are discovered is almost entirely due to the advent of a number of X-ray satellites which possess dedicated wide-field instruments capable of scanning a large fraction of the sky several times a day. Instruments such as the *Monitor of All-sky X-ray Image* aboard the International Space Station (ISS/*MAXI*; Matsuoka et al. 2009) and the BAT aboard *Swift* (Barthelmy et al., 2005) have enabled daily monitoring of previously known transients as well as discovering several new sources a year.

1.3.2 The Spectrum of LMXBs

The range of wavelengths that the accretion disc spectrum of LMXBs emits over can be described by studying the accretion luminosity over the varying radius of the disc. A NS of mass $M_{\rm NS}$ accreting matter at a rate $\dot{M}$ will have an accretion luminosity:

$$L_{\rm acc} = GM_{\rm NS}\dot{M}/R_{\rm NS} \tag{1.5}$$

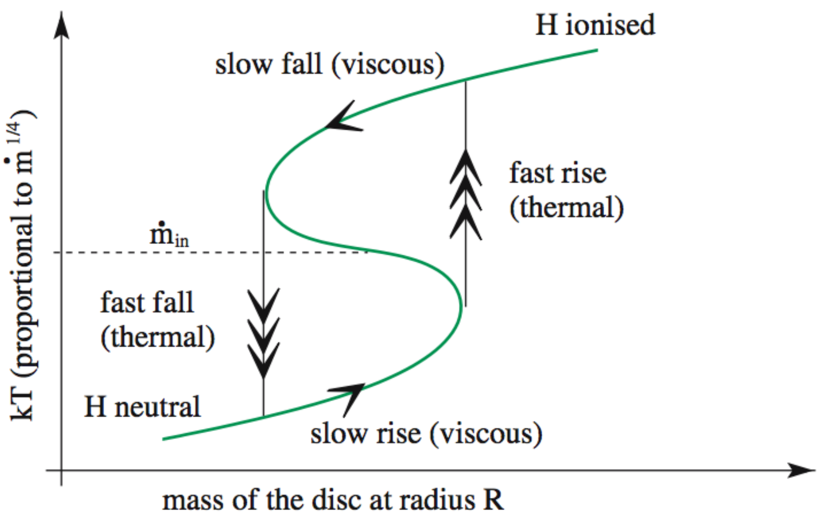

FIGURE 1.10: The hydrogen ionisation instability showing how an accretion disc jumps discontinuously between a cool, neutral state and a hot, ionised state. In quiescence a cold, neutral disc fills up with matter, until at some radius a critical temperature is reached, triggering an outburst as a heating wave propagates through the disc. The resultant increased mass accretion rate is maintained until the outer disc temperature dips below the hydrogen ionisation temperature, at which point a cooling wave propagates through the disc and the source becomes quiescent. Adapted from Done et al. (2007).

through the release of gravitational potential energy at the NS surface, $R_{\rm NS}$. If it is assumed that all this energy is released as blackbody radiation then the temperature is calculated to be $T_{\rm bb} = (L_{\rm acc}/4\pi R_{\rm NS}^2\sigma)^{1/4}$. For a typical $(1.4M_\odot)$ NS accreting at $\sim 10^{36}$ erg s^{-1}, $T_{\rm bb} \sim 10^7$K, or $k_{\rm B}T_{\rm bb} \sim 1$ keV (where $k_{\rm B} = 1.381 \times 10^{-23}$ m^2 kg s^{-2} K^{-1} is the Boltzmann constant), i.e. X-ray emission. However, this only applies to emission at the surface of the NS and so the true spectrum of the accretion disc is calculated by adding up the contributions from several disc annuli, each of which is assumed to radiate as a blackbody as described above, but also emits at optical and UV wavelengths at larger radii as the disc gets cooler further away from the compact object (Mitsuda et al., 1984; La Dous, 1989). The resultant spectrum for a disc around a NS is a continuum which peaks at X-ray energies. It must be noted that the blackbody temperature calculation is slightly more complicated for an accreting BH, as the lack of a hard surface at the Event Horizon means that much of the matter that reaches this region could simply fall into the BH and add to its mass, rather than be radiated. This introduces a new uncertainty to the calculation of $L_{\rm acc}$, parameterised as the dimensionless quality η, the efficiency. The accretion power of a BH therefore becomes:

$$\begin{aligned} L_{\rm acc} &= 2\eta G M_{\rm BH}\dot{M}/R_{\rm S} \\ &= \eta\dot{M}c^2 \end{aligned} \tag{1.6}$$

where R_S is the Schwarzchild radius of the BH.

The optical spectrum of an accreting LMXB is, as discussed above, mostly dominated by the accretion disc as it greatly outshines the dim main sequence companion - the typical absolute magnitude V of an LMXB accretion disc is in the range $-5 \lesssim \mathrm{V} \lesssim 5$ (van Paradijs & McClintock, 1994), compared to $\mathrm{V} \gtrsim 8$ for typical M dwarf stars (Lépine & Gaidos, 2011). The observed V appears to be correlated with the X-ray luminosity of the source, suggesting that the optical brightness is dependent on the strength of the central X-ray source. A simple model for the optical emission of LMXBs is presented by van Paradijs & McClintock (1994) in which X-rays from the central source irradiate the outer accretion disc and are reprocessed into optical and UV photons by the outer regions of the disc. The observed optical luminosity is proportional to the X-ray luminosity and the P_{orb} of the system.

A large fraction of the reprocessed X-ray emission appears at the UV and blue end of the spectrum (van Paradijs & McClintock, 1994), thus the optical spectrum of a typical LMXB consists of a blue ($B-V \sim -0.1$) continuum with a few high excitation emission lines. Notable emission lines include He II λ4686, the Bowen blend at $\lambda\lambda$4640−50 and the Balmer series ($\mathrm{H}_{\alpha,\beta,\gamma}$ etc). In the case of SXTs the optical spectrum changes drastically when the source enters a period of quiescence. In quiescence, the contribution from the accretion disc is reduced and signatures of the low-mass companion can become apparent in the spectrum as the system reaches its pre-outburst magnitude (Casares et al., 1993, detected the companion of V404 Cyg at $R \sim 16.5$, whilst its outburst magnitude was $R \sim 12$). Comparing optical spectra of quiescent SXTs to those of spectral-type standard stars enables the spectral classification of the companion star to be measured (Fig. 1.11), leading to mass determinations of the compact object which are discussed in more detail below.

The X-ray spectrum of a typical LMXB has multiple components. The accretion disc exhibits blackbody emission as discussed above. However, at harder X-ray energies there exists a power-law component to the spectrum which is likely due to inverse Compton scaterring of soft photons by a population of hot electrons which surrounds the accretion disc itself. This population of electrons is known as the accretion disc corona (ADC) and the geometry of such a region is widely disputed. In some LMXBs the X-ray spectrum exhibits more complicated components (see e.g. GX 339-4 Tomsick et al., 2008; Fürst et al., 2015). X-ray reflection is the process in which hard X-ray photons (> 10 keV) originating in the ADC are Compton scattered by free electrons in the disc, which gives the hard X-ray component of the spectrum a characteristic broad hump-like shape, as harder X-ray photons are preferentially Compton scattered (Lightman & White, 1988). Line emission is also seen in LMXB spectra, most notably in the form of the Fe K_α

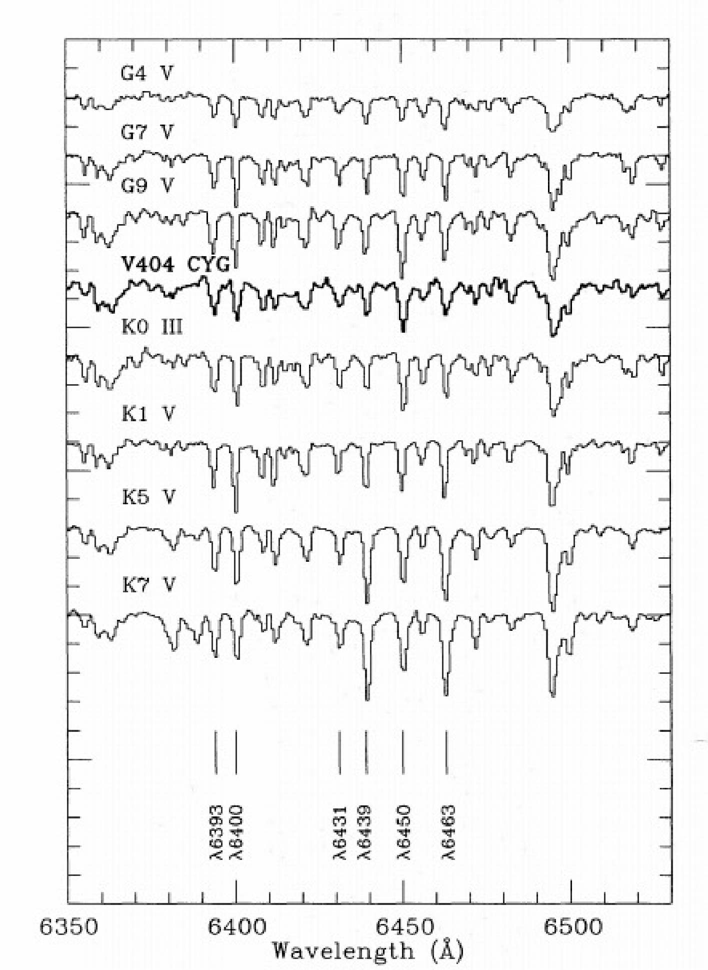

FIGURE 1.11: Optical spectra of the SXT V404 Cyg in quiescence (bold) and several low-mass comparison stars in the $\lambda\lambda 6350 - 6530$ range. The strongest absorption features associated with the companion star that appear in the spectrum of V404 Cyg are labelled. Adapted from Casares et al. (1993).

fluorescence line at ~ 6.4 keV. Fe K_α emission is produced, once again, when the ADC illuminates the disc (see Fig. 1.12). The iron in the disc absorbs the hard X-rays and is excited from the ground state, which, when returning to the ground state, releases the X-ray energy as photons. Due to the high energies of such photons, the Fe fluorescence lines can be used to probe the regions closest to the compact object. The X-ray spectrum can change drastically, however, dependent on the X-ray spectral state of the source, an overview of which is given in section 1.3.3.

1.3.3 X-ray spectral states and the Hardness Intensity Diagram

As discussed in section 1.3.1, a number of LMXBs exhibit transient behaviour in which they undergo X-ray/optical outbursts on time scales of weeks to months, followed by long periods of quiescence where there is no X-ray activity. XRTs that contain a BH (Black

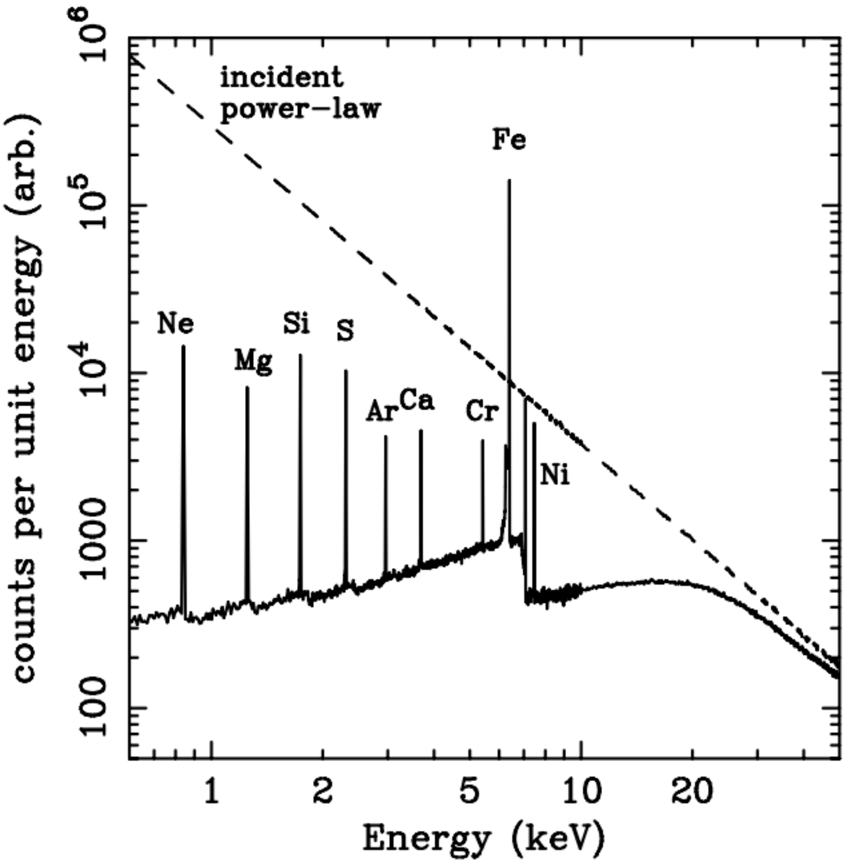

FIGURE 1.12: A Monte-Carlo simulation of X-ray reflection from an illuminated slab of gas (i.e. the accretion disc) based on the models of Reynolds et al. (1994). The dashed line shows the illuminating power law (the ADC) with a spectral index $\Gamma = 2$. The solid line shows the resultant reflection spectrum, including the fluorescence features and the Compton hump. Adapted from Fabian & Ross (2010).

Hole X-ray Transients; BHXRTs) all exhibit varying outburst durations and recurrence rates but all appear to follow characteristic flux evolution during the course of their outbursts. This evolution is tracked by the Hardness - Intensity diagram (HID; Fender et al. 2004), which plots X-ray intensity against the Hardness Ratio (HR), usually the ratio of the hard X-ray band to the soft X-ray band flux. A schematic representation of the HID is shown in Fig. 1.13 and shows the various X-ray states a BHXRT exhibits throughout the course of an outburst.

At low accretion rates BHXRTs will occupy the 'Hard State,' with X-ray spectra characterised by a power law of the form $f_E \propto E^{-\Gamma}$, with a spectral index $\Gamma \sim 1.5$, consistent with the inverse Compton scattering of soft photons by the hot ADC. The X-ray spectrum typically exhibits little to no contribution from the accretion disc which is generally interpreted as evidence of the disc being heavily truncated at large radii thus providing fewer soft X-ray photons (Esin et al., 1997). The HR in the hard state is typically $\gg 1$ and the source occupies the lower right-hand corner of the HID. Also associated with the hard state are the formation of steady compact, relativistic jets. Such jets emit via the synchrotron self-absorption process, i.e. photons are produced by the radial acceleration of electrons in a magnetic field and then absorbed by the same electron population. This is manifested in the spectral energy distribution as a flat or inverted ($\Gamma \geq 0$) component in the radio/mm (and sometimes infrared) bands (Fender et al., 2004).

As the thermal-viscous disc instability begins to take effect, the source luminosity increases and the spectrum becomes softer as the (now brighter) accretion disc becomes the dominant component of the X-ray spectrum. This transition to a 'Soft State' is coupled with the Lorentz factor of the jet increasing rapidly and producing internal shocks in the outflow, seen as a radio flare as faster moving material at the base of the jet collides with the slower material further away from the BH (Vadawale et al., 2003; Fender et al., 2004). Such flares exhibit a spectrum with a negative index, indicative of optically thin synchrotron emission (Fender et al., 1999), in contrast to the optically thick emission seen in the steady compact jets of the hard state.

As the source transitions to the soft (or thermal dominated) state, the production of jets ceases and the inner edge of the accretion disc moves in towards the innermost stable circular orbit (ISCO) of the BH and the spectral contribution from the ADC is quenched. As material in the disc is depleted, the source moves from the soft state back to the hard state, restarting the production of jets as the source fades into a hard, quiescent state once more (Fender et al., 2004).

As well as the cessation of jet formation, the soft state is also associated with the driving of another type of outflow in the form of accretion disc winds. Disc winds manifest themselves in X-ray spectra as high velocity, highly ionised absorption features and are ubiquitous in the jet-free soft states of all BHXRTs (Ponti et al., 2012). A visualisation of the different accretion states is presented in Fig. 1.14, which shows the range of X-ray spectra seen in just one source during the different stages of an outburst, along with the proposed accretion geometry for each of those states.

The origin of jet emission remains a hot topic in astronomy, but models often offer a magneto-hydrodynamic (MHD) solution to the problem. Blandford & Payne (1982) introduced the idea that radio jets may be produced by magnetic field lines removing angular momentum from the accretion disc in a collimated flow. Later, Meier et al. (2001) showed that the strongest jets result when the accretion flow has a large scale height (i.e. the ADC), and so they are naturally suppressed in the soft state which is dominated by the geometrically thin Shakura-Sunyaev disc. There are a number of models for jet formation, most of which feature a magnetised accretion disc as the basis of a MHD outflow which highlights the importance of magnetic fields in XRBs (see e.g. Kudoh et al., 2002; Lynden-Bell, 2003; Livio et al., 2003).

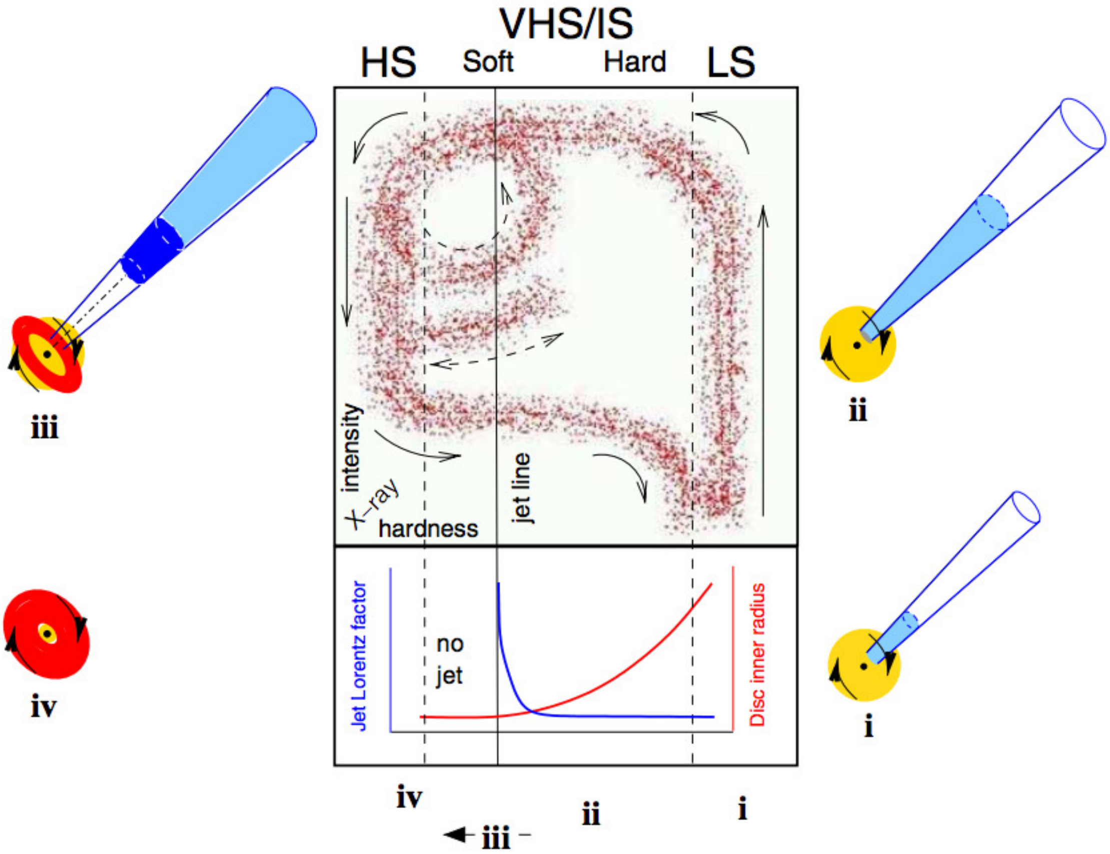

FIGURE 1.13: A schematic of the Hardness - Intensity diagram showing the typical evolution of the flux of a BHXRT throughout the course of an outburst. Also shown around the outside are the relative contributions of the compact jet (blue), ADC (yellow) and accretion disc (red) at various stages of the outburst. Adapted from Fender et al. (2004).

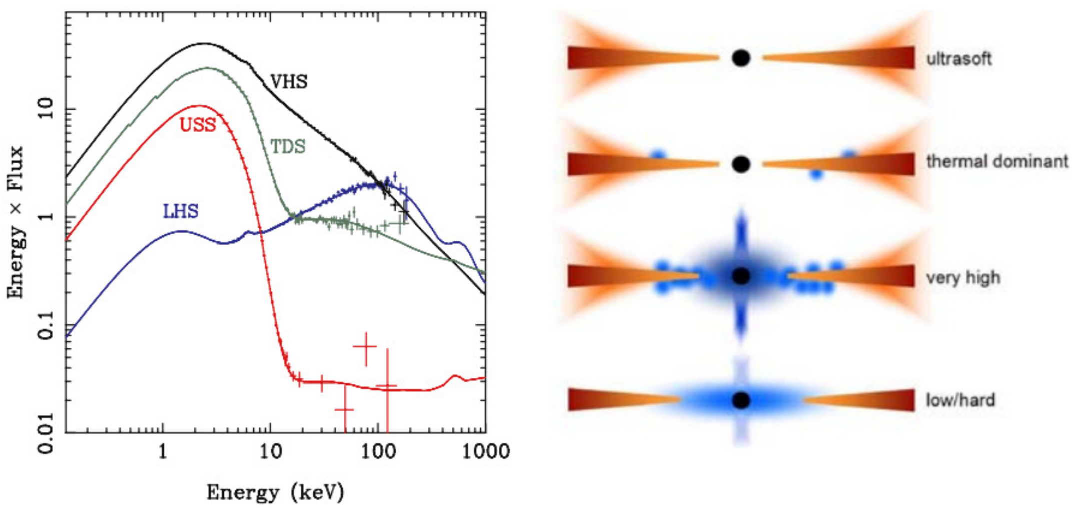

FIGURE 1.14: *Left:* X-ray spectroscopy of a selection of spectral states of GRO J1655-40 during its 2005 outburst. *Right:* A schematic of the proposed accretion flow changes to explain these different spectra showing differing contributions from the disc, a hot inner flow (ADC), an associated jet and a wind. Adapted from Done et al. (2007).

1.3.3.1 Variability and timing analysis

As well as the spectral changes discussed in section 1.3.3, LMXBs also exhibit temporal behaviour where the variability correlates with spectral state (see e.g. reviews by van der Klis, 2006; McClintock & Remillard, 2006). Here I will present a brief overview of timing properties of LMXBs and introduce key concepts in timing analysis which will be utilised in future chapters.

To analyse the fastest timing characteristics of LMXBs we study the Fourier power spectrum of the light curves of such objects, which is a decomposition of the light curve into a spectrum of frequencies over a continuous range. This provides an estimate of the variance as a function of Fourier frequency ν in terms of the *power density* $P_\nu(\nu)$ (van der Klis, 1989). A number of components make up the power spectrum which describe the variability of a source, examples of which are shown in Fig. 1.15. Features in the power density spectrum (PDS) are usually categorised as *noise* and *quasi-periodic oscillations* (QPOs) and are measured by least-squares fitting techniques. A QPO is a finite-width peak in the power spectrum and can usually be described with a Lorentzian $P_\nu \propto \lambda/[(\nu - \nu_0)^2 + (\lambda/2)^2]$ with centroid frequency ν_0 and full width at half maximum (FWHM) λ. This represents the power spectrum of an exponentially damped sinusoid and the properties of such features are correlated strongly with spectral state. Noise manifests itself in the PDS as a power law component ($P_\nu \propto \nu^{-\alpha}$) with an index α in the range $0 - 2$.

As an LMXB progresses through the HID (Fig. 1.13), the centroid frequency of the QPO changes, increasing as the spectrum softens, reaching a maximum amplitude as the source reaches the hard intermediate state before diminishing as spectral evolution continues (see Fig. 1.15). The strength of the variability of a source is usually reported in terms of its fractional root-mean-squared (rms) amplitude $r \propto P^{1/2}$ where $P = \int P_\nu \mathrm{d}\nu$ is the integrated power. LMXBs exhibit the highest levels of variability ($\sim 20 - 50\%$ rms) in the hard state, indicating that source variability and therefore QPOs are associated with the hot inner flow (the ADC), which dominates in the hard state. The emerging model is one of the inner flow precessing as a solid body, causing the modulation observed in the X-ray and optical light curves of some LMXBs (Ingram et al., 2009) and there is some evidence that QPO frequencies are related to compact object mass in BH systems (Remillard et al., 2002).

Variability can also be seen on longer timescales, which is usually analysed via a different form of the power spectrum called the Lomb-Scargle periodogram. Regular Fourier analysis requires that the data points be evenly spaced, which is why such techniques are ideal for fast timing studies. However, when studying variability over days, one

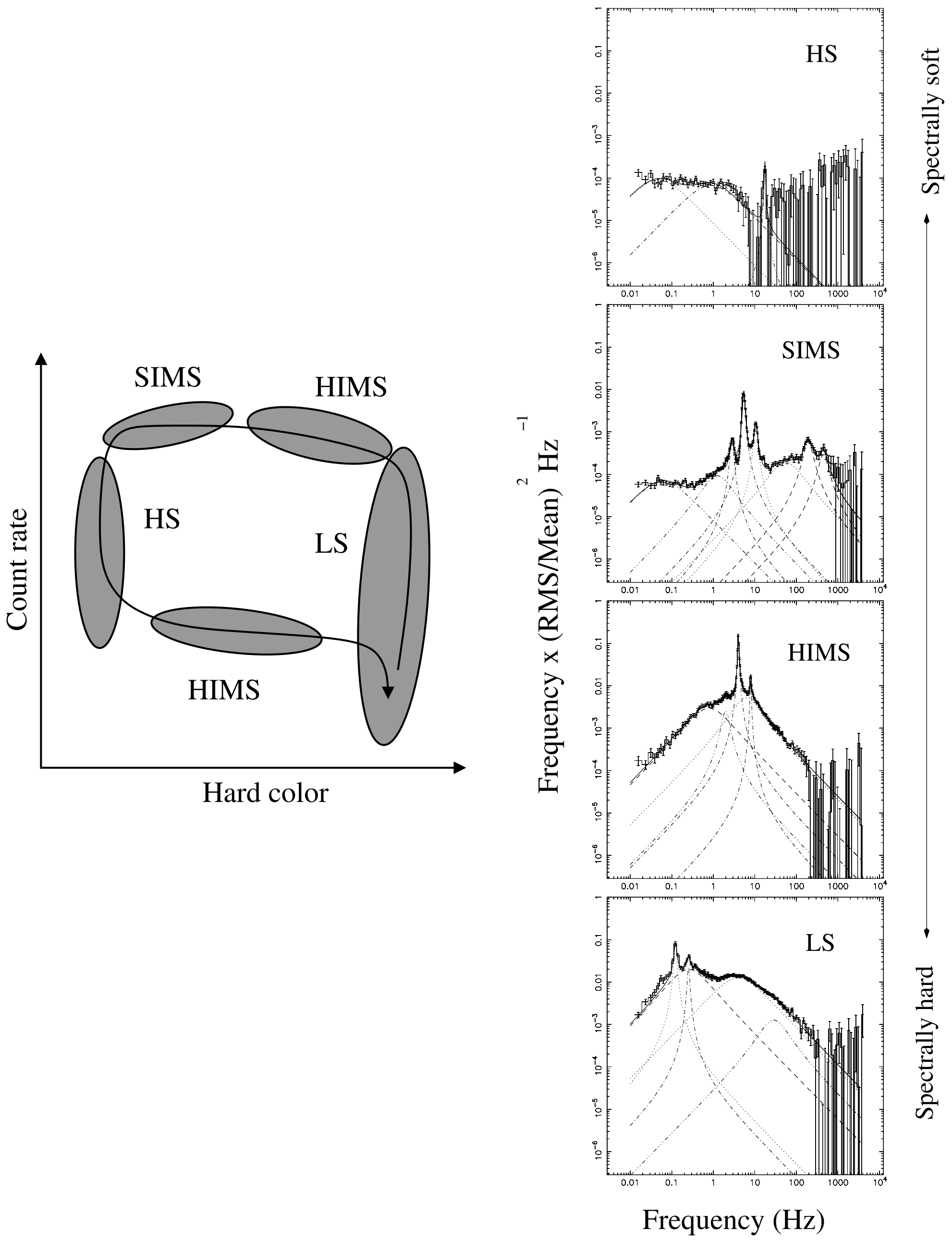

FIGURE 1.15: The evolution of the Fourier power spectrum of a BHXRT as it progresses through the HID during an outburst. The power spectra exhibit different variability components depending on the accretion state of the source. The main states are the high (soft) state (HS), soft intermediate state (SIMS), hard intermediate state (HIMS) and the low (hard) state (LS). Figure kindly provided by Diego Altamirano.

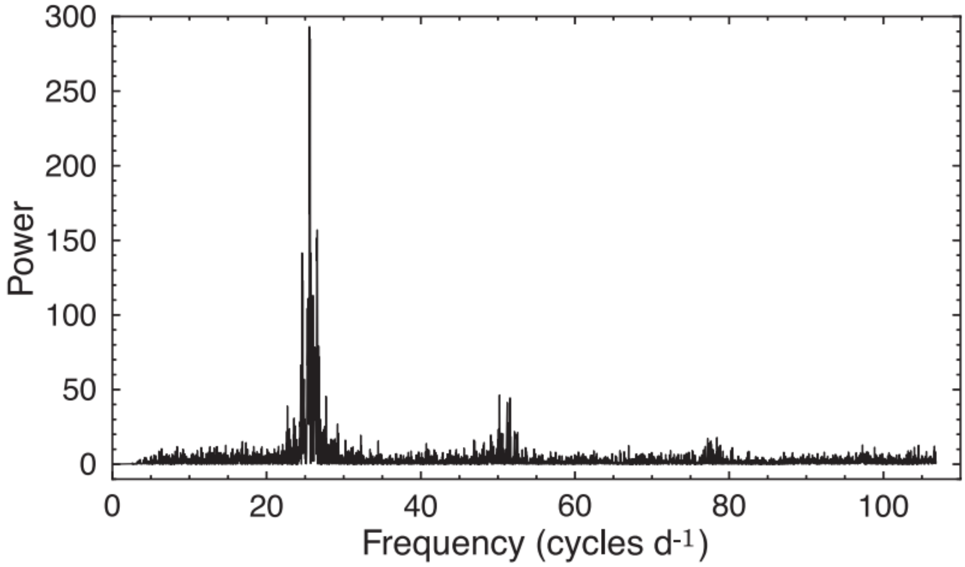

FIGURE 1.16: The Lomb-Scargle periodogram of the AWD SBSS 1108+574, showing aliasing. The true periodicity (fundamental frequency) in this case is at 25.56 cycles d^{-1}, but aliases are seen at double and triple this value, representing $\frac{1}{2}P$ and $\frac{1}{3}P$, respectively. Also visible are the ±1 cycle d^{-1} aliases. Adapted from Carter et al. (2013).

will typically observe a source in irregular blocks, due to, for example, only being able to observe with ground-based optical telescopes at night, or the P_{orb} of space-based observatories. Lomb-Scargle periodogram analysis (Lomb, 1976; Scargle, 1982) assumes that a discrete data set (i.e. a light curve) can be approximated by a weighted sum of sinusoids of frequencies determined by picking the frequency that minimises the residuals after least-squares fitting. A source's periodicity can be determined by analysing the resultant power spectrum, which will have a strong peak at the frequency at which a periodicity is supposedly present in the light curve.

Lomb-Scargle analysis requires long data sets to minimise the effects of aliasing, i.e. strong power in the periodogram due to sinusoids of different frequencies fitting the same data set (see Fig. 1.16), which can lead to mis-identification of the true periodicity. Nevertheless, periodograms can be used to find P_{orb} of sources from their light curves, as well as variability due to effects such as a precessing accretion disc.

If the light curve does not obviously exhibit any sinusoidal variations, then the Phase Dispersion Minimisation (PDM) technique can be used (Stellingwerf, 1978). PDM searches for periodic components in a time series by 'folding' the data on a series of trial periodicities to produce a light curve as a function of orbital phase. The folded data is then divided into a series of bins and the variance of the amplitude in each bin is calculated. The combined bin variances are compared to the overall variance of the data set. A true periodicity will have a small bin to total variance ratio and a PDM periodogram is usually shown as a plot of this ratio against the trial period. PDM analysis is particularly useful in analysing the light curves of dipping and eclipsing sources, as such structure is highly non-sinusoidal.

1.3.4 Determining compact object masses

To measure the mass of the compact object in an LMXB system, one needs to observe the orbital motion of the companion star, which is best done via optical spectroscopy of the mass donor. This is remarkably difficult in persistent LMXBs (although not impossible, as discussed below) as the majority of the optical light seen is emitted by the accretion disc from which is difficult to measure the velocity semi-amplitude of the compact object (K_1). This is due to its typically asymmetric brightness distribution and, generally, the large discrepancy between the mass of the donor and the compact object in LMXBs, meaning that $K_1 \ll K_2$, the velocity semi-amplitude of the donor. However, as discussed in section 1.3.2, when an XRT fades to quiescence, the contribution from the accretion disc significantly decreases and signatures of the companion can become visible in the spectrum. Comparing quiescent spectra of the system with those of 'spectral type standard' stars enables identification of the spectral type of the companion. As the companion star orbits the compact object, the narrow absorption features of the mass donor are Doppler shifted from their rest wavelength (radial velocity shifts) which results in a velocity modulation over $P_{\rm orb}$. The radial velocity curve is constructed by cross-correlating the time-resolved spectra of the source with the rest wavelength spectrum of a star of identical spectral type to the companion. Fitting a sinusoid of the form:

$$V(t) = \gamma + K_2 \sin\left(\frac{2\pi}{P_{\rm orb}}[t - T_0]\right) \tag{1.7}$$

provides information about the radial velocity of the system relative to the Sun (systemic velocity; γ), absolute phase zero (sometimes representative of the inferior conjunction of the secondary star; T_0) and K_2.[1] K_2 is actually equivalent to $V_2 \sin i$, where V_2 is the true orbital velocity of the secondary and i is the inclination of the orbital plane to our line of sight. Having obtained these values, the *mass function* can now be introduced:

[1]It must be noted that the radial velocity curve is only sinusoidal if the orbit is circular. However, this is almost always the case for LMXBs if $P_{\rm orb} \lesssim$ 1d, as they circularise very quickly due to tidal and frictional forces between the two binary components.

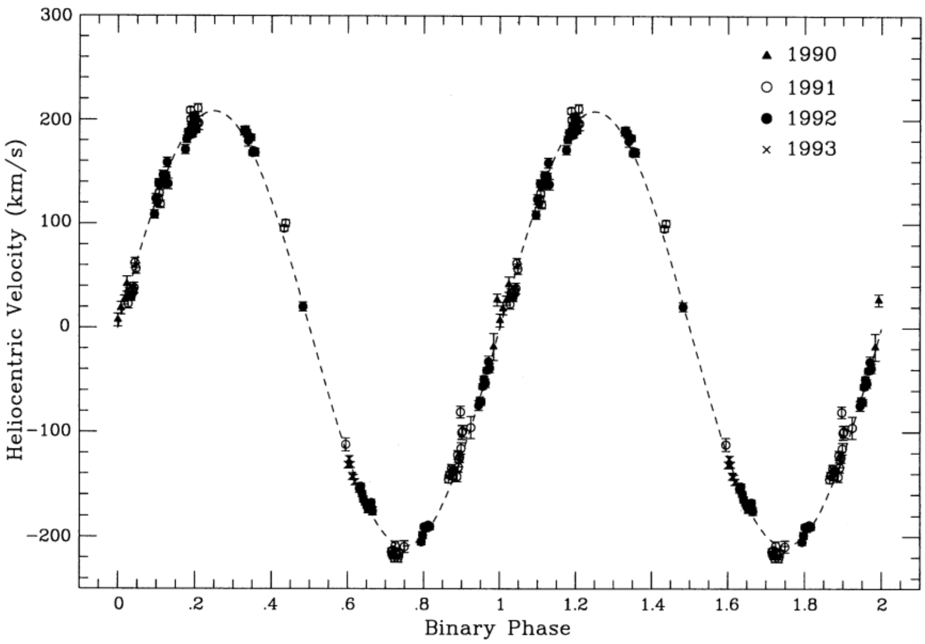

FIGURE 1.17: Radial velocity curve of the secondary star of V404 Cyg, folded on $P_{\rm orb} = 6.47$ days. Each symbol represents data sets acquired in different years with the 4.2m William Herschel Telescope on La Palma and a sinusoidal fit to the data is shown as a dashed line. Adapted from Casares & Charles (1994).

$$f(M) = \frac{P_{\rm orb} K_2^3}{2\pi G} = \frac{M_1^3 \sin^3 i}{(M_1 + M_2)^2} = \frac{M_1 \sin^3 i}{(1+q)^2} \tag{1.8}$$

where M_1 is the mass of the compact object, M_2 is the mass of the secondary and $q = M_2/M_1$ is the mass ratio of the binary components. In the case of LMXBs, if we assume a face on system ($i = 90°$) and a negligible mass secondary ($M_2 = 0$), then the mass function represents a firm lower limit to the mass of the compact object (i.e. $f(M) = M_1$). Therefore, if the mass function is calculated to be higher than $\sim 3M_\odot$ (the maximum mass of a NS Tolman, 1939; Oppenheimer & Volkoff, 1939; Wiringa et al., 1988; Kalogera & Baym, 1996) then the compact object *must* be a BH. The first such unambiguous discovery of a BH came from the 1989 outburst of the SXT GS 2023+338, better known by the name of its optical counterpart, V404 Cyg. When the source returned to quiescence, optical spectroscopy revealed the radial velocity variations of the late-type secondary star. The variations were large ($K_2 \sim 210$ km s^{-1}; see Fig. 1.17) and varied on a period of 6.47 days which was interpreted as the $P_{\rm orb}$ of the system. These two parameters alone gave a mass function $f(M) = 6.26M_\odot$, which is the absolute minimum mass for the compact object. V404 Cyg represents the first unambiguous discovery of a stellar mass BH (Casares et al., 1992).

The mass function only represents a lower-limit to the mass of the compact object, however. To calculate the true value of M_1, the values of i and q need to be accurately determined. q can be determined by measuring the *rotational broadening* of the absorption lines of the companion star. LMXBs are tidally locked due to the proximity of the binary components, meaning that the rotation period of the companion is identical to the $P_{\rm orb}$ of the system. The fast rotation of the companion star causes the absorption lines to be Doppler broadened and the level of this broadening, $V_{\rm rot} \sin i$ is directly related to q:

$$\frac{V_{\rm rot} \sin i}{K_2} = 0.462 q^{1/3} (1+q)^{3/2} \tag{1.9}$$

(Wade & Horne, 1988).[2] $V_{\rm rot} \sin i$ can be obtained by subtracting the spectral type template broadened by different velocities from the Doppler-corrected, averaged spectrum of the source and comparing the χ^2 residuals to find the best value (see e.g. Marsh et al. 1994; Casares & Charles 1994; Tomsick et al. 2002).

The final requirement to find the true value of M_1 is the binary inclination, i of the system. Unfortunately no SXTs are seen to be eclipsing, so the uncertainty in i dominates mass estimates. However, i can be estimated by studying the quiescent light curves of SXTs. The secondary star is heavily distorted as it fills its Roche lobe and therefore has a varying projected area as it orbits the compact object (see Fig. 1.18), giving rise to a double-humped orbital light curve, the so-called *ellipsoidal modulation*. The shape of the ellipsoidal light curve is largely dependent on binary inclination and accurate modelling can provide tight constraints on the value of i (see e.g. Shahbaz et al. 1994; Orosz & Bailyn 1997). With these techniques, the masses for 18 BHs in SXTs have been determined (Casares & Jonker, 2014; Mata Sánchez et al., 2015) and it has been found that $\sim 75\%$ of SXTs contain a BH (McClintock & Remillard, 2006).

1.3.4.1 Measuring masses during outburst: The Bowen Fluorescence Technique

In the previous section, I detailed the method for determining compact object masses in quiescent SXTs. However, detecting the companion star is more difficult in persistent LMXBs as the vast majority of the optical light emitted by the system originates from the accretion disc. This meant that bright sources such as Sco X-1, which was the first Galactic X-ray source ever discovered, had no constraints on the mass of the compact object. However, high-resolution phase-resolved optical spectroscopy revealed narrow

[2] Note: this assumes the donor is tidally locked and spherically symmetric, and is filling its Roche lobe.

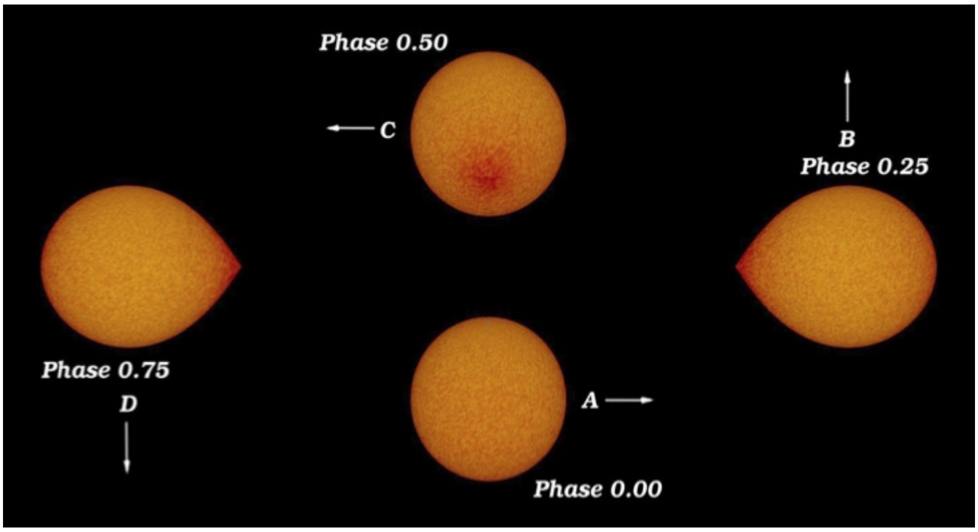

FIGURE 1.18: Illustration of the ellipsoidal variations in an LMXB depicting the distortion of the low-mass companion by the strong gravitational influence of the compact object. The companion adopts the shape of its Roche lobe and, as a result, projects a varying area with binary phase. The resultant light curve shows a double-humped structure due to the varying projected area of the star. Adapted from Seward & Charles (2010).

emission line components in the range $\lambda\lambda 4630 - 4660$, (Fig. 1.19) known as the Bowen blend (Steeghs & Casares, 2002). These narrow, high-excitation emission lines (a blend of C III and N III lines) were shown to move in anti-phase with lines from the compact object, strongly suggesting that they arise from the surface of the donor star, irradiated by the accretion disc. The resultant radial velocity curve then provided solid limits on K_2 and thus the mass of the compact object, confirming its NS nature.

Since the breakthrough with Sco X-1, the Bowen fluorescence technique has been applied to a number of persistent and two transient LMXBs leading to first estimates of the mass function (Cornelisse et al., 2008) for these sources. It must be noted, however, that the velocity determined from the narrow components is only a lower limit to K_2, as the lines arise on only one side of the irradiated donor star, which does not correspond to its centre of mass. This can by rectified by applying the so-called K-correction, which is dependent on q and the screening effects of a flared accretion disc (Muñoz-Darias et al., 2005).

1.3.4.2 Distribution of masses: The Mass Gap?

Using the techniques described in section 1.3.4, the masses of 18 BHs in SXT systems have been determined (Casares & Jonker, 2014; Mata Sánchez et al., 2015), as well as of many more NSs (Lattimer & Prakash, 2005; Özel et al., 2012). The resultant distribution of masses reveals a dearth of compact objects in the mass range $2 - 5 M_{\odot}$ (Farr et al.,

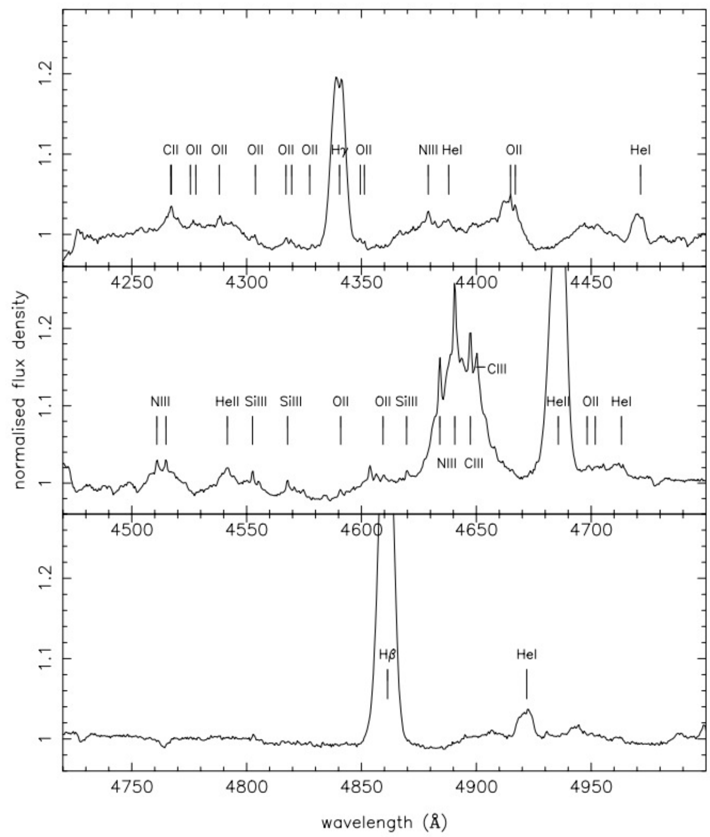

FIGURE 1.19: High-resolution optical spectrum of Sco X-1, showing the Bowen blend in the range $\lambda\lambda 4630-4660$ (middle panel). The N III lines are the result of UV fluorescence of the donor star by the accretion disc, while the C III lines are due to photo-ionisation and subsequent recombination (McClintock et al., 1975). Adapted from Steeghs & Casares (2002).

2011), the so-called 'mass gap' (see Fig. 1.20). The existence of a gap in this range is rather unexpected, as the mass range of pre-supernova massive stars is weighted to the lower end, so one would expect the same of the BH mass distribution (Fryer & Kalogera, 2001). The existence of the mass gap is a source of much debate - it is not clear whether it is the result of a selection bias or if it is real (Özel et al., 2010; Farr et al., 2011). If the gap is indeed real it prompts new questions about the formation scenarios of low-mass BHs in the context of supernova explosion models (Belczynski et al., 2012). For example, Kochanek (2014) presented a scenario in which red supergiants in the range $16.5 \leq M \leq 25M_{\odot}$ produce 'failed' supernovae whereby, instead of a standard core-collapse explosion, the star ejects its outer layers, leaving behind a BH with the mass of the star's He core ($5-8M_{\odot}$). This model would naturally explain the observed mass gap, as well as the apparent lack of supernova progenitors in the $16-25M_{\odot}$ mass range (Smartt et al., 2009).

To truly determine if the gap exists, accurate BH masses need to be measured for the large number of 'candidate' BHs, i.e. sources which exhibit the properties of BH systems

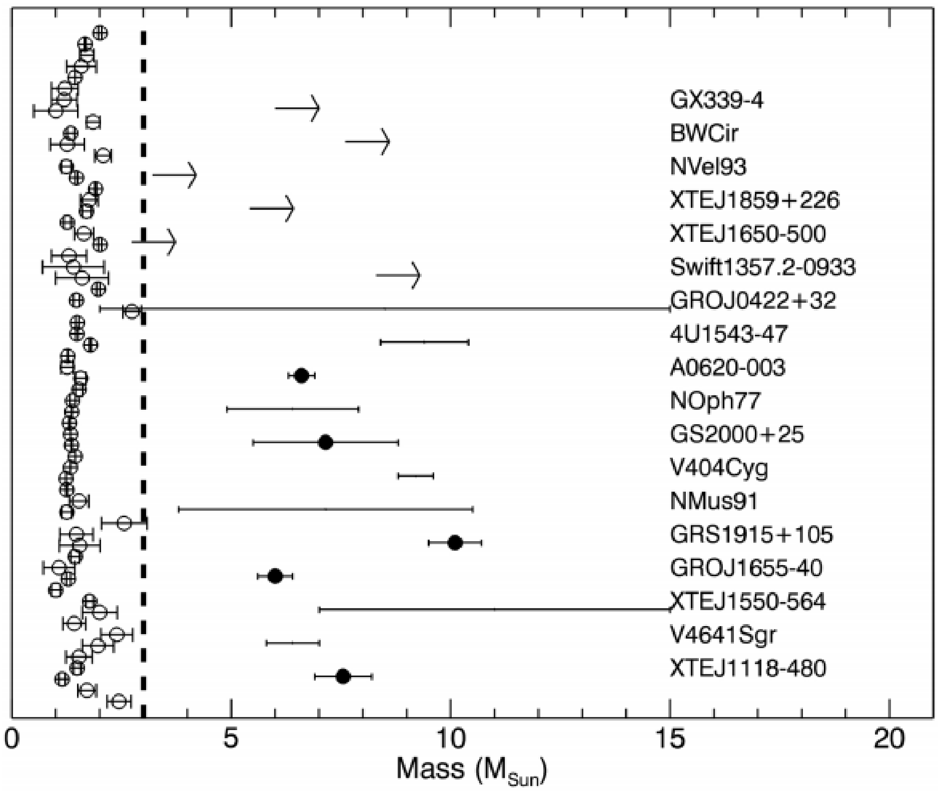

FIGURE 1.20: Distribution of observed compact object masses. The vertical dashed line represents the maximum mass allowed for NSs. Below the limit are the known masses of NSs (open circles; from Lattimer & Prakash, 2005; Özel et al., 2012; Antoniadis et al., 2013), whilst above it are reliable BH masses (solid circles; from Casares & Jonker, 2014). Arrows represent lower limits based on measured mass functions and upper limits to the inclination. Adapted from Corral-Santana et al. (2016)

but are not dynamically confirmed as such, as well as those with only a lower limit to their mass. A larger number of dynamically confirmed BHs will allow population studies, which are currently inhibited by the small sample size (Casares & Jonker, 2014; Corral-Santana et al., 2016). The main source of uncertainty with BH mass determination comes from the measurement of binary inclination, i, which can often be underestimated due to an underestimate of the contribution of disc emission to the quiescent (ellipsoidal) light curves (Kreidberg et al., 2012). This can, in turn, lead to a considerable overestimate of the BH mass due to the cubic dependence of the mass function with $\sin i$. Kreidberg et al. (2012) found that correcting the mass function of the BHXRT GRO J0422+32 based on the estimated bias in the inclination placed the source in the mass gap. This highlights the importance of careful interpretation of the ellipsoidal light curves.

1.3.5 Observational differences between BH and NS LMXBs

I have so far focussed mainly on BH systems when describing the observational characteristics of SXTs in this thesis. However, for completeness, I shall now briefly summarise some of the key differences between NS and BH LMXBs and SXTs. The key difference between a NS and a BH is the lack of a solid surface in BHs. When a BH is formed in a core-collapse supernova, the effective size is determined by the Event Horizon, so any material crossing this boundary will not be able to escape. Conversely, NSs, though compact, have a very well defined surface, as well as strong magnetic fields, which are responsible for a number of the observational characteristics of NSs, some of which I will describe here.

1.3.5.1 X-ray bursters

Some LMXBs are often identified through very occasional very rapid bursts of X-rays. These events are characterised by very short timescale ($\lesssim$ 1min) bursts of extreme energy (10^{39-40} ergs). The X-ray spectrum of one of these X-ray bursts is very similar to that of a blackbody, which is dependent only on temperature and radiating area. Using reasonable estimates for the distance to the burster and the blackbody temperature measured from spectral fitting, it was calculated that the emission must arise from the surface of a body whose radius is $\sim$ 10km (Swank et al., 1977). This is consistent with the size of a NS and the bursts must therefore arise from physical processes occurring on its surface. Therefore, any new SXT discovered that exhibits X-ray bursts is instantly classified as a NS.

The accepted model for X-ray bursts is one of unstable nuclear burning on the surface of a NS. In a NS LMXB, hydrogen is accreted on to the NS, which, as mass builds up, is compressed and heated enough to initiate nuclear fusion. Hydrogen fuses to helium and helium to carbon and oxygen in a series of thermonuclear runaways. The fusion of helium to carbon and oxygen is an unstable process, which results in a thermonuclear flash which is seen as the rapid rise of an X-ray burst (Woosley & Taam, 1976). After the flash, hydrogen continues to be accreted on to the surface of the NS and the process begins again. The burst recurrence rate is dependent on the rate at which matter is accreted on to the surface of the NS. An X-ray burster which accretes at $\dot{M} \sim 10^{-8} M_{\odot}$ yr^{-1} will have a burst recurrence time of $\sim$ 3 hours (see e.g. Cumming, 2003).

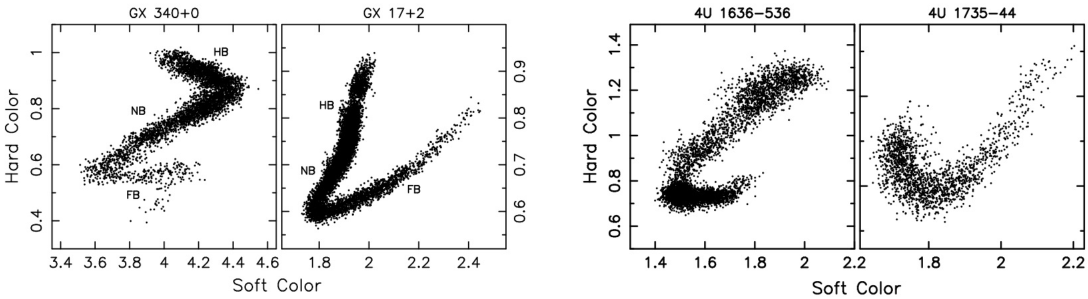

FIGURE 1.21: The X-ray colour-colour diagram for a sample of NS systems showing the Z-sources (left two panels) and atoll sources (right two panels). The Z-sources exhibit three distinct branches, the 'horizontal branch' (HB), the 'normal branch' (NB) and the 'flaring branch' (FB). Adapted from Hasinger & van der Klis (1989).

1.3.5.2 NS LMXB states

NS SXTs show state changes not unlike those in BHXRTs, tracing a 'q' shape on the HID, much like the example shown in Fig 1.13 (see e.g. Aql X-1; Tudose et al. 2009). However, there is another way to characterise X-ray states in NS systems; by studying the 'X-ray colour.' Examining the ratios of fluxes in higher and lower energy X-rays shows that different NS systems occupy different states on the X-ray colour-colour diagram. There are two classes of NS LMXBs, so-named after the shapes they trace on the colour-colour diagram (Hasinger & van der Klis, 1989). Z-sources trace out a 'Z' shape as their spectra vary with time, whilst atoll sources show various 'island' states as their spectra evolve (see Fig. 1.21).

The categorisation of Z and atoll sources roughly correlates with luminosity, with Z-sources exhibiting a substantially higher mass accretion rate than the lower luminosity atoll sources. The discovery of the SXT XTE J1701-462 showed that NS sources can actually move between the Z and atoll sub-classes, and this behaviour was dependent on source luminosity. At high (near super-Eddington) luminosities, XTE J1701-462 was seen to show Z-source like behaviour, but as the source decayed to quiescence it evolved towards a more atoll-like state. Spectral analysis strongly suggested that this transition between states was linked by only a single parameter; the mass accretion rate (Fridriksson et al., 2015).

1.4 Swift J1753.5-0127

Here I will introduce the source which will be the basis for the majority of the work presented in this thesis. Swift J1753.5-0127 was discovered by the *Swift* BAT in 2005 (Palmer et al., 2005) as a hard-spectrum (γ-ray source) transient at a relatively high

Galactic latitude (+12°). The source luminosity peaked within a week, at a flux of $\sim$ 200 mCrab, as observed by the *RXTE* All Sky Monitor (ASM, 2–12 keV; Cadolle Bel et al., 2007). The source was also detected in the UV, with *Swift*'s Ultraviolet/Optical Telescope (UVOT; Still et al. 2005), and in the radio with MERLIN (Fender et al., 2005). An $R \sim 15.8$ optical counterpart was identified by Halpern (2005), who noted that it had brightened by at least 5 magnitudes (as it is not visible in the Digitised Sky Survey; DSS), thereby establishing Swift J1753.5-0127 as an LMXB. Subsequent time-resolved photometry of the optical counterpart revealed R-band modulations on a period of 3.2h, which were interpreted as a superhump period, a periodicity only fractionally longer than the true $P_{\rm orb}$ of the system (Zurita et al., 2008). The presence of superhumps in the optical light curves of Swift J1753.5-0127 are indicative of an accretion disc that is precessing due to perturbations by the companion and have been seen to occur in other BHXRTs such as XTE J1118+480 (Zurita et al., 2002).

Almost immediately after its peak the X-ray flux of Swift J1753.5-0127 started declining, but this decline stopped when it reached $\sim$ 20 mCrab (2–12 keV), and where it then remained roughly constant for over 6 months rather than returning to quiescence as might have been expected for a typical BHXRT (Charles & Coe, 2006). The source has still not returned to quiescence, $\sim$11 years after its initial discovery, and has instead exhibited significant long-term variability over the course of its prolonged 'outburst' (see Chapter 2). Swift J1753.5-0127 has remained as a persistent LMXB in the hard state for the majority of this time, never transitioning to the soft state, even during the initial outburst. However, in March 2015, Swift J1753.5-0127 appeared to transition to a low luminosity soft state, showing characteristics previously unseen in the source (see Chapter 3).

With a large ($\Delta R \sim 5$ mag) optical increase at outburst, one would not expect to detect any spectroscopic signatures of the donor, due to the optical light being dominated by the accretion disc. Durant et al. (2009) confirmed this with spectroscopic observations revealing a smooth optical continuum and no evidence for features associated with the donor. With no detectable fluorescence emission either, it has not been possible to obtain any direct evidence of the compact object mass. However, *INTEGRAL* observations highlighted the presence of a hard power-law tail up to $\sim$ 600 keV, very typical of a black hole candidate (BHC) in the hard state (Cadolle Bel et al., 2007). Also, the power density spectrum from a pointed *RXTE* observation revealed a 0.6 Hz quasi-periodic oscillation (QPO) with characteristics typical of BHCs (Morgan et al., 2005). QPOs have also been seen at 0.08 Hz in optical data (Durant et al., 2009) as well as in a number of X-ray observations after the initial outburst had declined (Ramadevi & Seetha, 2007; Cadolle Bel et al., 2007).

Recently, Neustroev et al. (2014) reported on evidence for a low mass ($< 5M_{\odot}$) BH in Swift J1753.5-0127, based on observations of narrow features in the optical spectrum which they associate with the donor, despite such features not being identifiable or visible in previous spectroscopic studies (Durant et al., 2009). The observations by Neustroev et al. (2014) of apparent features associated with the donor, despite the source not being in quiescence, was surprising and if found to be true would have serious implications for the observed BH mass gap (section 1.3.4.2). My attempt to replicate and understand the results of Neustroev et al. (2014) is the subject of Chapter 5.

Given the high Galactic latitude of Swift J1753.5-0127, Cadolle Bel et al. (2007) concluded that its distance is likely 4–8 kpc. However, in recent work fitting the UV spectrum with an accretion disc model and assuming a $5M_{\odot}$ BH, Froning et al. (2014) obtain a distance of < 2.8 kpc and < 3.7 kpc for a binary inclination of $i = 55°$ and $0°$, respectively.

1.5 Thesis Outline

This thesis will mainly focus on Swift J1753.5-0127 as I undertake a multi-wavelength approach to understand the underlying physics behind the source. In this chapter I have introduced the concepts of accretion and spectral state changes, which provides the background for chapters 2 and 3 in which I discuss the presence of a long-term 'super-orbital' modulation in the optical and X-ray light curves of Swift J1753.5-0127 as well as a low-luminosity transition to a soft accretion state. Chapter 4 introduces the apparent correlation between X-ray and radio luminosity in such sources, and I test this correlation using long-term monitoring of Swift J1753.5-0127 with multiple radio telescopes. I have also discussed here the methods required to measure the mass of the compact object in SXTs and in chapter 5 I utilise such methods to challenge the evidence for a low mass BH in Swift J1753.5-0127 presented by Neustroev et al. (2014).

In chapters 6 and 7, I move away from my study of Swift J1753.5-0127 and focus on other SXTs. In chapter 6 I utilise optical spectroscopy and photometry of V404 Cyg, the first dynamically confirmed BH, in order to test the DIM, which I discuss here in section 1.3.1. Finally, in chapter 7 I present X-ray observations of the candidate BH MAXI J1305-704 and attempt to determine its $P_{\rm orb}$ by utilising the timing analysis techniques introduced here in section 1.3.3.1.

Chapter 2

A 420 day X-ray/optical modulation and extended X-ray dips in the short-period transient Swift J1753.5-0127

"I read of one planet in the seventh dimension got used as a ball in a game of intergalactic bar billiards. Got potted straight into a black hole, killed ten billion people."

Ford Prefect - The Restaurant at the End of the Universe

In this chapter I present archival optical and X-ray monitoring of the Galactic BHXRT Swift J1753.5-0127, a short-period LMXB which has been the main focus of the majority of my PhD research. I report on the discovery of a long-term super-orbital periodicity present in soft and hard X-ray light curves, as well as optical data. I also report on the presence of two substantial X-ray dips in the hard X-ray light curves and speculate on their nature. I interpret the long term periodicity as a property of the accretion disc, most likely a long-term precession. Such precession indicates a very low mass ratio LMXB, which even for a $\sim 10M_\odot$ BH requires a $\sim 0.02M_\odot$ donor.

2.1 Introduction

As discussed in Section 1.4, Swift J1753.5-0127 is an unusual source which outburst in 2005 and has not yet returned to quiescence. Since the original outburst, the source has exhibited significant long-term variability which is the subject of this chapter. Here I report on the discovery of a 420 day modulation present in archival optical and X-ray light curves of Swift J1753.5-0127. I also discuss the nature of two short-term dips discovered in the hard X-ray light curves, which are also separated by 420 days - the same timescale as the super-orbital modulation.

2.2 Observations and Analysis

2.2.1 Observations

Swift J1753.5-0127 has been more or less continually observed by multiple X-ray to γ-ray instruments since its original outburst in 2005. Public data from the Monitor of All-Sky X-ray Image (MAXI; 2–20 keV), *Swift*-BAT (15–50 keV) and the *RXTE*-ASM (2–12 keV) have been used to produce the $\sim$ 7yr light curves presented here. The data required no significant processing and are all available online. [1,2,3]

Swift J1753.5-0127 was also observed by the two 2m robotic Faulkes Telescopes (FT) North (located at Haleakala on Maui) and South (at Siding Spring, Australia), which are now part of the Las Cumbres Observatory Global Telescope (LCOGT) network (e.g. Lewis et al. 2010). Photometry was performed in the *i'*, R and V-bands and the data were reduced using the FT pipeline. Additional optical data were obtained with the 80cm IAC-80 telescope at the Observatorio del Teide on Tenerife, and both the 1.5m and 0.84m telescopes at the Mexican Observatorio Astronómico Nacional on San Pedro Mártir (Zurita et al., 2008). Swift J1753.5-0127 has also been monitored in the H, I and V-bands with the Small and Moderate Aperture Research Telescope System (SMARTS) at Cerro Tololo (Hynes et al., 2009a; Soleri et al., 2010).

2.2.2 Light Curves

The 7 year X-ray light curve of Swift J1753.5-0127 is shown in 5-day bins in Figure 2.1 and exhibits a profile typical of XRTs in outburst i.e. a FRED, or Fast Rise, Exponential Decay profile, with a peak at $\sim$ 200mCrab (Ramadevi & Seetha, 2007). However, following the initial outburst the flux stalled at $\sim$ 20mCrab for several months before it then started gradually increasing again. This behaviour is present in both the BAT and ASM light-curves. Then, just after MJD $\sim$ 54500, there is a significant increase in flux, following which the light curve begins to exhibit a modulation with a period of $\sim$ 400d.

[1]http://maxi.riken.jp/top/
[2]http://heasarc.nasa.gov/docs/swift/results/transients/
[3]http://xte.mit.edu/

The sudden increase in X-ray flux has been noted before (Krimm et al., 2008; Negoro et al., 2009), but the long-term variability has not previously been investigated.

I selected X-ray data for timing analysis by excluding the initial outburst/FRED portion, i.e. I use all data after MJD 54000 (see Fig. 2.1). The periods and their errors are determined using a Lomb-Scargle (LS) analysis to determine a central peak frequency, and then performing a Monte-Carlo simulation based on 'bootstrap-with-replacement.' In this method a subset of the light curve is constructed from a random 2/3 of the original dataset to re-perform the periodogram analysis on, whilst allowing data points to be selected multiple times (i.e. the data point is *replaced*, back into the original light curve once selected). In each mock data set the number of points is exactly the same as in the original data set, but with some points occuring more than once. The distribution of peak frequencies resulting from 10000 iterations of this process is used to determine the error on the peak frequency. A LS power spectrum is also calculated using the available optical data in the combined R-band and FT *i'*-band data, as observations of the source in both these filters exhibited almost identical values. As seen in Figure 2.2, there is a clear peak in both X-ray periodograms at 416.4±2.1d (BAT) and 422.8±2.3d (combined MAXI/ASM). The power spectrum of the combined optical data also exhibits a peak at a period of 419.2 ± 3.5d; however, whilst the peak power is still significant, it is lower than that in both X-ray power spectra, and the periodogram is noisier. Nevertheless, it should be noted that these datasets are entirely independent of each other.

When the light curves are folded on $P = 422.8$ days (Fig. 2.3) it becomes clear that the peak of the hard X-ray light curve (*Swift*-BAT) precedes that at lower energies (MAXI/ASM) by $\sim 0.1 - 0.2$ phase ($\approx 40 - 80$d). There is also evidence of potential dipping structure in the folded *Swift*-BAT light curve, which I explore further in section 2.2.3. The folded optical light curve shows evidence of a tentative anticorrelation between the optical and the hard X-ray flux, with a correlation coefficient $r \approx -0.3$ (at 95% confidence), with a similar value of r being calculated for the optical vs. MAXI data. The confidence level was determined from the two-tailed p-value calculated alongside the Pearson r coefficient.

2.2.3 X-ray dips

One of the most remarkable features of the *Swift*-BAT light curve of Swift J1753.5-0127 is the presence since MJD ~ 55500 of two extended X-ray dips, which are separated by 420 days, an interval that is fully consistent with the long term modulation discussed in section 2.2.2. These dips last for ≈ 25 days and are almost a full eclipse of the hard X-ray flux, and occur at the maximum of the MAXI/ASM modulation. The dips in the

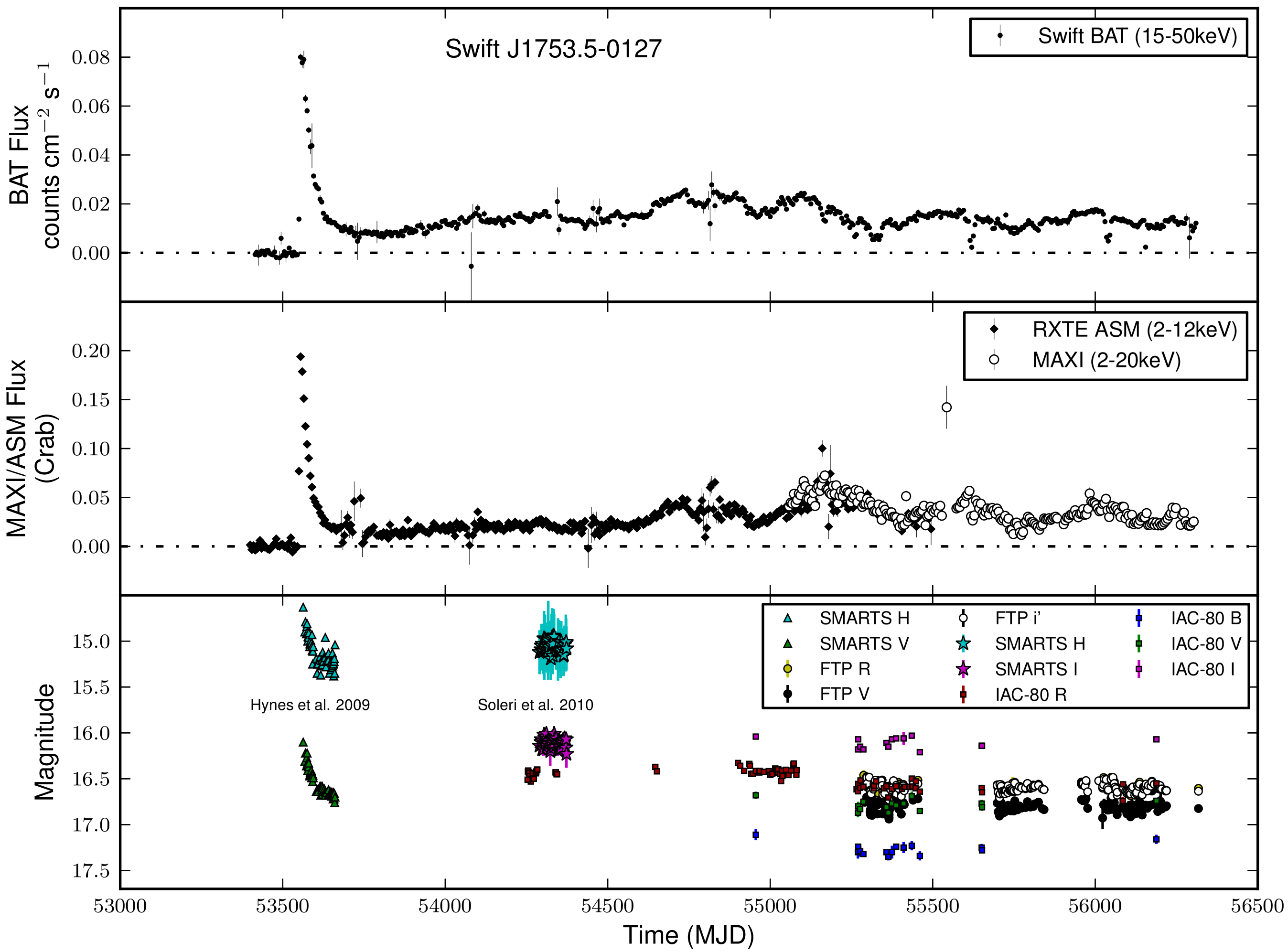

FIGURE 2.1: *Upper panel:* 15 - 50 keV *Swift*-BAT light curve of Swift J1753.5-0127 spanning approximately 7 years from 30 Jan 2005 - 11 Jan 2013, using 5d binning. *Centre panel:* Combined *RXTE*-ASM (diamonds, 2-12 keV) and MAXI (open cirles, 2-20 keV) light curves, with both normalised to the Crab, again with 5d binning. *Lower panel:* Combined optical and near-IR photometry of Swift J1753.5-0127 from SMARTS (cyan (H) and green (V) triangles, (Hynes et al., 2009a); cyan (H) and magenta (I) stars, (Soleri et al., 2010)), IAC-80 (magenta (I), red (R), green (V) and blue (B) squares) and FT (yellow (R), white *i'* and black (V) circles). In the upper and centre panels the dash-dotted line marks zero flux.

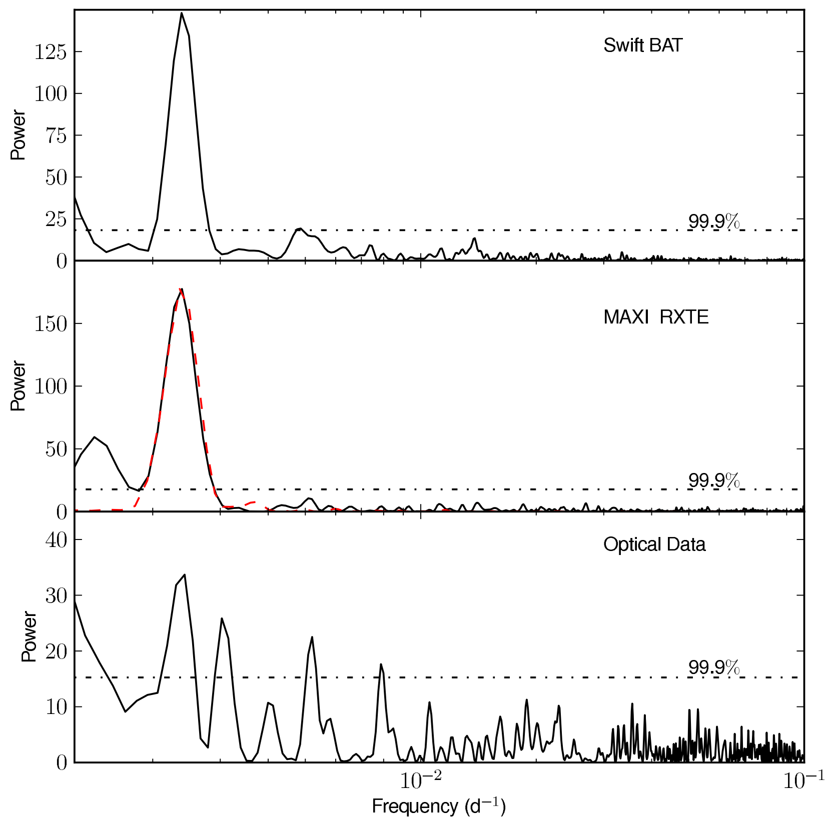

FIGURE 2.2: *Upper panel:* LS periodogram of the selected *Swift*-BAT data of Swift J1753.5-0127 (see text). *Centre panel:* The solid line shows the periodogram of the combined RXTE ASM and MAXI light curves, whilst the red dashed line is a periodogram of a sine curve with the same period. *Lower panel:* periodogram of the combined R and *i'*-band data of Swift J1753.5-0127 from Fig. 2.1. In all three plots the dash-dotted lines represent the 99.9% confidence level. Both *Swift*-BAT and MAXI/ASM power spectra exhibit rising power at very low frequencies; this is due to the gradual rise in flux during the data window.

Swift-BAT light curve at MJD $\sim$ 55625 and $\sim$ 56045 are clearer in the more detailed Fig. 2.4, where related, but weaker, features in the lower energy MAXI light curve can also be seen. The MAXI feature is more significant in the first dip ($\sim$ 30 mCrab) than in the second. Dips on this timescale are not visible anywhere else in the near 7 year light curves of the source in either X-ray energy band, which is why they are not immediately obvious in the folded *Swift*-BAT light curve in Fig. 2.3. Figure 2.4 also includes contemporaneous optical monitoring data that has been obtained with FT and IAC-80. There is no evidence for an optical response at the time of the second hard X-ray dip (the first dip is not contemporaneous with optical observations).

2.3 Discussion

2.3.1 The 420d modulation

Swift J1753.5-0127 is a unique candidate BHXRT in that the source has not returned to quiescence like most transients, but instead is now exhibiting a substantial long-term modulation over a wide range of energies on a period of $\sim$ 420d. Since $P_{\rm orb} \approx 3.2$h is known (Zurita et al., 2008), it must be noted that this modulation is a "super-orbital" periodicity of the kind that has now been seen in a significant fraction of XRBs. There are a variety of mechanisms that can give rise to long-term (tens to thousands of days) variations in all types of XRBs (see e.g. Charles et al. 2010; Kotze & Charles 2012), but the most likely cause in this case is disc precession as a result of the extreme mass ratio in BH LMXBs. Such behaviour is well-established in the CV analogues of LMXBs, the SUMa systems, which exhibit "superhumps" on periods very slightly longer than $P_{\rm orb}$ (see e.g. Warner 1995), as a result of the disc expanding outside its tidal stability radius (for full details see e.g. Whitehurst & King 1991). More importantly, Patterson et al. (2005) demonstrated an observational link between the period difference (i.e. $P_{\rm sh} - P_{\rm orb}$) and mass ratio $q = M_2/M_1$ (where M_2 and M_1 are the masses of the companion and the compact object, respectively), and this relationship has been extended from CVs to LMXBs. Indeed, it was applied by Zurita et al. (2002) in their analysis of XTE J1118+480.

Consequently, the presence of such long-term timescales in BHXRTs is taken as evidence of a precessing accretion disc, and hence can be extremely important in being able to provide an indication of q without any direct kinematic measurements. Zurita et al. (2008) claimed a tentative precession period of 29d from their R-band photometry. This can be interpreted as the beat between the orbital and superhump frequencies i.e. $P_{\rm prec} = (P_{orb}^{-1} - P_{sh}^{-1})^{-1}$, giving $P_{\rm orb} = 3.23$h for the observed $P_{\rm sh} = 3.2443$h. This would imply $q = 0.025$, using $\Delta P = (P_{\rm sh} - P_{\rm orb}/P_{\rm orb}) = 0.18q + 0.29q^2$ (Patterson et al., 2005). If instead the Patterson relation is re-applied using the $\sim$ 420d modulation as $P_{\rm prec}$, I find that this gives a much more extreme $q \sim 0.002$. If the compact object is a typical $\sim 10M_\odot$ BH (Farr et al., 2011), then the donor has a mass of $\sim 0.02M_\odot$, and would itself be highly evolved.

Such an extreme q draws comparisons of Swift J1753.5-0127 with SAX J1808.4-3658, the first accreting millisecond X-ray pulsar (AMXP), with $P_{\rm orb} = 2$h (Chakrabarty & Morgan, 1998). With an estimated donor mass $M_2 \approx 0.05M_\odot$ (Bildsten & Chakrabarty, 2001), I suggest that Swift J1753.5-0127 is a BH analogue to this AMXP system, taking the mass ratio to new extremes. If this is the case, a $0.02M_\odot$ brown dwarf (BD) donor would require a radius of $\approx 0.10R_\odot$ to sustain Roche Lobe overflow (following Bildsten

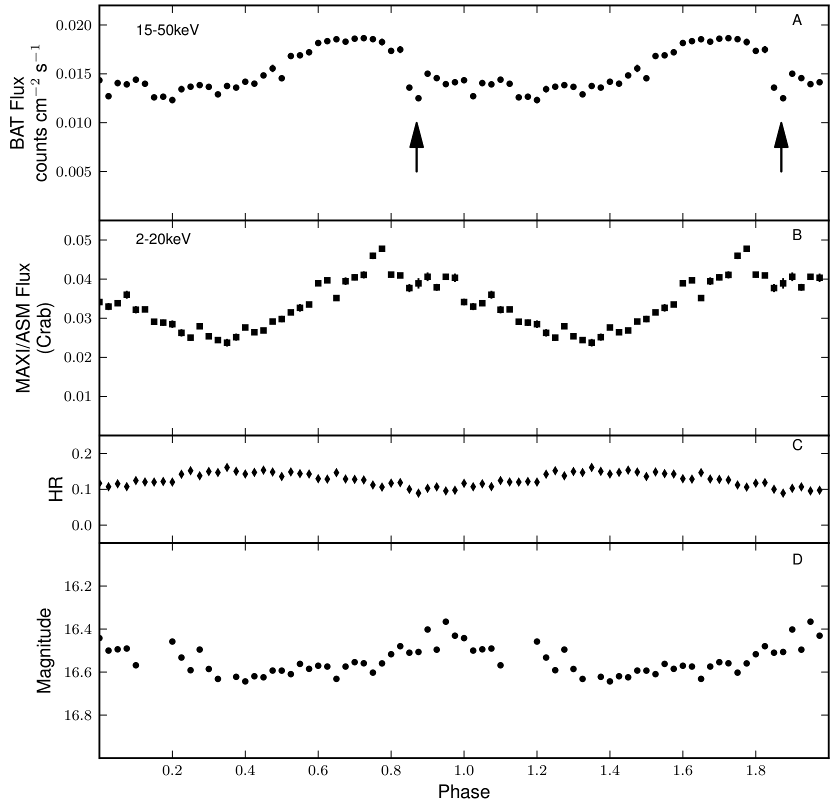

FIGURE 2.3: *Panel A: Swift*-BAT light curve of Swift J1753.5-0127 folded on a period of 422.8 days (as determined from the MAXI/ASM periodogram in Fig. 2.2), with arrows marking the location of hard X-ray dips that are discussed in the text. *Panel B:* Combined MAXI & ASM light curve of Swift J1753.5-0127 folded on the same period. *Panel C:* Hardness Ratio (HR) defined as BAT count rate/MAXI & ASM count rate. *Panel D:* Combined R and Faulkes *i'*-band light curves of Swift J1753.5-0127 folded on the same period. In all panels, each bin represents ≈ 10 days.

& Chakrabarty, 2001), and this is consistent with the M-R relation of low-mass stars and sub-stellar objects detailed by Chabrier et al. (2009).

Another mechanism considered for the long-term modulation of Swift J1753.5-0127 is that of irradiation-driven warping. In this case an initially flat accretion disc is unstable to warping when irradiated by a central source, as the warp then excites the tilt of the disc continuously, thereby leading to precession (Ogilvie & Dubus, 2001; Foulkes et al., 2006). This model was used to simulate real binary systems with observed or inferred super-orbital periods by Foulkes et al. (2010), who found they could account for observed X-ray properties for a given super-orbital period (P_{sup}). However, high q systems were found to have the shortest P_{sup} out of all XRBs examined, and knowing that the donor of Swift J1753.5-0127 must be very low mass (it is not visible on the DSS), it is unlikely that this scenario applies to J1753.

2.3.2 Properties of the 420d modulation

The folded light curves in Fig. 2.3 show that the hard X-ray emission leads that at lower energies, but the hardness ratio (HR) modulation (Fig. 2.3, panel C) shows that this could also be interpreted as a smooth spectral variation. This is reminiscent of that seen in 4U 1636-536, an LMXB with a 3.8h period that displays long-term variability on timescales of $30-40$d (Belloni et al., 2007). Remarkably, while the long-term variability was found at both soft ($2-12$ keV, RXTE ASM) and hard ($20-100$ keV, INTEGRAL IBIS) X-ray energies, it was also found to be anticorrelated (Shih et al., 2005). The long-term variation was initially suggested to be due to a tilted or warped, precessing accretion disc (Shih et al., 2005), and the measured mass ratio allowed for this hypothesis (Casares et al., 2006). However, the variations were not stable, and coupled with the anticorrelation between soft and hard X-rays, it is difficult to interpret as a precessing disc (Shih et al., 2011). Regardless of the nature of the long-term variations, the soft/hard X-ray anticorrelation seen in the 4U 1636-536 light curves suggests physically separate emission regions responsible for hard and soft X-rays, a hypothesis which can be applied to J1753. This theory is further strengthened by the presence of strong X-ray dips in the *Swift*-BAT light curve of J1753, but only weak dips in the softer MAXI light curve.

2.3.3 Hard X-ray dips

The hard X-ray dips could be attributed to a warped disc structure that obscures the hard X-ray emitting region entirely whilst leaving the softer region mostly visible. It can be assumed that the dips do not appear earlier in the overall light curve as the warp was not yet established at that time. The dip light curves can be used to place constraints on the size of the hard X-ray emitting region if I adopt my derived value of q. Assuming that the obscuring material is located at the edge of the disc ($R_1 \approx 1.8R_{\odot}$), the angle swept out by the warp would be $\sim 21^{\circ}$, from which I roughly estimate a hard X-ray emitting region size of $\sim 0.3\ R_{\odot}$. However, I note that the lack of similar scale dips at lower energies implies that the latter is from a significantly more extended region.

I also note that the dips are prominent in the HR light curve (Fig. 2.4, panel C), which shows similar behaviour in the more extended, but shallower dip at MJD $\sim$ 55300. Interestingly this is the interval when Soleri et al. (2013) observed spectral state changes, and so these dips could all be related to such behaviour, although it is not clear why this would be periodic.

Finally I note that the 420d separation of the two dips may be consistent with Lense-Thirring precession at the Bardeen-Petterson radius (Bardeen & Petterson, 1975). It is

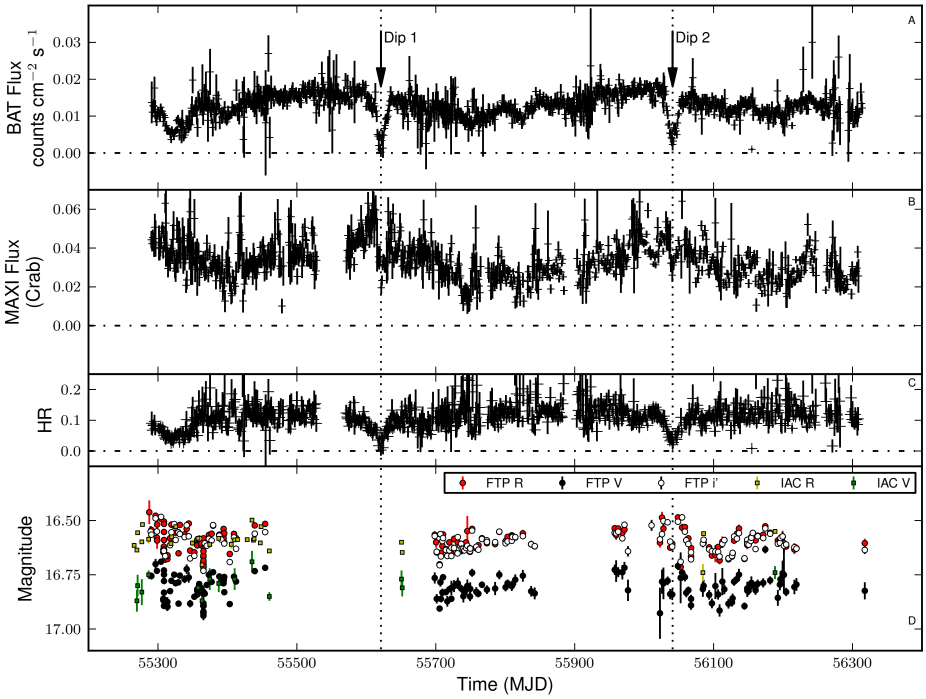

FIGURE 2.4: *Panel A: Swift*-BAT light curve (15 - 50 keV) of Swift J1753.5-0127 with 1d binning. *Panel B:* 2 - 20 keV light curve of Swift J1753.5-0127 from MAXI, also in 1d bins. *Panel C:* Hardness Ratio (HR) defined as BAT count rate/MAXI count rate. *Panel D:* Optical photometry of Swift J1753.5-0127 from the IAC-80 (yellow (R) and green (V) squares) and FT (red (R), black (V) and white (*i'*) circles). In panels A, B and C, the dash-dotted line marks the zero point and the vertical dotted lines highlight the minimum of the dips.

at this radius that frame-dragging effects from the rapidly rotating BH can give rise to a twisted, warped structure in the inner disc, which has been linked to the QPOs seen in many XRBs (Fragile et al., 2001), and could offer an explanation for the hard X-ray dips. Linking the 0.6Hz QPO seen in Swift J1753.5-0127 with the Bardeen-Petterson radius would place it at $\sim 200\ R_s$ (where R_s is the Schwarzschild radius of the BH) for a typical BH mass, which could have a Lense-Thirring precession period comparable to the observed 420d. However, these values are highly dependent on the scaling and spin parameters of the BH as described in Equation 4 of Fragile et al. (2001) and such effects have never been seen at these timescales.

2.3.4 Comparison with other high-latitude X-ray transients

The last decade has seen the emergence of a number of short period BHXRTs which can be compared with Swift J1753.5-0127. Interestingly these are all at high Galactic latitude and hence located in the halo (Table 2.1), and may represent a sub-class of

Table 2.1: BHXRTs in the Galactic Halo

Source	F_x [a] (mCrab)	b	d (kpc)	v_D [b] ($km\ s^{-1}$)	$P_{\rm orb}$ (hr)	$P_{\rm sup}$ (d)	q	M_1 ($M_\odot$)	i	M_2 ($M_\odot$)
GRO J0422+32[1]	3000	$-12°$	~ 2.5	400	5.1	?	0.075	~ 4	$45°$	0.3
XTE J1118+480[2]	~ 40	$+62°$	~ 1.8	600	4.1	~ 52	< 0.025	8	$68°$	0.2
MAXI J1305-704[3]	~ 30	$-7°$	?	500*	?	?	?	?	?	?
Swift J1357.2-093313[4]	~ 30	$+50°$	~ 1.6	900	2.8	?	< 0.06	> 3	$\geq 70°$	0.2
MAXI J1659-152[5]	~ 50	$+16°$	8.6	?	2.4	?	< 0.08	> 3	$\sim 65° - 80°$	$0.15 - 0.25$
Swift J1753.5-0127	~ 200	$+12°$	~ 8	600	3.2	~ 420	~ 0.002	~ 10	?	~ 0.02

Note: [a] Peak X-ray flux, [b] Disk edge velocity estimated from H_α double peak separation (Warner, 1995).
* denotes that v_D was estimated from HeII emission.
[1]Gelino & Harrison 2003, [2]Zurita et al. 2002, [3]Charles et al. 2012, [4]Corral-Santana et al. 2013, [5]Kuulkers et al. 2013

BHXRTs which are difficult to find in soft X-ray surveys, but are seen by *Swift*-BAT in the LH state.

It is interesting to note that 4 of the 6 sources listed show dipping structure. Swift J1357.2-093313 exhibits very fast optical dips (∼2-8min) and these cannot be Keplerian at the outer disc, but must be in the inner disc region (Corral-Santana et al., 2013). Swift J1357.2-093313 shows no X-ray dips and thus must have a very high i, requiring that the central BH is hidden from view completely, and thus only scattered X-rays are seen from the ADC (section 1.3.2), accounting for the low peak $F_x \sim$ 30mCrab, making such systems hard to detect.

On the other hand, MAXI J1659-152 exhibits X-ray dips suggestive of a disc edge structure, hence the range in i shown in Table 2.1. This highlights the importance of considering the geometry of such systems, as one would not expect this high a fraction of dipping sources within the sample.

2.4 Recent Developments

Since the publication of this work, there have been a number of attempts to understand the nature of the dipping structure in the hard X-ray light curves. As noted above, Soleri et al. (2013) discovered a short-term spectral state change (dubbed 'failed state transitions') at MJD $\sim$ 55300, characterised by a softer spectrum and a lower level of variability (fractional rms $\sim$ 15%) than in a typical Swift J1753.5-0127 hard state. Yoshikawa et al. (2015) investigated a second of these failed state transitions with *Swift*, discovering an increase in the temperature of the inner accretion disc and simultaneous steepening of the power law component of the X-ray spectrum as it progressed through the transition. This particular failed state transition was simultaneous with the first hard X-ray dip presented here at MJD 56045 and supports the hypothesis that the dips are related to a state transition in the source. In March 2015, the *Swift*-BAT flux of Swift J1753.5-0127 began to drop again, suggesting that the source was transitioning once more. However, rather than entering a hard intermediate state (e.g. Soleri et al. 2013; Yoshikawa et al. 2015), the source instead transitioned to the soft state for the first time in its outburst history. This soft state is discussed in detail in Chapter 3.

At the time of the publication of this work, the X-ray dips were hypothesised to be a periodic phenomenon, as they appeared to be separated by the $\sim$ 420 day periodicity discussed above. For this reason, it was expected that the next dip would occur in June 2013. However, the source remained in the hard state and appeared to show no signs of a state transition. It therefore remains unclear as to why the two hard X-ray dips are separated by the super-orbital period.

2.5 Conclusions

The LMXB Swift J1753.5-0127 has exhibited a strong, long-term ($\sim$ 420 day) periodicity over the course of its prolonged 'outburst.' I discuss this in the context of a precessing accretion disc, which, if true, requires a highly evolved (possibly brown dwarf) companion. I also report on the discovery of two hard X-ray dips in the *Swift*-BAT light curves, with a weak response in the lower energy MAXI light curves. These dips are separated by the super-orbital periodicity and have recently been attributed to failed state-transitions (Soleri et al., 2013; Yoshikawa et al., 2015). It is not clear why the dips appeared to be associated with the super-orbital modulation, as such state transitions were not seen again until the source entered the soft state in 2015 (Chapter 3).

Chapter 3

A low-luminosity soft state in the short period black hole X-ray binary Swift J1753.5-0127

"Last night, Darth Vader came down from Planet Vulcan and told me that if I didn't take Lorraine out, that he'd melt my brain."

George McFly - Back to the Future

In this chapter I present recent *XMM-Newton* and *NuSTAR* observations of Swift J1753.5-0127 in a spectral state previously unseen in this source. The X-ray spectral analysis reveals the emergence of a strong disc-dominated component scattered into an extremely soft, steep ($\Gamma = 6.39^{+0.08}_{-0.02}$) power law with an additional hard power law tail ($\Gamma = 1.79 \pm 0.02$). I conclude that Swift J1753.5-0127 has entered the soft state for the first time in its unusually prolonged outburst. Using reasonable estimates for the distance to the source and BH mass, I calculate the unabsorbed luminosity to be 0.72% of the Eddington luminosity, making this one of the lowest luminosity soft states recorded in X-ray binaries. I also find that the accretion disc has extended towards the BH during the transition from hard to soft, with an inner disc radius estimated to be $R_{\text{in}} \sim 11 - 35R_g$, dependent on the boundary condition chosen.

3.1 Introduction

This chapter continues my study of Swift J1753.5-0127 from chapter 2. Since the publication of chapter 2 in Shaw et al. (2013), Swift J1753.5-0127 has remained active and has continued to exhibit long term variability. In early 2015, the *Swift*-BAT flux of Swift J1753.5-0127 dropped to its lowest levels since the source's discovery (Onodera et al., 2015). Subsequent follow-up with the *Swift* X-ray telescope (XRT; Burrows et al. 2005) revealed a dramatic increase in the soft band (0.6–2 keV) flux whilst the contribution from the 2–10 keV band had dropped to only ∼10% of the total flux (Shaw et al., 2015), suggesting that the source was entering a soft state for the first time.

In a study of several BHXRTs by Kalemci et al. (2013), the transition luminosity between soft and hard spectral states was found to be $1 - 3\%$ $L_{\rm Edd}$ for the majority of systems. The lowest luminosity soft state in this particular study was seen at 0.3% $L_{\rm Edd}$ (3–200 keV) for XTE J1720-330 but this was the only source seen in a soft state at an Eddington fraction $< 1\%$. In a further study, the BHXRT 4U 1630-47 was observed in a soft state at an unusually low (0.5–200 keV) luminosity $L/L_{\rm Edd} = 0.03\%$ (for a 10 $M_{\odot}$ BH) and to date this is the lowest luminosity at which a BH has been observed in the soft state.

In this chapter I present a spectral study of Swift J1753.5-0127 during its 2015 prolonged state transition, which shows characteristics previously unseen in this source. I utilise observations from the *Swift*-XRT and near simultaneous data from *XMM-Newton* (Jansen et al., 2001) and the *Nuclear Spectroscopic Telescope Array* (*NuSTAR*; Harrison et al. 2013). I focus in particular on the emergence of a soft component at a low Eddington fraction, which dominates the 0.7–78 keV spectrum. This places Swift J1753.5-0127 in the emerging population of sources which exhibit extremely low-luminosity ($L/L_{\rm Edd} \lesssim 1\%$) soft states.

3.2 Observations and Data Reduction

3.2.1 Swift

I utilised 173 observations of Swift J1753.5-0127 made with the *Swift* Gamma-ray Burst Mission (Gehrels et al., 2004) between 2005 July 02 and 2015 July 30. *Swift* consists of two pointing telescopes – the XRT and UVOT (Roming et al., 2005) – as well as the larger field of view (FoV) coded-mask detector, BAT. For the purposes of this work I have used a number of archival XRT observations (Target IDs: 00030090, 00031232 and 00033140) and I have also monitored the 15–50 keV flux with the BAT.

I created a long-term *Swift*-XRT light curve using the online light-curve generator provided by the UK *Swift* Science Data Centre (UKSSDC; Evans et al. 2007), which is presented in Fig. 3.1, along with corresponding light curves from the *Swift*-BAT transient monitor. Hardness ratios were obtained by filtering *Swift*-XRT light curves in to "hard" (1.5–10 keV) and "soft" (0.3–1.5 keV) energy bands which I use to construct a hardness-intensity diagram (HID), presented in Fig. 3.2. All *Swift*-XRT data were grouped into 1d bins and distinct epochs are represented in the light curves by different symbols and their corresponding hardness ratio (HR) presented in the HID with identical notation.

I also extracted spectra of Swift J1753.5-0127 from *Swift*-XRT observations during three epochs. *Swift* observed the source in windowed timing (WT) mode on 2015 March 17, near simultaneous to the *XMM-Newton* observation described below, on 2012 April 24 at the peak of a failed state transition (Yoshikawa et al., 2015) and on 2013 June 18 during the hard state. Data were processed using HEASOFT v6.16 and count rates were extracted with the task XSELECT using a circular region 20 pixels in radius ($\approx 47''$). The background count rate was extracted from an identically sized source-free region. Spectra were grouped to have a minimum of 20 counts per energy bin. The details of all the spectral observations of Swift J1753.5-0127 are presented in Table 3.1.

3.2.2 XMM-Newton

A Director's Discretionary Time (DDT) observation of Swift J1753.5-0127 with *XMM-Newton* was performed on 2015 March 19 starting at 02:11 UTC (Obs ID: 0770580201) for a total of 42 ks. For this work I utilised data from the European Photon Imaging Camera (EPIC) pn detector (0.15–12 keV; Strüder et al., 2001), which operated consecutively in timing (32 ks) and burst (10 ks) modes. Data were reduced using SAS v14.0.0.

The SAS tool EPPROC was used to extract the event files from the timing mode data, which were then filtered for flaring particle background and to keep events between RAWX columns 25 and 47. A light curve was extracted with the SAS task EVSELECT and I found an average count rate of ~ 600 counts s^{-1}. I therefore examined the filtered events for evidence of photon pileup with the task EPATPLOT. Significant pileup was detected in the timing mode data. To reduce the effects of photon pileup, I removed the central five RAWX columns from the data and filtered them to only include single and double pattern events (PATTERN $\leq$4). With the central five columns removed, the average count rate decreased to ~ 115 counts s^{-1}. I extracted source and background spectra with EVSELECT. Response matrices and ancillary files were produced with the SAS tools RMFGEN and ARFGEN, respectively. Finally the spectra were binned such that each bin had a minimum signal-to-noise ratio (S/N) greater than 20.

Immediately following the timing mode observations, EPIC-pn also observed Swift J1753.5-0127 for 10 ks in burst mode, a variation of the standard timing mode which offers high

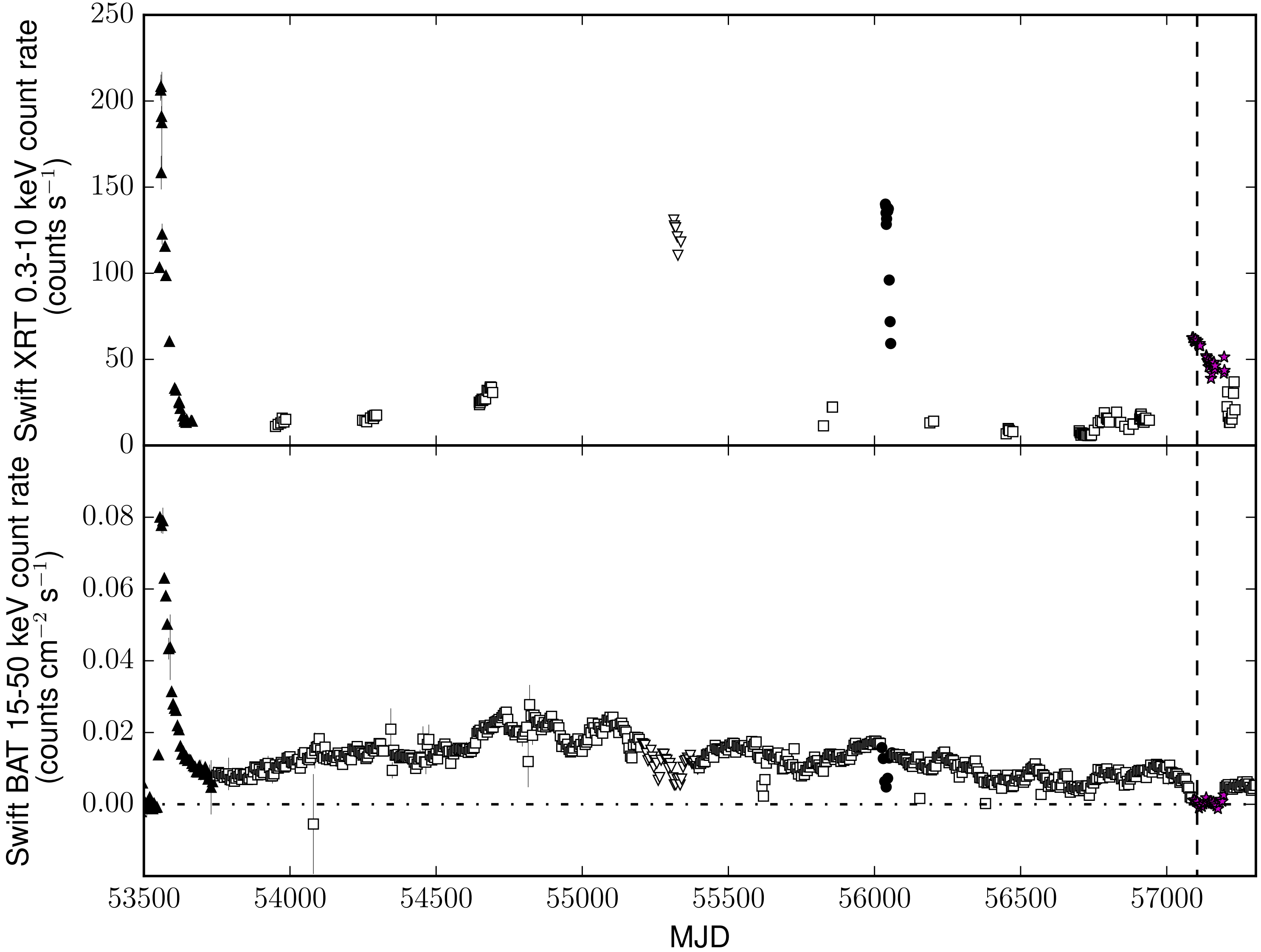

FIGURE 3.1: *Top*: Long-term light curve of Swift J1753.5-0127 using all available observations with *Swift*-XRT, grouped into 1d bins. *Bottom*: Long-term *Swift*-BAT light curve of Swift J1753.5-0127. Data are grouped into 5d bins. Black triangles represent the initial 2005 outburst and decline, open squares represent observations in the hard state, black circles and open triangles represent observations of the source during two of the failed state transitions, all as observed by *Swift*-XRT. The vertical dashed line represents *Swift*-XRT observations of the source performed between 2015 March 5 and 2015 April 2, during the time of the state transition which is the subject of this work. The dash-dotted line in the bottom panel denotes a *Swift*-BAT count rate of zero.

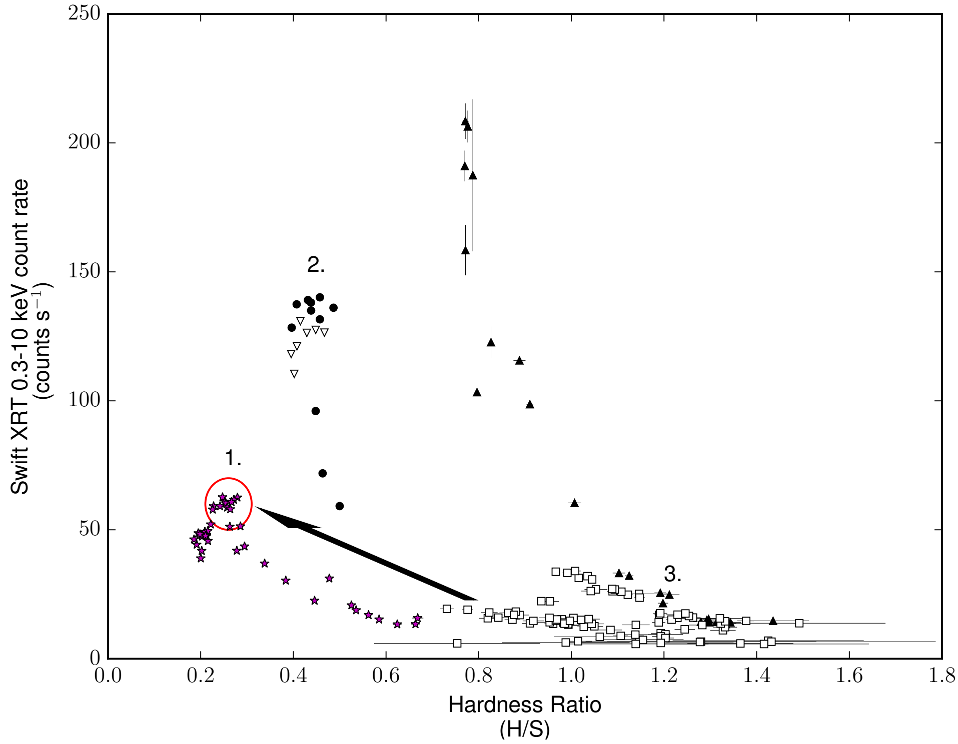

Figure 3.2: Hardness intensity diagram (HID) of Swift J1753.5-0127 using observations from *Swift*-XRT. The data are grouped into 1d bins and the symbols are the same as in Fig. 3.1. The arrow represents the direction of the state transition and the observations performed during the transition are highlighted by the red circle. The hard (H) and soft (S) bands are 1.5–10 keV and 0.3–1.5 keV, respectively. I mark the epochs used to extract the spectra presented in Fig. 3.3 as 1 (soft state), 2 (failed state transition) and 3 (hard state).

time resolution (7μs) but with a low duty cycle of 3%. Spectra were extracted in a similar way to the timing mode data, in RAWY[0:140] as suggested by Kirsch et al. (2006), and grouped into energy bins with a minimum S/N of 20. There was no pileup present in the burst mode data. The EPIC-pn covers the energy range from 0.2–10 keV, but the latest EPIC Calibration Technical Note (CAL-TN-0018[1]) recommends restricting the fit to energies greater than 0.5 keV. To be conservative, the EPIC-pn spectral fits were therefore restricted to the range 0.7–10.0 keV.

3.2.3 NuSTAR

A DDT observation of Swift J1753.5-0127 was also carried out on 2015 Mar 18 from 19:56 UTC until 2015 March 19 12:06 UTC with *NuSTAR* for a total exposure of 31ks. *NuSTAR* consists of two co-aligned grazing incidence telescopes, FPMA and FPMB,

[1]http://xmm2.esac.esa.int/docs/documents/CAL-TN-0018.pdf

TABLE 3.1: Summary of X-ray spectral observations of Swift J1753.5-0127

Obs. ID	Start Date (UTC)	MJD	Instrument	Observing Mode	Exposure Time (ks)
00031232024	2012 April 24	56041	*Swift*-XRT	WT	1.0
00030090059	2013 June 18	56461	*Swift*-XRT	WT	2.0
00030090067	2015 March 17	57098	*Swift*-XRT	WT	1.0
80001047002	2015 March 18	57099	*NuSTAR*	—	31
0770580201	2015 March 19	57100	*XMM-Newton* pn	Timing	32
0770580201	2015 March 19	57100	*XMM-Newton* pn	Burst	10

operating in the 3–78 keV energy range, offering unprecedented sensitivity in the hard X-ray band which has previously only been provided by proportional counter (non-imaging) telescopes. The data were processed with HEASOFT v6.16 and the task NUPIPELINE. A spectrum and light curve were extracted from a circular region of radius 45″. Background counts were extracted from a source-free polygonal region on the same CCD. Spectra were grouped to have a minimum of 50 counts per energy bin. The average count rates were found to be 1.46 and 1.39 counts s^{-1} in FPMA and FPMB, respectively.

3.3 Results

3.3.1 The Light Curve and Hardness-Intensity Diagram

The *Swift*-XRT light curve presented in Fig. 3.1 shows the initial 2005 fast rise and exponential decay, which corresponds to the hard state outburst of the source as well as observations of the source in the hard state, characterised by the source's low flux (0.3–10 keV count rate∼10–30 counts s^{-1}) and hard spectrum (HR > 0.8).

Also visible in the XRT light curve are two large increases in the 0.3–10 keV count rate (at MJD ∼55250 and ∼56000), reaching ∼ 60% that of the original outburst. Due to the limited coverage by *Swift*-XRT, the timescale of the first of these events is uncertain. However, the second event is simultaneous with a hard X-ray dip present in *Swift*-BAT light curves (chapter 2), which lasted for ∼ 25d. This increase in soft X-rays and simultaneous decrease in hard X-rays is characterised, spectrally, by an increase in inner disc temperature and a decrease in Comptonised emission (Yoshikawa et al., 2015). A study of the first of these spectral softenings revealed that the source had transitioned to the hard intermediate state, in which there was still significant variability (fractional rms > 13%), but a notably softer spectrum (a failed state transition; Soleri et al. 2013). The two events occupy similar regions in the HID (HR ∼0.4–0.5) and exhibit similar spectral properties such as inner disc temperature (Soleri et al., 2013; Yoshikawa et al., 2015), suggesting that they are both associated with the same phenomena. Following Soleri et al. (2013), I shall refer to these two events as the 'failed state transitions.'

At MJD ∼57100 in Fig. 3.1 I have highlighted the *Swift*-XRT observations of Swift J1753.5-0127 which took place in March 2015, during which time the *Swift*-BAT flux had been steadily decreasing (Onodera et al., 2015), visible in the lower panel of Fig. 3.1. The light curve shows a notable increase in 0.3–10 keV count rate (∼55 counts s^{-1} compared to a base rate of ∼ 10–20 counts s^{-1}). However, the flux does not reach the levels of the failed state transitions. The HR also suggests that the source is much softer than during the failed state transitions (epoch 1, Fig. 3.2). The apparent return of the source to the hard state is also seen as a gradual hardening of the source in Fig. 3.2, coincident with a decrease in 0.3–10 keV count rate and a corresponding increase in *Swift*-BAT flux (Fig. 3.1). In order to investigate the low flux of the apparent soft state a detailed study of the X-ray spectrum during the transition must be undertaken.

3.3.2 Spectral Fits: *Swift*

All spectral fits were performed using XSPEC v12.8.2 (Arnaud, 1996) which uses the χ^2 minimisation technique to determine the best fit model. The interstellar absorption is accounted for by the TBABS model with Wilms et al. (2000) abundances and photo-ionisation cross-sections described by Verner et al. (1996). I also included a systematic error of 3% for the *Swift*-XRT spectra, given the uncertainties of the response matrix (SWIFT-XRT-CALDB-09[2]). I first examined the *Swift*-XRT data in three individual spectral epochs (labelled “1,” “2” and “3”) as defined by the HID in Fig. 3.2. As discussed above, I chose one observation from each of these epochs, i.e. when the source was in the hard state, at the peak of the failed-state transition and in the apparent new spectral state. The unfolded spectra are presented in Fig. 3.3 and exhibit dramatically different spectral properties.

During the hard state, the *Swift*-XRT spectrum can be well described ($\chi^2_\nu = 0.96$) by an absorbed power law (POWERLAW) with photon index $\Gamma = 1.51 \pm 0.04$ (90% confidence errors are given here and throughout this chapter unless otherwise indicated) which is typical of a source in the hard state. During the failed state transition, I find that a one-component model such as an absorbed power law does not fit the data well ($\chi^2_\nu = 2.15$). The addition of a multi-colour disc (DISKBB) component ($kT_{\rm in} = 0.50^{+0.02}_{-0.01}$ keV) to the model provides an acceptable fit ($\chi^2_\nu = 0.89$). In this state I find a steeper power law index $\Gamma = 3.16^{+0.29}_{-0.32}$.

The March 17 *Swift*-XRT spectrum is more complicated to fit. Utilising the DISKBB + POWERLAW model, as before, I find a less acceptable fit ($\chi^2_\nu = 1.11$; $kT_{\rm in} = 0.54^{+0.04}_{-0.05}$ keV and $\Gamma = 4.32^{+0.12}_{-0.14}$) although it must be noted that the power law component in

[2]http://www.swift.ac.uk/analysis/xrt/files/SWIFT-XRT-CALDB-09_v16.pdf

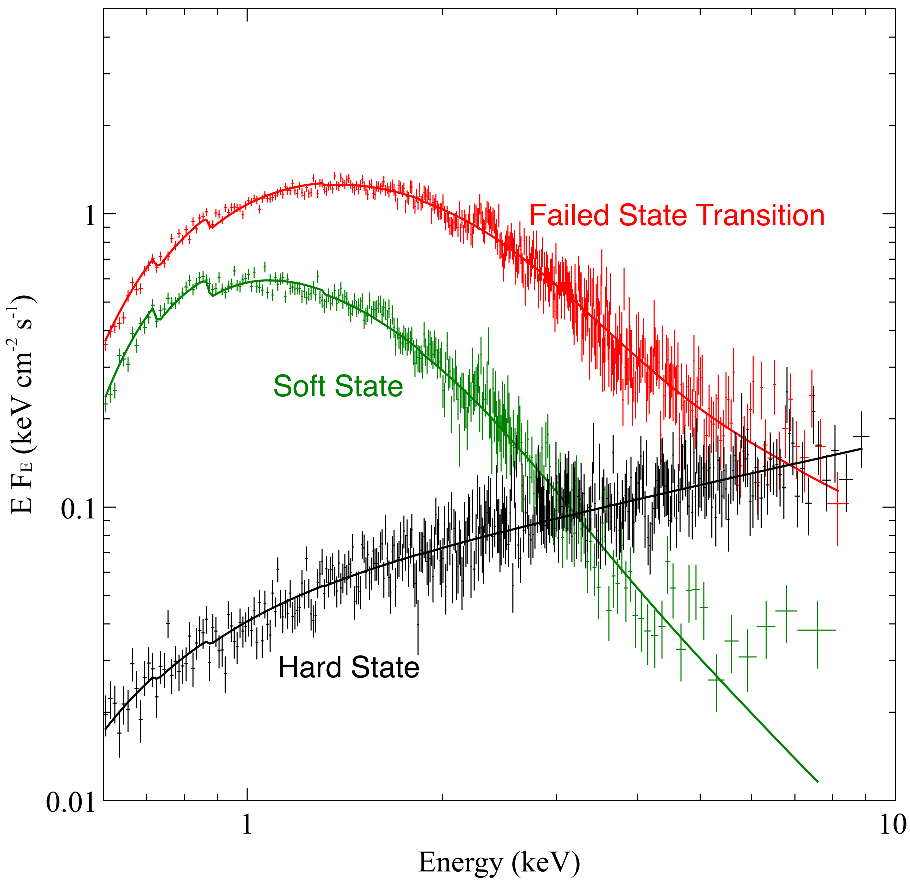

FIGURE 3.3: A comparison of unfolded *Swift*-XRT spectra from 3 epochs: during the failed state transition (2012 Apr 24; red), during the hard state (2013 June 18; black) and during the apparent new accretion state (2015 March 17; green). The 2012 and 2015 data are fitted with DISKBB+POWERLAW and the 2013 data are fitted with POWERLAW (solid lines).

this spectrum is steeper than during the failed state transition. The March 17 spectrum deviates from the model significantly at energies >5 keV, which could be indicative of an additional hard spectral component, although the S/N of the spectrum is too poor to investigate using *Swift*.

Figs. 3.2 and 3.3 show that the flux of the March 17 *Swift* spectrum appears to be lower than that of the short-lived failed state transition. For the failed state transition the absorbed flux, $F = 2.9 \times 10^{-9}$erg cm^{-2} s^{-1}, whilst for the new state $F = 1.1 \times 10^{-9}$erg cm^{-2} s^{-1} (0.6–10 keV) which corresponds to a low Eddington fraction, as discussed further in section 3.4. In order to study this apparently low-luminosity soft state, the full broadband spectrum must be investigated.

3.3.3 Spectral fits: *XMM-Newton* and *NuSTAR*

For fitting the broadband spectrum, I chose to fix the interstellar column density to $N_H = 2.0 \times 10^{21}$ cm^{-2}, obtained by fitting the Lyα absorption line in the UV spectrum (Froning et al., 2014). I also included a systematic error of 1.2% and 1% in the 2–3 and 3–5 keV bands, respectively, to account for uncertainties in the response matrices (see e.g. Díaz Trigo et al. 2014). Upon investigation of the broadband spectrum, I find that the burst mode spectrum is consistent with the March 17 *Swift*-XRT spectrum below 2 keV, although the timing mode data does not agree with the burst mode data. I therefore utilise the burst mode spectra across the entire energy range (0.7–10 keV), and the timing mode data only at energies > 2 keV. I also include the *NuSTAR* observations. The cross-normalisation between *XMM-Newton* and *NuSTAR* was allowed to vary with the fit, however it remained close to unity independent of the chosen model. Table 3.2 shows the results of the fits of a number of models to the data. The residuals of the model fits are presented in Fig. 3.4.

3.3.3.1 Disk blackbody plus power law

I first consider the DISKBB + POWERLAW model, in order to draw comparisons with previous studies of the source in different accretion states (Wilkinson & Uttley, 2009; Yoshikawa et al., 2015; Tomsick et al., 2015). Those studies have shown that the source in both the hard state and the failed state transition is well constrained by such a model, as is also noted above with the *Swift* spectral fits. As suggested by fitting the same model to the *Swift* spectrum (see above), such a simple model cannot accurately represent the 0.7–78 keV spectrum ($\chi^2_\nu = 3.02$; see Table 3.2 and Fig. 3.4a). Replacing the power law with an empirical Comptonisation model (e.g. NTHCOMP; Życki et al. 1999) did not improve the fit ($\chi^2_\nu = 3.19$). I note that there is evidence for a slight deviation from the power law component above ~ 20 keV, which could be evidence of a weak reflection component, despite the fact that the residuals do not show evidence for a strong Fe emission line at 6.4 keV as might be expected if there was reflection. Adding a reflection component to the power law with the REFLIONX model (Ross & Fabian, 2005) does improve the fit ($\chi^2_\nu = 2.08$; Table 3.2), and appears to correct the residuals above 20 keV (Fig. 3.4b), however, the fit is still not acceptable.

3.3.3.2 Compton-upscattered disc blackbody

Due to the increase in the soft component of the spectrum, I utilised the SIMple Power Law model (SIMPL; Steiner et al. 2009), a characterisation of Comptonization in which

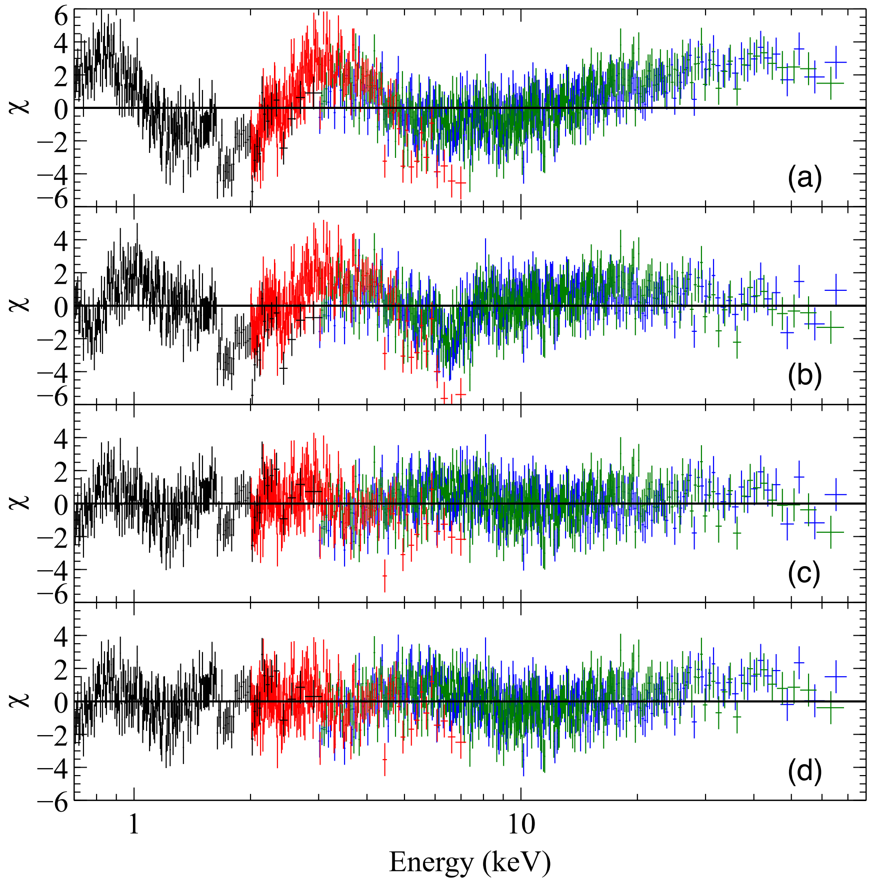

FIGURE 3.4: $\Delta\chi$ residuals of the best fit model to the combined *XMM-Newton* and *NuSTAR* spectrum of Swift J1753.5-0127. The models (defined in text) are: (a) DISKBB+POWERLAW, (b) DISKBB+POWERLAW+REFLIONX, (c) (SIMPL*DISKBB)+POWERLAW and (d) DISKIR. The figure utilised data from *XMM-Newton*/PN in Burst Mode (black) and Timing Mode (red), *NuSTAR*/FPMA (green) and *NuSTAR*/FPMB (blue).

seed photons from an input thermal spectrum are scattered into a power law component. SIMPL is designed to be used with soft thermal spectra, which are Compton thin and exhibit a power law index $\Gamma > 1$. I utilise the model in the form DISKBB * SIMPL, but this does not describe the data well ($\chi^2_\nu = 3.08$).

As seen from the results in Table 3.2 and Fig. 3.4c the fit improves significantly ($\chi^2_\nu = 1.28$), however, if an additional power law is introduced to the model ((SIMPL * DISKBB) + POWERLAW). The broad-band unfolded spectrum fitted with this model is presented in Fig. 3.5. It is important to note that the disc photons appear to be scattered into a steep power law ($\Gamma_{\rm simpl} = 6.39^{+0.08}_{-0.02}$), plus there is an additional hard power law tail ($\Gamma_{\rm PL} = 1.79 \pm 0.02$). Whilst this models the spectrum more accurately than just a multi-colour disc plus a power law, it is not a self-consistent physical model as it is not clear how to produce such a steep power law. In order to discuss the underlying physics

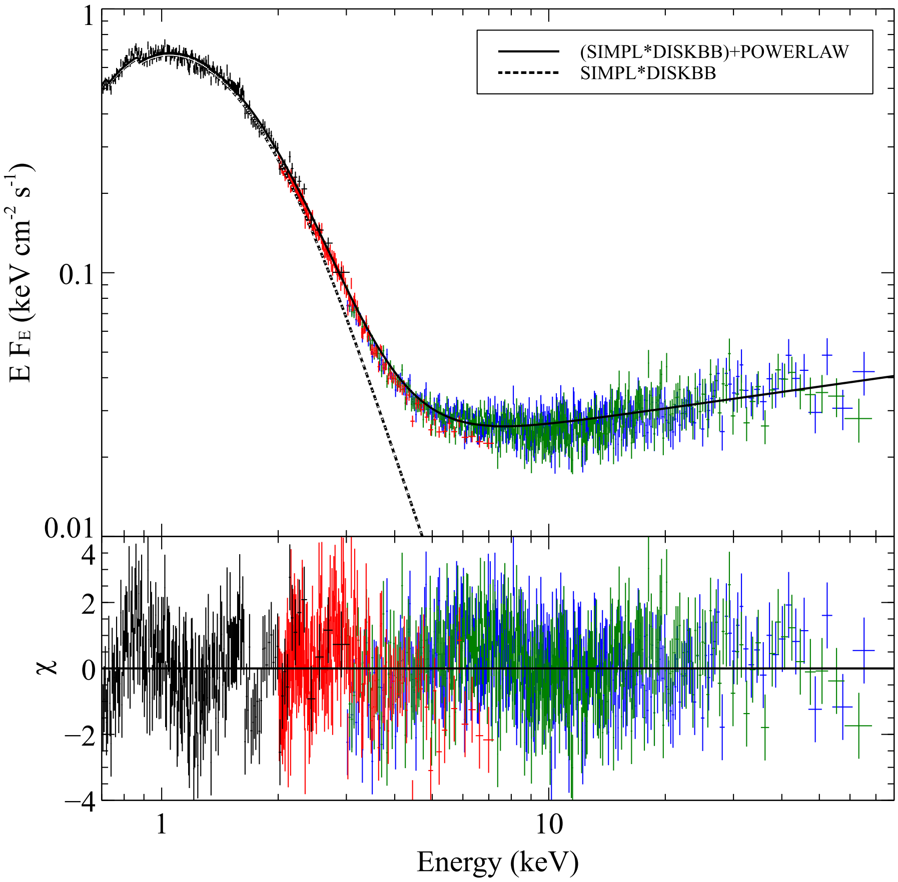

FIGURE 3.5: The combined *XMM-Newton* and *NuSTAR* spectrum of Swift J1753.5-0127. The 0.7–78 keV spectrum is unfolded and has been fitted with a Compton up-scattered disc model with an additional power law, illustrated by the solid black line. The dotted line represents the SIMPL*DISKBB model fit, without the additional power law. The colour scheme is the same as in Fig. 3.4.

of the soft state of Swift J1753.5-0127, the additional soft component – parametrised here by the additional soft, steep power law – must be modelled.

DISKBB is a simple model which equates the disc as a sum of multiple blackbody spectra (Mitsuda et al., 1984) and does not take into account vertical disc structure or relativistic effects. It is possible that these effects may help to explain the excess in the soft component at higher energies which is currently modelled with a steep power law. Relativistic effects can be considered with the KERRBB model, which incorporates a general relativistic disc around a Kerr BH (Li et al., 2005). I find that replacing DISKBB with the KERRBB model significantly improves the fit ($\chi^2_\nu = 2.24$) from the two component case (DISKBB + POWERLAW), however it is still not a formally acceptable fit. I find similar results when introducing the BHSPEC model (Davis & Hubeny, 2006), which self-consistently calculates the vertical structure of the disc using stellar atmosphere-like calculations of disc annuli. Utilising the model in the form BHSPEC + POWERLAW does not describe the broadband spectrum well ($\chi^2_\nu = 2.96$).

In either of these more physical models, the observed additional soft component in the spectrum cannot be accurately reproduced. Therefore, I continue to describe the spectral shape at lower energies using the simpler DISKBB model, upscattered into a steep power law component (SIMPL).

3.3.3.3 Irradiated inner disc

During the decline of the original outburst of Swift J1753.5-0127, Chiang et al. (2010) found that the soft region of the X-ray spectrum could not be entirely described by a multi-colour disc due to an additional soft X-ray component emerging. In the new state, this additional soft component can be illustrated with a phenomenological DISKBB + BBODY + POWERLAW model. In this scenario, I find an improved fit ($\chi^2_\nu = 1.33$) over two component models, which is characterised by a multi-temperature disc (k$T_{\rm in} = 0.29 \pm 0.01$ keV) with an additional single temperature blackbody (k$T = 0.43 \pm 0.01$ keV) and a hard power law tail ($\Gamma = 1.90 \pm 0.02$).

Following Chiang et al. (2010), in which the additional soft X-ray component that emerged was well constrained by irradiation of the inner disc by the Compton tail (Gierliński et al., 2008), I apply the irradiated disc model (DISKIR) to the 0.7–78 keV spectrum of Swift J1753.5-0127 in its new state. In addition to the irradiated inner disc, DISKIR also models the illuminated outer disc, which dominates the optical and UV bands (Gierliński et al., 2009). However, as I have not included optical data here, I have fixed the fraction of the flux thermalised in the outer disc, $f_{\rm out}$, to zero. As the spectrum only extends to 78 keV, I fix the high energy cutoff (the electron temperature) $kT_e = 1000$ keV, due to the fit being insensitive to this parameter as well.

The resulting fitted parameters are displayed in Table 3.2 and show that the fit is significantly improved ($\chi^2_\nu = 1.34$) compared to two component models, and from Fig. 3.4 it is evident that the structure previously visible in simpler fits has been reduced. This is due to the model taking into account illumination of the disc by the Compton tail, which is reprocessed and re-emitted as a quasi-thermal addition to the observed disc emission (Gierliński et al., 2008). In the case of Swift J1753.5-0127 I find that the fraction of the Compton tail which is thermalised in this manner is $f_{in} = 0.72^{+0.03}_{-0.02}$ and that the ratio of luminosity in the Compton tail to that of the unilluminated disc is $\frac{L_c}{L_d} = 7.45^{+0.11}_{-0.10} \times 10^{-2}$. I also find that the radius of the Compton illuminated region of the disc is $R_{\rm irr} = 1.015 \pm 0.003 R_{\rm in}$, suggesting that according to the model only the innermost regions of the disc are being irradiated.

However, it is recommended (Gierliński et al., 2008, 2009) to freeze f_{in} to a low value. This is because the value of f_{in} also relies heavily on assumptions about the reflection albedo of the disc ($f_{in} \sim 0.1$ for typical disc albedo of 0.3; Gierliński et al. 2009). For $f_{in} = 0.74$, even if the albedo is only 0.1–0.2 it would be inferred that $\sim 80-90\%$ of the sky as seen from the corona is covered by the disc. With such a heavily illuminated disc, one would expect to see strong reflection features in the spectrum. However, despite finding an improved fit if a reflection component is added (REFLIONX; $\chi^2_\nu = 1.23$), there is no strong evidence for reflection in the form of an iron line, nor a Compton hump, as discussed previously. The observed spectrum also shows a weak power law relative to the soft disc emission ($\frac{L_c}{L_d} \sim 7\%$), so it seems unlikely that this would provide enough irradiating power to produce such a strong illuminated component. I therefore consider the DISKIR model to be an unphysical representation of the spectrum.

3.3.3.4 Investigation of reflection

Reflection of hard X-ray photons by the accretion disc is often seen as a combination of a fluorescent iron line at 6.4 keV (Fabian et al., 1989) and a broad 'Compton hump' which peaks at $\sim$ 30 keV (Lightman & White, 1988; George & Fabian, 1991). These features are seen in a number of LMXBs in both the hard and soft states (see e.g. Tomsick et al. 2014a; Fürst et al. 2015). However, in Swift J1753.5-0127 there has been no strong evidence of a reflection component in the X-ray spectrum (Tomsick et al., 2015), although a broad Fe line has been detected in hard state observations of the source (Hiemstra et al., 2009).

I have already discussed the REFLIONX model, which self-consistently includes a narrow Fe line. However in order to examine the presence of an Fe line in detail, I separately include a Gaussian at 6.4 keV in the Compton-upscattered disc blackbody model. I find the 90% upper limit on the equivalent width of a narrow ($\sigma = 0.1$ keV) line at 6.4 keV to be < 40 eV. However, the fit improves ($\Delta\chi^2 = 54$ for 3 fewer dof) if a broad line is included. The line has a central energy of $E = 6.39^{+0.36}_{-0.23}$ keV, equivalent width $EW = 0.40^{+0.25}_{-0.17}$ keV and an extremely broad width ($\sigma = 1.49^{+0.25}_{-0.30}$ keV). The high apparent EW should be associated with a significant reflection Compton hump, however, from the residuals of the (SIMPL * DISKBB) + POWERLAW model in Figs. 3.4 and 3.5, this feature is not evident. It is possible that the addition of a Gaussian is attempting to account for the unusual continuum shape and upturn in the spectrum at $\sim 4-5$ keV with an extremely broad line at ~ 6.4 keV.

However, a broad Fe line may be the result of relativistic broadening. To test this, I use a relativistic convolution of reflection in the model by replacing the hard power law component with the RELXILL model (García et al., 2014; Dauser et al., 2014), which applies relativistic smearing to the complete spectrum. Implementing RELXILL provides a formally acceptable fit ($\chi^2_\nu = 1.24$), but closer inspection of the parameters reveals that the model is perhaps over-fitting the continuum in the region of the Fe line, where there is an upturn in the spectrum (see e.g. the (SIMPL * DISKBB) + POWERLAW fit in Fig. 3.5). I find that the quality of the RELXILL fit is insensitive to a number of important parameters, most notably the BH spin parameter. Another key parameter in the fit is the Fe abundance, which prefers a maximum value of Fe/solar = 10. Forcing Fe/solar $\leq$ 1 does not improve the fit (compared to Fe/solar = 10). It is possible that RELXILL is also attempting to constrain the unusual continuum shape as discussed previously in the context of a broad Gaussian, hence the unphysical Fe abundance in this scenario. There is also no significant evidence for a Compton hump when applying RELXILL to the spectrum and I find a reflection fraction of $0.15^{+0.23}_{-0.07}$.

3.4 Discussion

3.4.1 An unusual soft state

I have presented quasi-simultaneous *XMM-Newton* and *NuSTAR* spectra from the BHC Swift J1753.5-0127 in an accretion state it has never previously been observed in. Best-fit spectral models prefer a multi-colour disc component with a hard Compton tail, with an additional steep ($\Gamma = 6.38^{+0.08}_{-0.02}$) power law component which I attempt to reconcile with an irradiated disc model but find that the parameters are unphysical. There is no strong evidence for an Fe emission line in the spectrum at 6.4 keV, nor a reflective Compton hump (if the two power law model is used). Simple, two component models (e.g. DISKBB + POWERLAW) did not provide an acceptable fit to the 0.7–78 keV spectrum, and it is evident that in this particular low, soft accretion state, Swift J1753.5-0127 does not exhibit a classical soft state spectrum. Alhough it is not clear how such a steep power law component is produced, physically, this phenomenon is not unique to Swift J1753.5-0127. The BHXRT GRO J1655-40 exhibited an unusual 'hypersoft' state during its 2005 outburst in which the photon index was measured to be $\Gamma \simeq 6$ (Uttley & Klein-Wolt, 2015). Though the inner disc temperature is much higher (k$T_{\rm in} \simeq 1.2$ keV) and the fraction of up-scattered photons much lower ($f_{\rm SC} \simeq 0.2$) for the hypersoft state of GRO J1655-40 than the soft state of Swift J1753.5-0127, it nevertheless proves that a steep power law is possible in such sources.

The spectrum does, however, show many of the classic characteristics of a LMXB in the soft state – most significantly the emergence of a disc component in the X-ray spectrum and drop in hard X-ray flux. Separately, the rms variability is found to have decreased significantly (Uttley et al., in prep) combined with a sudden drop in the radio flux

TABLE 3.2: Spectral parameters for the combined *XMM-Newton*/*NuSTAR* fits to Swift J1753.5-0127

Parameter	Units	DISKBB + POWERLAW[a]	DISKBB + POWERLAW + REFLIONX[a,b]	(SIMPL * DISKBB) + POWERLAW)	DISKIR	DISKIR + REFLIONX[b]
N_H	10^{21}cm^{-2}	2.0^c	2.0^c	2.0^c	2.0^c	2.0^c
k$T_{\rm in}$	keV	~ 0.346	~ 0.363	0.252 ± 0.003	0.297 ± 0.001	$0.302^{+0.002}_{-0.001}$
$N_{\rm disc}$	10^3	~ 9.55	~ 6.85	$32.8^{+1.6}_{-1.1}$	$20.0^{+0.1}_{-0.2}$	$17.9^{+0.2}_{-0.3}$
$\Gamma_{\rm PL}$	—	~ 2.16	—	1.79 ± 0.02	1.89 ± 0.01	—
$N_{\rm PL}$	—	~ 0.042	~ 0.044	0.017 ± 0.001	—	—
Fe/solar	—	—	~ 20.0	—	—	$12.1^{+2.5}_{-1.5}$
$\Gamma_{\rm ref}$	—	—	~ 2.23	—	—	1.98 ± 0.01
ξ	erg cm s^{-1}	—	~ 199	—	—	200^{+1}_{-6}
$N_{\rm ref}$	10^{-6}	—	~ 9.60	—	—	$2.19^{+0.25}_{-0.18}$
$\Gamma_{\rm simpl}$	—	—	—	$6.39^{+0.08}_{-0.02}$	—	—
$f_{\rm SC}$	—	—	—	1.00^d	—	—
$\frac{L_c}{Ld}$	10^{-2}	—	—	—	$7.45^{+0.11}_{-0.10}$	$6.57^{+0.14}_{-0.13}$
f_{in}	—	—	—	—	$0.72^{+0.03}_{-0.02}$	$0.79^{+0.01}_{-0.03}$
$R_{\rm irr}$	$R_{\rm in}$	—	—	—	1.015 ± 0.003	1.016 ± 0.001
χ^2_ν	—	3132/1037	2149/1034	1323/1035	1391/1035	1266/1032

[a]Due to a poor fit ($\chi^2_\nu > 2$), accurate (90% confidence) uncertainties cannot be calculated.
[b]A relativistic interpretation of reflection is discussed in Section 3.3.4.
[c]Fixed.
[d]Fraction of disc photons up scattered reached the upper limit allowable in XSPEC.

(see Chapter 4), suggesting that the compact jet has switched off - also evidence of a transition to a disc-dominated soft state. The HID constructed from ∼10 years of *Swift*-XRT observations shows that the source has indeed reached its softest state ever observed, with the HR dropping to ∼0.2–0.3, compared with ∼0.4 during the failed state transitions studied by Soleri et al. (2013) and Yoshikawa et al. (2015).

To investigate the broadband luminosity of the soft state of Swift J1753.5-0127, I calculate the unabsorbed flux (0.1–100 keV) to be 3.45×10^{-9} erg cm^{-2} s^{-1} using the XSPEC model CFLUX. It must be noted that this calculation is highly sensitive to N_H and is thus only an estimate, due to the uncertainty of the spectral shape outside the 0.7–78 keV range of the observed spectrum. Nevertheless, the chosen energy range is most representative of that required to calculate the intrinsic luminosity of the source. The distance, d to the source is not known and there are a wide range of estimates (Cadolle Bel et al., 2007; Zurita et al., 2008; Froning et al., 2014). I adopt here the upper limits of d=3.5–4.6 kpc (assuming a $7M_{\odot}$ BH and binary inclination $i < 55°$; see Chapter 5 for an estimate of the BH mass) calculated by Froning et al. (2014) from fitting accretion disc models to the UV spectrum of the source. Assuming a fiducial value of d=4 kpc I therefore estimate the luminosity to be 6.6×10^{36}erg s^{-1}, which, for a $7M_{\odot}$ BH is 0.72% of the Eddington limit. For larger BH masses, this value decreases. Soft-to-hard state transitions have been seen to occur in LMXBs mostly at luminosities between 0.3% and 3% Eddington (Maccarone, 2003; Kalemci et al., 2013), though very rarely at the lower end of this range. Swift J1753.5-0127 has therefore likely been observed to be in one of the lowest luminosity soft states recorded in BH systems, comparable to those observed in 4U 1630-47 (Tomsick et al., 2014b) and the microquasar XTE J1720-318 (Kalemci et al., 2013, see section 3.1).

However, to draw real comparisons with the aforementioned sources, the luminosity must be estimated from the same energy range. For 4U 1630-47, an Eddington fraction was calculated from the 0.5–200 keV luminosity to be $L/L_{\rm Edd} = 0.03M_{10}^{-1}\%$ where M_{10} is the mass of the BH in units of 10 $M_{\odot}$ (Tomsick et al., 2014b). I estimate the unabsorbed luminosity of Swift J1753.5-0127 (2–10 keV) to be $L = 4.2 \times 10^{36}$ erg s^{-1} or $L/L_{\rm Edd} = 0.46\%$. This is an order of magnitude higher than 4U 1630-47, although it is still a very low transition luminosity. In the case of XTE J1720-318, Kalemci et al. (2013) utilised the 3–200 keV flux to estimate an Eddington fraction of $L/L_{\rm Edd} = 0.30\%$ during the soft state. However, this is an underestimate of the Eddington fraction due to not accounting for the softest X-rays in the luminosity calculation (a product of utilising observations only from *RXTE*). I estimate $L/L_{\rm Edd} = 0.05\%$ for Swift J1753.5-0127 in this range. This is an order of magnitude lower than XTE J1720-318. Therefore, the Eddington fraction of the soft state in Swift J1753.5-0127 is actually lower than for XTE

J1720-318, making Swift J1753.5-0127 the second lowest luminosity soft state source in terms of Eddington fraction.

So far there have been several reported cases of unusual soft spectral states at very low luminosities in different sources, of which Swift J1753.5-0127 is now the best-studied example. Although all these states show soft spectra, they are not like standard disc blackbodies, instead showing very steep but power law-like tails. This suggests the possibility that at such low luminosities the disc can persist but its spectrum is modified by strong Compton scattering by plasma with a temperature not much higher than the disc itself, i.e. there is a significant disc 'atmosphere.' This in turn may suggest that discs at such low accretion rates are at the borderline of evaporating, perhaps to form the standard hard state corona (e.g. via the mechanisms described by Liu et al. 2006; Meyer et al. 2007; Meyer-Hofmeister et al. 2012), yet somehow they are able to remain relatively stable at low luminosities in this borderline disc/corona state, compared to discs following the usual soft-hard transition.

3.4.2 The inner disc radius

The fitting parameters from the (SIMPL * DISKBB) + POWERLAW model can also be used to estimate the inner radius $R_{\rm in}$ of the accretion disc of Swift J1753.5-0127. The model normalisation $N_{\rm disc}$ is related to the inner radius as follows:

$$R_{\rm in}/R_g = \left(0.676 d_{10} f^2 \sqrt{N_{\rm disc}}\right) / \left((M_{BH}/M_\odot)\sqrt{\cos i}\right) \tag{3.1}$$

where f is the spectral hardening factor (see Shimura & Takahara 1995 and Equation 1 of Tomsick et al. 2015) and d_{10} is the distance to the source in units of 10 kpc. For a distance of 4 kpc, $i = 55°$ (calculated from X-ray spectral analysis of the source in the hard state; Reis et al. 2009), $M_{BH}/M_\odot = 7$ and $f = 1.7$ (a typical value; Shimura & Takahara 1995), I find $R_{\rm in} \approx 35 R_g$, though this decreases with increasing M_{BH} and increases for larger distances. Previous studies of the source in the hard state find a heavily truncated disc with $R_{\rm in} > 212 R_g$ (Tomsick et al., 2015). It is important to note that Tomsick et al. (2015) used a lower inclination ($i = 40°$), utilising this value in this calculation of $R_{\rm in}$ would only decrease the value by $\sim 4R_g$.

$R_{\rm in}$ can be estimated separately by considering the friction free boundary condition (Kubota et al., 1998). From this condition, the inner radius can be calculated as follows:

$$R_{\rm in} = \sqrt{\frac{3}{7}}\left(\frac{6}{7}\right)^3 f^2 \frac{\sqrt{N_{\rm disc}} d_{10}}{\sqrt{\cos i}} \tag{3.2}$$

Using the same values as above, I estimate $R_{\rm in} = 114$km, which for a $7M_{\odot}$ BH is $\sim 11R_g$. Regardless of the boundary condition chosen, in the soft state of Swift J1753.5-0127 the inner edge of the disc appears to have moved closer to the BH. In the case of this source, it has not entered a typical soft state, in which the mass accretion rate will reach large Eddington values ($\gtrsim 0.1$), consistent with the disc having not yet reached the innermost stable circular orbit (ISCO). However, $R_{\rm in}$ is significantly closer to the BH than that in the hard state.

It is interesting to compare my calculated value of $R_{\rm in}$ with that of Yoshikawa et al. (2015). I find $N_{\rm disc}$ to be an order of magnitude larger in the soft state than Yoshikawa et al. (2015) find during one of the failed state transitions. This implies that the disc was closer to the BH ($R_{\rm in} \sim 4R_g$ for identical parameters as above) during the short-lived intermediate state, which correlates with the higher disc temperature seen at this time.

3.5 Conclusions

The LMXB Swift J1753.5-0127 transitioned to a low luminosity soft state in March 2015, previously unseen in this source, after ∼10 yrs in the hard state (which is also highly unusual amongst BHXRTs). The X-ray spectrum is dominated by a soft accretion disc component and a hard power law tail, although I find that a simple two component model does not constrain the data well and a third component is required. The best fit model describes the spectrum with a multi-temperature disc with k$T_{\rm in} = 0.252$ keV which is scattered into a steep power law ($\Gamma = 6.39$), plus an additional, hard ($\Gamma = 1.79$) power law tail. I discuss the possibility that the softer, steep power law component could be caused by the irradiation of the inner disc by the Compton tail, but I find that the parameters are unphysical and the fit can be equally well replicated by including an additional multi-temperature disc component in place of the irradiated disc. I find that there is no evidence for Fe emission at 6.4 keV (a 90% confidence upper limit equivalent width of < 40 eV), nor for a reflection component in the best fit model.

Chapter 4

Disc-Jet quenching of the Galactic black hole Swift J1753.5-0127

"It is thanks to very long baseline interferometry that we can offer the highest precision horoscopes in all of astrology."

@RadioAstrology

In this chapter I continue my study of the low-luminosity soft state of Swift J1753.5-0127. After the success of our combined *XMM-Newton* and *NuSTAR* observations of the source, collaborators and I requested and obtained a deep radio observation during the soft state. The radio flux was found to be $< 21\ \mu$Jy, indicating that the jet was quenched by a factor $\gtrsim 25$, despite the low luminosity nature of the soft state. Here I present this deep radio observation alongside regular radio and X-ray monitoring observations of Swift J1753.5-0127, showing the connection of the radio-jet quenching to the X-ray power law component.

In this chapter, sentences using active voice describe the work I have done, whereas sentences using passive voice describe work undertaken by my collaborator Anthony Rushton.

4.1 Introduction

The spectral evolution of SXTs as they progress through an outburst occurs on observable timescales, presenting the ideal opportunity to study the disc-jet relationship with vastly different accretion rates and disc topologies (see e.g. section 1.3.3, Fender, 2010; Gallo, 2015).

XRBs have a well-established, albeit complex phenomenological relationship between the state of the accretion disc and the jet luminosity. To first-order approximation there appears to be a correlation with the hard X-rays and the compact jet. Fender et al. (2004) showed that as XRBs trace a hysteresis loop around the HID, they display distinctly different modes of jet activity; hard states are associated with compact jets, soft states with jet suppression and transitions from hard to soft states can eject knots of discrete plasma (see also sections 1.3.3 and 1.3.3.1). Intermediate states, such as those seen in Cygnus X-1 (Rushton et al., 2012), have also shown a reduction in the jet luminosity and size (although not a complete quenching). Furthermore, within the hard-state it has been shown that a non-linear relationship exists between the luminosity of the jet and the accretion disc. For example, Corbel et al. (2003) initially showed that for the BHXRT GX 339-4 the radio emission scales with the X-rays with a power law index of $\zeta \sim 0.7$ (for a flux relation $f_{\mathrm{X}} \propto f_{\mathrm{rad}}^{\zeta}$). Then, by accounting for distance, it was shown that a sample of BHXRTs follows a similar luminosity relationship (e.g. Gallo et al., 2003, 2006). Moreover, it has been suggested this relationship is a “fundamental-plane” for black holes of all mass taking the form $\log L_r = (0.6 \pm 0.1) \log L_x + (0.8 \pm 0.1) \log M + (7.3 \pm 4.1)$ (Merloni et al., 2003).

Swift J1753.5-0127 transitioned to the soft state in March 2015 (chapter 3) at an unusually low luminosity ($< 1\%\ L_{\mathrm{Edd}}$). In this chapter I present analysis of all the radio monitoring observations of this source since its initial discovery and report on deep limits on the radio activity in the soft state. I then discuss the implications this unusual source has for the X-ray/radio correlation.

4.2 Observations and Data Reduction

4.2.1 Archival radio observations (2005–2009)

Following the initial discovery of Swift J1753.5-0127 in 2005 an intensive series of radio observations was reported by Soleri et al. (2010). Their work analysed a sub-set of observations that were coincidental with *Swift* and *RXTE*. This analysis makes use of the full set of radio fluxes which they reported in table A2, including the Very Large Array (VLA) at 1.4, 4.8 and 8.4 GHz, the Multi-Element Radio-Linked Interferometer Network (MERLIN) at 1.7 GHz and the Westerbork Synthesis Radio Telescope (WSRT) 4.9 and 8.5 GHz. The initial observations caught a radio flare that peaked up to ~ 3 mJy and decayed over a period of about 100 days, until steadying at a mean flux of ~ 0.4 mJy.

The radio spectrum between 1.4 and 8.4 GHz showed a mostly flat or slightly inverted spectrum, indicative of a self-absorbed synchrotron jet of energetic particles (section 1.3.3). The overall radio flare, decay and steady emission closely couple with the fluxes seen in the X-ray band.

4.2.2 AMI-LA monitoring (2013–2015)

Between January 2013 and July 2015 the Arcminute Microkelvin Imager Large Array (AMI-LA) aperiodically monitored Swift J1753.5-0127, with a typical cadence of 1–2 weeks. Each epoch lasted a few hours and was scheduled around the source's local transit of the telescope. The array consists of eight 12.8 m dishes with baselines ranging from 18 to 110 m located in Cambridge, UK and was built by the Mullard Radio Astronomy Observatory (AMI Consortium: Zwart et al., 2008). During this period AMI-LA operated at a frequency range of 13.9–17.5 GHz, with the analogue XF correlator providing five usable channels each with a bandpass of 0.72 GHz giving a total bandwidth of 3.6 GHz.

Data calibration was performed using the PYTHON DRIVE-AMI pipeline (Staley & Anderson, 2015a,b)[1], which uses the MRAO tool REDUCE to automatically flag for interference, shadowing and hardware errors, conduct phase and amplitude calibrations, and Fourier transforms the data into *uv*-FITS format (see Perrott et al., 2013). Imaging was performed within the Common Astronomy Software Application (CASA; McMullin et al., 2007) produced by NRAO, using the CLEAN task driven by the DRIVE-AMI wrapper. The resultant maps were then loaded and analysed by the Transient Pipeline (TraP: Swinbank et al., 2015) in order to extract the flux density of each epoch.

4.2.3 JVLA observation (May 2015)

Swift J1753.5-0127 was observed with the Karl G. Jansky Very Large Array (JVLA) on 2015 May 13 07:32–09:15 UT (project code 15A-481), with a total on-source time of 84 minutes. The array was mostly in the "B" configuration with baselines of up to 11.1 km (a single antenna had been moved to "A" configuration). The wide X-band receiver system was used with 3-bit samplers, allowing a tuneable frequency range of 7.7–12.6 GHz. Due to radio-frequency interference (RFI; sources of radio emission other than Swift J1753.5-0127, e.g. radio transmitters) within the band, the basebands were tuned to cover 7.98–11.67 GHz giving a total usable bandwidth of 3.69 GHz. Observations were made at a central frequency of 9.8 GHz using two basebands each divided into 16 sub-bands with 64 x 2 MHz channels per sub-band.

[1] `https://github.com/timstaley/drive-ami`

Data reduction was carried out using CASA. Initial inspection of the data was performed to flag bad data from antenna errors, shadowing, RFI, or other instrumental issues. Hanning smoothing was applied to minimise the effects of RFI on surrounding frequency channels. Bandpass and flux scale calibration was performed using a short observation of 3C 286. The flux density scale was set using Perley & Butler (2013) and transferred to the phase calibrator and target field. Time-dependent amplitude and phase gains were solved using the nearby phase calibrator J1743-0350 using a 2:8 minute duty cycle between calibrator and target.

No significant radio flux is detected within the primary beam. The mean rms noise towards the phase centre is 7 μJy bm^{-1}, making the 3σ upper limit of the flux from this epoch < 21 μJy.

4.2.4 *Swift* observations

I utilised 175 observations of Swift J1753.5-0127 made with the *Swift* Gamma-ray Burst Mission (Gehrels et al., 2004) between 2005 July 02 and 2015 July 30. For the purposes of this work I have used a number of archival XRT observations (Target IDs: 00030090, 00031232 and 00033140), and I have also monitored the 15–50 keV flux with the *Swift* BAT.

Swift-XRT operated in windowed timing (WT) mode for each of these observations, eliminating the possibility of photon pile-up on the CCD. Data were reduced using the HEASOFT v6.16 task XRTPIPELINE and count rates extracted from a circular region 20 pixels in radius ($\approx$ 47"). The background count rate was extracted from an annulus centred on the source with inner and outer radii of 80 and 120 pixels, respectively. Spectra were grouped to have a minimum of 20 counts per energy bin, allowing the use of the χ^2 statistic when fitting models to the data.

All spectral fits were performed using XSPEC v12.8.2 (Arnaud, 1996) which uses the χ^2 minimisation technique to determine the best fit model. The interstellar absorption is accounted for by the TBABS model with Wilms et al. (2000) abundances and photoionisation cross-sections described by Verner et al. (1996). Also included is a systematic error of 3% for the *Swift*-XRT spectra, given the uncertainties of the response matrix (SWIFT-XRT-CALDB-09[2]). I fitted two models to each spectrum, an absorbed power law (POWERLAW) and an absorbed disc-blackbody plus power law (DISKBB+POWERLAW), with the best-fit model determined using an F-test. Once this had been done, I extracted the unabsorbed flux with the XPSEC model CFLUX and determined the 90% confidence intervals for each fit parameter.

[2]http://www.swift.ac.uk/analysis/xrt/files/SWIFT-XRT-CALDB-09_v16.pdf

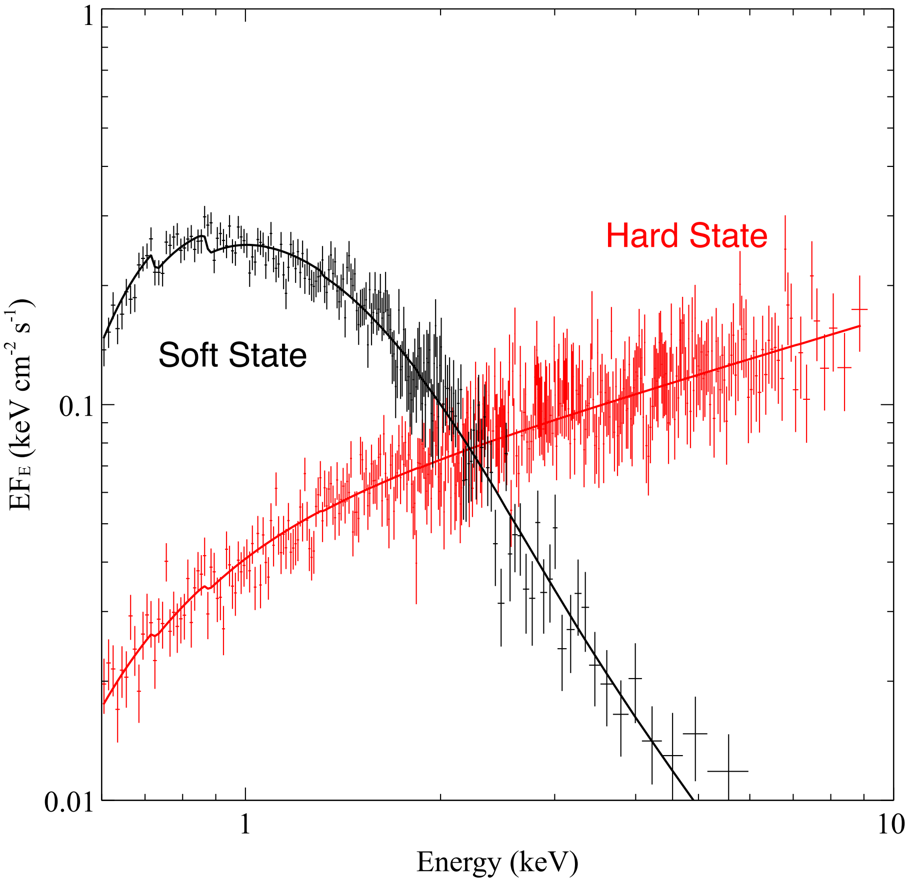

FIGURE 4.1: A comparison of unfolded *Swift*-XRT spectra from two epochs: during the 2015 soft state (2015 May 13th; black) and during a typical hard-state (2013 June 18; red). The 2015 data are fitted with DISKBB+POWERLAW and the 2013 data are fitted with POWERLAW (solid lines).

A *Swift*-XRT observation of Swift J1753.5-0127 was also performed on 2015 May 13 10:15–10:33 UT, 1 hr after the JVLA observation. The total exposure time was 1058s. The spectrum was extracted using similar methods to those described above and is well constrained with an absorbed disc-blackbody plus power law. I measure the unabsorbed X-ray flux (0.6-10 keV) to be $F = 1.09^{+0.27}_{-0.37} \times 10^{-9}$ erg cm^{-2} s^{-1} with a photon index of $\Gamma = 4.29^{+0.28}_{-0.71}$, an inner disc temperature $kT_{in} = 0.31^{+0.05}_{-0.03}$ keV and $N_H = 4.1^{+0.9}_{-1.8} \times 10^{21}$ cm^{-2} (χ^2/d.o.f. = 1.02). The soft state spectrum is shown as black in Fig. 4.1 and compared to a typical hard-state spectrum in red.

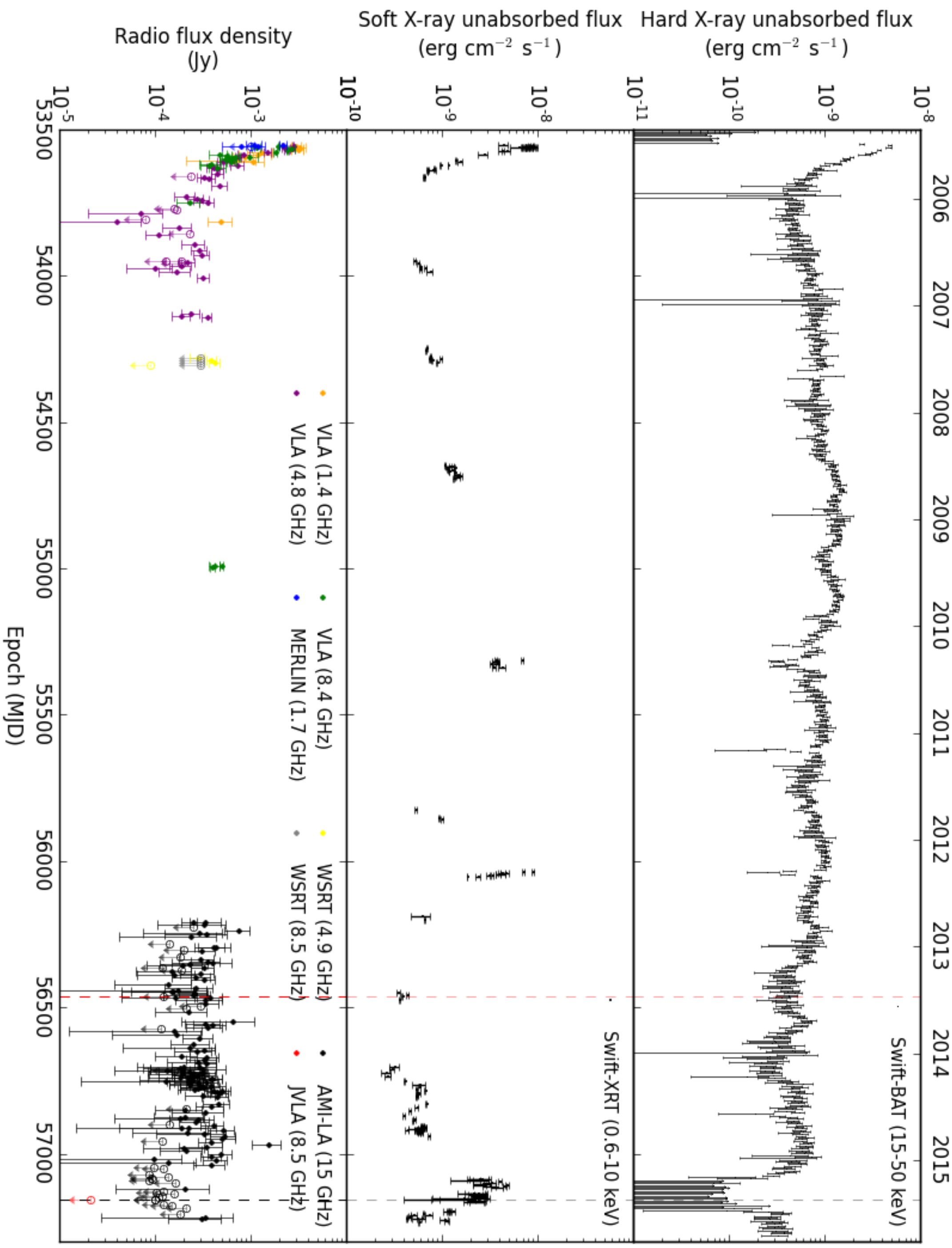

FIGURE 4.2: The 2005–2015 X-ray and radio lightcurve of Swift J1753.5-0127. The X-ray spectra at the times of the dashed lines are shown in Figure 4.1. Figure kindly provided by Anthony Rushton.

4.3 Results and Analysis

4.3.1 ~ 10 year Radio and X-ray light curve

The light curve shown in Fig. 4.2 shows the Fast Rise, Exponential Decay (FRED) outburst of 2005, with an increase in both X-ray and radio luminosity by over an order of magnitude compared to the subsequent long-term average. The X-ray emission flared to almost 10^{-8} erg cm^{-2} s^{-1} in both the 1-10 keV and 15-150 keV band with a slow decay over $\sim$ 100 days. Likewise the radio emission showed a quick rise to just over 3 mJy followed by a slow decay to around 0.4 mJy.

The 'failed state transitions' previously discussed in chapter 3 (section 3.3) are visible in Fig. 4.2 at $\sim$ 55400 and 56000 as a dramatic increase in soft flux coupled with a simultaneous decrease in hard flux. Unfortunately no radio observations were performed during these epochs.

Between 2013 and mid-2015 AMI-LA intensively monitored the source every few days. During the hard state, the flux maintain a time-averaged value of 0.3 mJy with an rms-variability (after correcting for noise) of 0.14 mJy; this behaviour was typical for the flux level post-2005 flare, assuming there was no major change to the spectral index. The source remained in this state until January 2015 when the flux suddenly quenched below the 3σ monitoring detection limit (< 150 μJy bm^{-1}). This corresponds to the soft state transition seen in X-rays (chapter 3). Swift J1753.5-0127 remained in this radio-quenched soft state for $\sim$ 170 days before returning to the hard-state in July of 2015. Two weeks later AMI-LA monitoring halted due to a scheduled correlator upgrade.

4.3.2 The X-ray / Radio Correlation of Swift J1753.5-0127

The radio and X-ray flux over the entire $\sim$ 10 yr dataset was correlated by matching epochs that are quasi-contemporaneous. A maximum separation limit of three days was used to produce a reasonably large sample that did not significantly increase χ^2 in the fits. All observations correspond to the hard or quiescent state (with the exception of the deep JVLA soft state epoch reported here, which is omitted from this analysis). The 1.7 GHz observations reported by Soleri et al. (2010) are omitted as the MERLIN measurements are inconsistent with the overall spectrum and appear unusually low, which could be due to calibration errors (reanalysis of this data is beyond the scope of this work).

The correlation was performed using data from both the soft 0.6–10 keV X-ray band measured by *Swift*-XRT and the hard 15–50 keV X-ray band measured by *Swift*-BAT.

Figure 4.3 shows the radio relationship against the hard and soft bands in the upper and lower panels respectively. The majority of the lower radio luminosity data was taken using the AMI telescope which had a typical rms noise of ~ 50 μJy bm^{-1} and most of the AMI-LA (15 GHz) points are 2–10σ. A significance cut-off of 3σ is set and an upper-limit is placed on any points below this flux. An F-test is performed by using an orthogonal distance regression analysis (using SCIPY.ODR) with a single and broken power law function to test if either model is favoured. The F-test shows that applying a broken power law was not justified and in Fig. 4.3 the power law fit (solid red line) of the form $S_{\rm radio} = k(S_{\rm X-ray})^{\zeta}$ is shown, where $\zeta = 0.99{\pm}0.12$ for the BAT and $\zeta = 0.96{\pm}0.06$ for the XRT.

Although estimating the disc-jet luminosity is dominated by uncertainty in the distance, it is clear that compared to other XRBs Swift J1753.5-0127 has remained on the radio-quiet branch (as originally shown in Soleri et al., 2010). Assuming a distance of 2.3–8 kpc the median X-ray luminosity is $(5-50)\times 10^{35}$ erg s^{-1} and is associated with a (5 GHz) radio luminosity of $(1-10)\times 10^{28}$ erg s^{-1} i.e. an $L_{\rm radio}/L_{\rm X-ray}$ ratio of $\sim 5\times 10^7$. For most XRBs that follow the "upper-branch" of the scaling relationship (i.e. scale with power law $\zeta \sim 0.7$) the corresponding radio luminosity would be $(6-30)\times 10^{29}$ erg s^{-1} i.e. a ratio of $\sim 8\times 10^5$.

In Fig. 4.4 I present the 5 GHz vs 0.6–10 keV luminosity of Swift J1753.5-0127 (assuming the upper distance of 8 kpc) compared to a sample of quiescent and hard-state XRBs taken from Corbel et al. (2013). Swift J1753.5-0127 falls on the "lower-branch" which has a cluster of 4-5 sources that are also about an order of magnitude quieter in radio emission than e.g. GX 339-4 and V404 Cyg (the "upper-branch").

4.3.3 Soft-state quenching of the radio jet

The deep JVLA radio observation of Swift J1753.5-0127 places the most stringent quenching factor on the soft state radio flux from a BHXRT. Previous works studying the radio quenching have only used the apparent XRB Radio-X-ray luminosity relationship to estimate the analogous hard-state radio flux. For example, Russell et al. (2011) have so-far placed the deepest constraints on the radio flux of a persistent soft state BH XRB; the soft state radio flux density of 4U 1957+11 was measured to be significantly less (3σ) than 11.4 μJy ($F_{5\ \rm GHz} < 5.7\times10^{-19}$ erg s^{-1} cm^{-2}) and the corresponding unabsorbed X-ray flux was measured as $F_{1-10\ \rm keV} = 8.8\times 10^{-10}$ erg s^{-1} cm^{-2}, thus making $\frac{F_{1-10\ \rm keV}}{F_{5\ \rm GHz}} > 1.5\times 10^{9}$. The *inferred* hard-state radio flux of 4U 1957+11 is between $3.7-9.2$ mJy, based on the assumption that the source traces the upper-radio branch of the Radio-X-ray luminosity relationship and has a distance of 7–22 kpc. If correct,

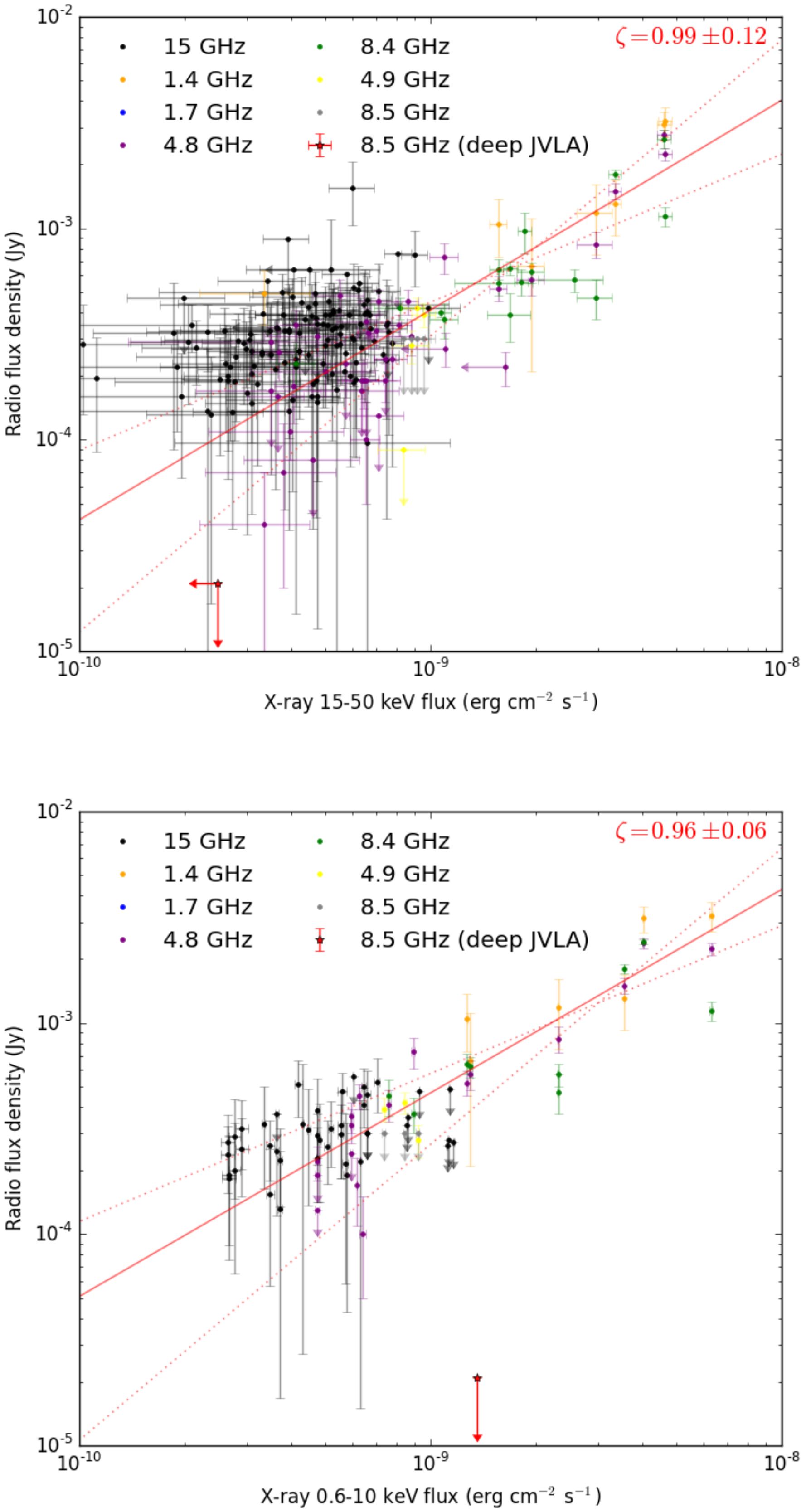

FIGURE 4.3: The X-ray / radio flux correlation. The dotted lines show a power law relationship of $\zeta = 0.7$ and 1.4 and the solid line shows the best fit. *Upper panel* shows the sample correlated with daily *Swift*-BAT data. *Lower panel* shows the radio sample correlated with measurements taken with the *Swift*-XRT. Marked in both panels is the limit of a deep JVLA observation taken in the soft state. Figure kindly provided by Anthony Rushton.

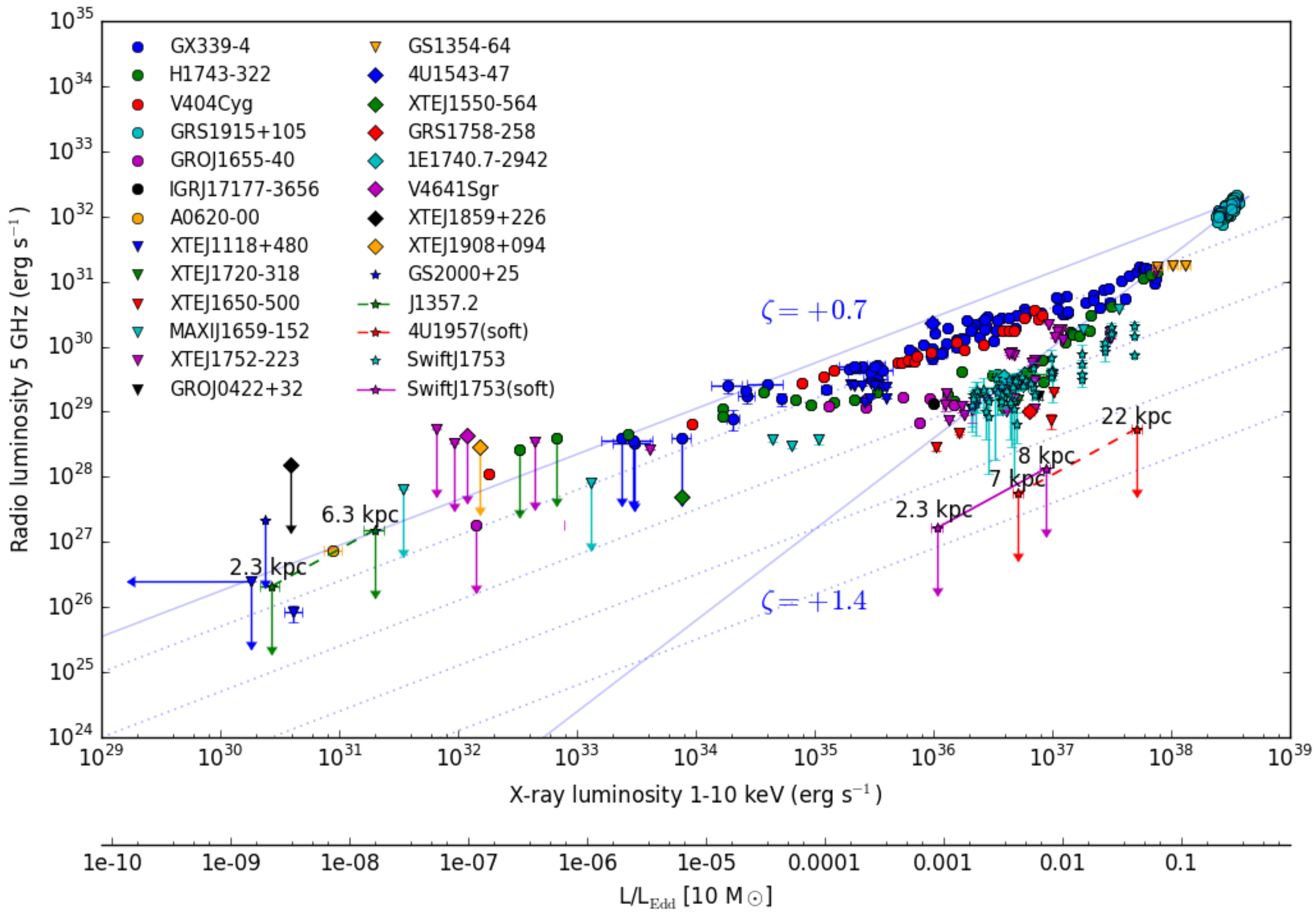

FIGURE 4.4: The X-ray/radio luminosity relationship for 25 XRBs. The solid lines show two different power law relationships scaled from the brightest known XRB GRS 1915+105. Also shown as dotted lines is the "standard" power law relationship ($\zeta = 0.7$) normalised by four different decades. For detections of Swift J1753.5-0127 a distance of 8 kpc is assumed.

the resultant radio quenching factor would be > 2.5 orders of magnitude, implying that jets in the soft state can be utterly suppressed.

In this chapter, a comparable tight constraint is placed on the soft state upper radio flux limit for a source with a *known hard-state radio flux.* Swift J1753.5-0127's soft state radio flux was found to be significantly less (3σ) than 21μJy ($F_{5\text{ GHz}} < 1.05 \times 10^{-18}$ erg s^{-1} cm^{-2}) and the unabsorbed soft X-ray flux for this epoch was $F_{1-10\text{ keV}} = 3.37 \times 10^{-10}$ erg s^{-1} cm^{-2}. Thus the soft state radio to X-ray flux ratio of $\frac{F_{1-10\text{ keV}}}{F_{5\text{ GHz}}} > 3.2 \times 10^{8}$ is within an order of magnitude to 4U 1957+11. Scaling the X-ray to radio flux (using the empirical flux relationship found in Fig. 4.3) corresponds to a hard-state flux of $F_{\text{radio}} \approx 600$ μJy (N.B. the mean hard-state flux is ~ 300 μJy). Thus a quenching factor of > 25 is directly observed.

The radio luminosity limits of Swift J1753.5-0127 and 4U 1957+11 are shown in Fig. 4.4. Given the estimated distance to the two sources the soft state quenching factor relative to the upper-branch is approximately the same (within the uncertainty of the distance). Shown as a solid blue line is the power law scaling of $\zeta = 0.7$ and 1.4 from GRS1915+105 (i.e. a 10 $M_{\odot}$ BH accreting at ~ 0.1 L/L_{Edd}). The soft state jet is shown to quench at least an order of magnitude more than the so-called "radiative-efficient" branch of GRS1915+105 (Rushton et al., 2010), if it were accreting at the ~ 0.01 L/L_{Edd} rate of Swift J1753.5-0127 and 4U 1957+11.

It is important to note that Swift J1753.5-0127 is a more 'canonical' transient XRB than 4U 1957+11 as the latter is a persistent soft X-ray emitter whilst the former a typical BHXRT that has transitioned across different X-ray states (although the soft state for Swift J1753.5-0127 is unusually low – see chapter 3). Also the radio emission from Swift J1753.5-0127 is clearly under-luminous compared to typical hard-state XRBs (see section 4.3.2) and the quenching factor with respect to the upper-branch of the empirical relationship is similar to 4U 1957+11. Moreover, the radio emission from 4U 1957+11 has never been detected, thus the typical radio flux is not yet known (assuming the source could ever produce a radio emitting jet).

4.4 Discussion and Conclusions

Although evidence of a disc-jet relationship is ubiquitous, significant scatter in the X-ray/radio relationship has been found. Some BHCs have shown a scaling relationship much closer to that proposed for radiatively efficient neutron stars (Körding et al., 2006). GRS1915+105 is known to have a much more luminous radio to X-ray ratio than other XRBs and Rushton et al. (2010) found the variability in the hard ("plateau") state to be significantly steeper, with a power law index of $\zeta = 1.7 \pm 0.3$; Swift J1753.5-0127 on the other hand is significantly radio-quiet compared to the "standard" GX 339-4 relationship. Evidence for a transition in the power law relationship (i.e. from the radio quiet to loud track) has been found for H 1743-322, which showed a possible transition from $\zeta = 0.6$ to 1.4 around a critical luminosity of about $L_X = 10^{35} - 10^{36}$ erg s^{-1} (Coriat et al., 2011). XTE J1752-23 also hinted at a transition where at lower radio/X-ray luminosity the ratios are similar to GX 339-4, but at higher luminosities the radio jet is apparently under-luminous if tested against the "fundamental-plane" (section 4.1). Moreover, Gallo et al. (2014) performed a cluster and linear regression analysis on the hard and quiescent state of these XRBs (including a total of 24 systems). They found that a two cluster solution was favoured if the uncertainty of the luminosities is less than a factor of ~ 2. However, if one includes data collected on Cygnus X-1 there is no significant evidence for a bimodal distribution of tracks.

Although this analysis for Swift J1753.5-0127 clearly shows the source to be on the lower-branch of the $L_{\rm radio}/L_{\rm X-ray}$ relationship, it is not clear if the source prefers a similar power law relationship to that of GRS1915+105 or neutron stars (i.e. $\zeta \sim 1.4$). Rather, the scatter in the scaling relationship could be upper-branch variability albeit with a normalisation about an order of magnitude lower (to illustrate this in Figure 4.4, $\zeta \sim 0.7$ at four different decades are shown as blue dotted lines). Therefore, while variations in the radiative efficiency cannot be ruled out, that leads a different scaling of the observed X-ray luminosity with accretion rate, it must be noted that other parameters (e.g. such as Doppler boosting) could also have an important role at these Eddington ratios.

Jet activity is not found in the soft X-ray states and suppression occurs when the temperature of the blackbody disc increases. However, it is not clear if the jet-quenching mechanism is linked to a *relative* change in the disc to hard power law ratio or only an *absolute* drop in the hard power law component. To help constrain this I can use the combined *XMM-Newton*/*NuSTAR* measurement of Swift J1753.5-0127 during a different period of the soft state (chapter 3). In chapter 3 I fitted a hard power law component of $\Gamma = 1.79$ with a flux of $8.98^{+0.35}_{-0.24} \times 10^{-11}$ erg s^{-1} cm^{-2} (scaled to the 0.6-10 keV band) during a soft state, which was about $\sim$ 9% of the total flux (the rest was dominated by the blackbody and an additional soft, steep power law component). If I *assume* the same fractional flux for the hard power law during the JVLA soft state observation, then the inferred power law flux is $\sim 6 \times 10^{-11}$ erg s^{-1} cm^{-2}. This flux is a factor of ~ 10 less than the typical hard state level when the radio is around 300μJy. Thus if the radio flux scales just with the power law component, one expects $L_{\rm radio} = 300/10^{\zeta}\mu$Jy, which equates to 60 and 12 μJy for $\zeta = 0.7$ and 1.4, respectively. Although this is an estimate, it tentatively suggests that the hard power law to radio flux does not scale with the standard $\zeta = 0.7$ relationship.

Soft states have mostly been seen to occur at $\gtrsim 1\%\ L_{\rm Edd}$ (Maccarone, 2003; Kalemci et al., 2013), therefore one may consider jet suppression to only occur at high accretion of up to (and possibly beyond) the Eddington accretion rate. However, in chapter 3 I measured the soft state to be at an unusually low accretion rate ($0.72\%\ \dot{M}_{\rm Edd}$). I can therefore *rule out* a requirement that the accretion rate has to be larger than $\sim 1\%\ \dot{M}_{\rm Edd}$ for jet quenching to occur.

The deep JVLA observations in the soft state of Swift J1753.5-0127 show the deepest radio quenching of a transient BH XRB. Unlike the weak radio component seen in a soft-like state of Cygnus X-1, which may have been a failed state-transition (Rushton et al., 2012), there is no radio emission associated with the soft state of Swift J1753.5-0127. Although I compare this result on Swift J1753.5-0127 to the limit measured for 4U 1957+11 (Russell et al., 2011), it is important to note that the latter source has never been detected in the radio; thus the quenching factor for 4U 1957+11 is an estimate based on assuming the hard state flux follows the upper branch of the disc-jet relationship, which is not known for 4U 1957+11 and can vary widely between sources. However, since the jet flux is known for Swift J1753.5-0127, the estimate of the quenching factor can be much more accurate.

Chapter 5

No evidence for a low-mass black hole in Swift J1753.5-0127

"Don't you know the first law of Physics? Anything that's fun costs at least eight dollars"

Eric Cartman - South Park (Trapped in the Closet)

In this chapter I will conclude my study of Swift J1753.5-0127 by investigating the claims of a low-mass BH in the system made by Neustroev et al. (2014). I present optical spectroscopy of Swift J1753.5-0127, finding no evidence for the 'unidentified' narrow absorption and emission lines claimed to be associated with the donor. In addition, investigation of the H_α emission line shows that the mass of the compact object is likely $> 7.4 \pm 1.2 M_\odot$, much higher than previous suggestions of a low-mass ($< 5M_\odot$) BH (Neustroev et al., 2014). If the existence of such a low-mass BH were confirmed this would be the first instance of a BH existing in the "mass gap," the name given to the apparent gap in the mass distribution of compact objects between $2 - 5M_\odot$.

5.1 Introduction

Using the technique (described in section 1.3.4) of studying the donor in quiescent BHXRTs, and adding in the mass determinations in high mass X-ray binaries (HMXBs), there are now more than ~ 20 BH mass determinations (see Fig. 1.20 and Casares & Jonker, 2014). The distribution of these masses has become the subject of intense scrutiny from both an observational and theoretical viewpoint as, when combined with the substantial number of accurate neutron star mass measurements, there appears to be a dearth of compact objects with masses in the range $2-5M_{\odot}$ (Özel et al., 2010; Farr et al., 2011, and references therein, also see section 1.3.4.2). This has even been referred to as the "mass gap", and has prompted theoretical explanations based on the nature of the supernova mechanism that produced the BHs, ranging from convective instabilities at the time of the explosion to 'failed' supernovae in a certain mass range of red supergiants (Belczynski et al., 2012; Ugliano et al., 2012; Kochanek, 2014). Consequently, there is considerable interest in either (a) accounting for this mass gap as a selection bias of some form (e.g. Farr et al., 2011; Kreidberg et al., 2012), or (b) finding objects with masses in or close to this range, with significant implications for massive star evolution. Hitherto, the lowest mass BHXRT has been considered to be GRO J0422+32 ($\sim 5M_{\odot}$), but there has been a significant uncertainty in this value as a result of its poorly determined inclination (see Casares & Jonker, 2014, and references therein). The search has therefore been on for a low mass BHXRT with an accurately determined binary inclination, and hence a more accurate mass determination.

Swift J1753.5-0127 has been never been formally classified as a BH due to the source not having been observed in quiescence. No spectroscopic evidence of the donor has been obtained whilst the source has been in outburst, due to the optical emission being dominated by the accretion disc (Durant et al., 2009). With no detectable fluorescence emission either, it has therefore not been possible to obtain any direct evidence of the compact object mass and Swift J1753.5-0127 remains classified as a 'candidate' BH.

Remarkably, given the above summary of previous spectroscopic studies of Swift J1753.5-0127, Neustroev et al. (2014, hereafter N14) have presented evidence that it does contain a low mass ($< 5M_{\odot}$) BH, based on their discovery of narrow optical features (in both emission and absorption) which they associate with the donor. Given the considerable potential importance of the identification of a high inclination, low-mass BH in the "mass gap", I, along with collaborators, therefore undertook a spectroscopic study of Swift J1753.5-0127, using significantly higher spectral resolution than N14 so as to investigate its properties in much greater detail, and at the very least attempt to confirm the low-mass BH candidacy of Swift J1753.5-0127. I therefore focussed on the donor's features reported by N14, and report here my inability to reproduce any of their results. There was also interest in understanding the origin of the features reported by N14 as their wavelengths were not consistent with any known stellar lines.

5.2 Observations and Analysis

Swift J1753.5-0127 was observed from 2015 June 14 21:39:36 UT to June 15 04:44:55 UT (MJD 57187.903–57188.198) with the Intermediate dispersion Spectroscopic and

Imaging System (ISIS) on the 4.2-m William Herschel Telescope (WHT) at Observatorio del Roque de los Muchachos, La Palma, Spain. I obtained 25×900s exposures covering a total spectral range $\lambda\lambda 4174 - 7134$Å, utilising the R600B and R600R gratings and a 1" slit in photometric conditions of good ($\sim$ 1") seeing. I used IRAF (Tody, 1986) to perform standard reduction techniques to achieve wavelength calibration, cosmic ray removal using the external task "lacos" (van Dokkum, 2001) and extraction of the 1-dimensional spectra. CuAr+CuNe comparison arcs were obtained to calibrate the wavelength scale, achieving a central dispersion of 0.43 and 0.49 Å pixel^{-1} in the blue and red arms, respectively. I obtain a spectral resolution of 1.55 and 1.66Å (FWHM) in the blue and red arms, respectively. I also observed the spectral type standard stars HR 4949 (M5III), HR 4986 (M0III), HR 4929 (K0III) and HR 4962 (K5III), whose spectra were reduced and extracted in the same way. I flux-calibrated the averaged spectrum using the nearby flux standard star BD +33 2642 (Oke, 1990). I note that the observations were performed when Swift J1753.5-0127 was in the soft state (see chapter 3).

Much of the analysis of the extracted spectra was performed using Tom Marsh's MOLLY software package.[1] Computation of cross-correlation was performed separately for each arm of the spectrograph using the task XCOR, which computes the velocity shift of the target spectrum with respect to a template spectrum. I created 25 template spectra, each spectrum created by averaging all of the spectra of Swift J1753.5-0127 except for the target spectrum used for the calculation of the cross-correlation. For example, I cross-correlated spectrum 1 with a template created from the average of spectra 2–25. This removes the possibility of a false positive correlation. I cut the spectra in the blue arm above 5500Å due to large-scale variations in the flat-fields. The individual spectra and the template spectra were rebinned onto a uniform velocity scale in each arm and the continuum was subtracted by fitting a low-order spline to the data. Spectral features which may have affected the calculation of the cross-correlation function such as interstellar lines, H_α and He II λ4686Åwere masked out of the spectra and the templates before the calculation was performed. In the blue arm, cross-correlation was performed in the range $\lambda\lambda 4174 - 5500$Åand in the red arm in the range $\lambda\lambda 5618 - 7134$Å.

I also performed Doppler Tomography using the PYTHON implementation of Tom Marsh's DOPPLER package.[2] I used the continuum-subtracted spectra from each arm, trimmed around the lines of interest to compute the maps. To create the reconstructed trailed spectra from the resultant maps, I used the DOPPLER task COMDAT.

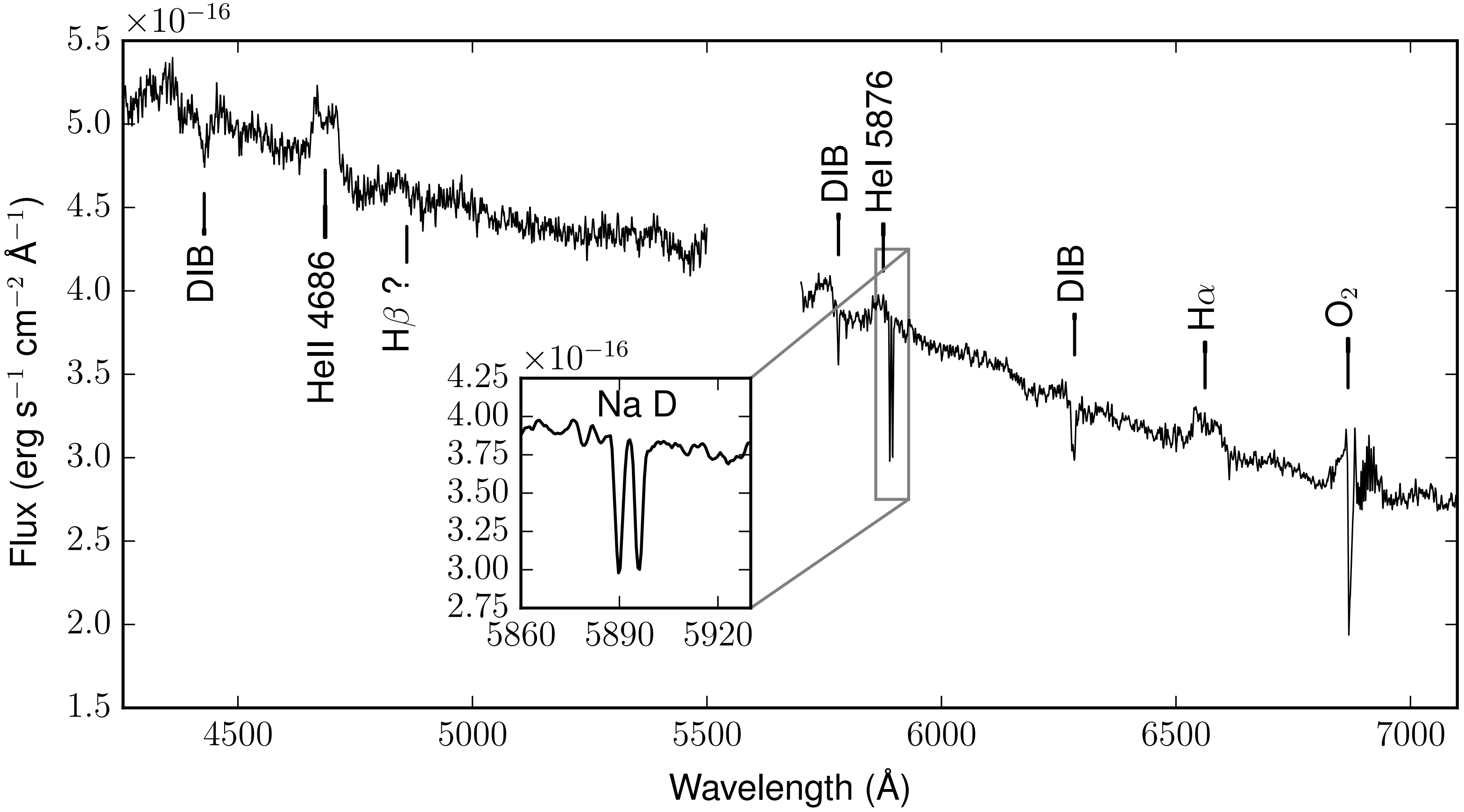

FIGURE 5.1: Flux calibrated averaged optical spectrum of Swift J1753.5-0127. Notable features are annotated. The inset shows a zoom of the Na D interstellar lines, demonstrating the resolution of the spectra.

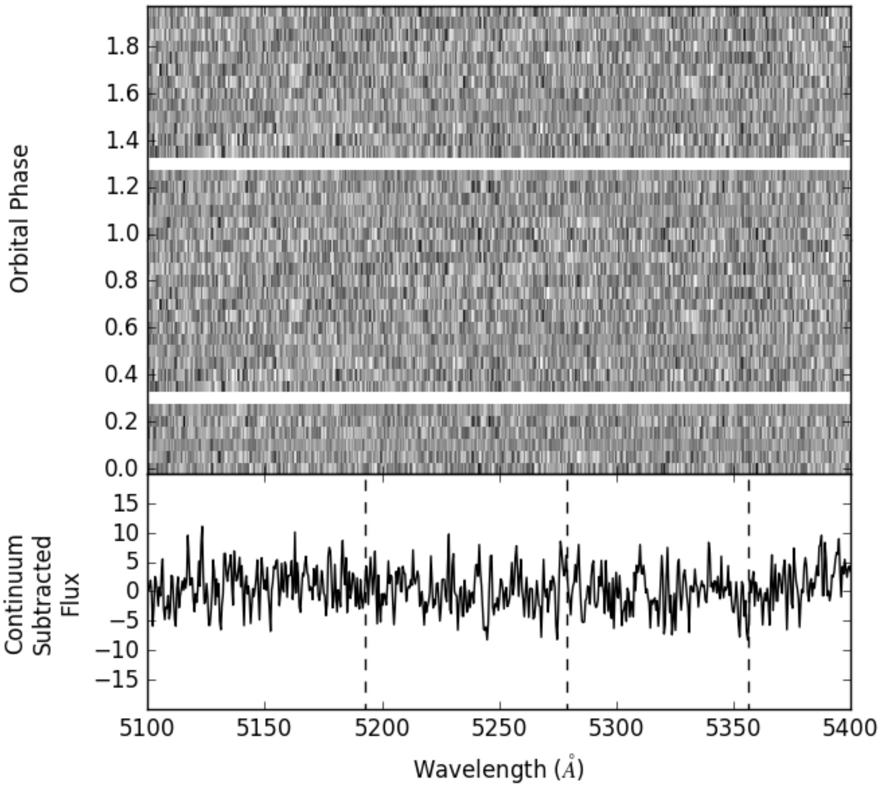

FIGURE 5.2: Top: The trailed spectrum of Swift J1753.5-0127 in the $\lambda\lambda 5100 - 5400$Årange, phase-folded on $P_{\rm orb}$ = 2.85h, as determined by N14. White indicates emission. Two cycles are shown for clarity. Bottom: The continuum subtracted, averaged spectrum of Swift J1753.5-0127. The dashed lines highlight the location of the narrow absorption and emission features seen by N14, which they associated with the secondary star.

5.3 Results

The flux-calibrated spectrum of Swift J1753.5-0127 is presented in Fig. 5.1 and exhibits strong double peaked He II $\lambda 4686$ and H_α emission lines along with evidence of weak Hβ emission and He I $\lambda 5876$, as had also been detected in previous spectroscopic studies of this source (Cadolle Bel et al., 2007; Durant et al., 2009). A number of diffuse interstellar bands (DIBs) are also present in the spectrum, most notably at $\lambda 4428$Åand $\lambda 6283$Åas well as the (resolved) interstellar Na D lines. I measure the equivalent widths (EWs) of the Na D interstellar lines to be 0.58 ± 0.03 and 0.55 ± 0.02 Å for Na D_1 and D_2 at $\lambda 5889$Åand $\lambda 5895$Å, respectively. This represents a decrease in EW from previous measurements (Durant et al., 2009) and such variability is indicative of some sodium being intrinsic to the system. The Fraunhofer B absorption features due to telluric O_2

[1]http://www2.warwick.ac.uk/fac/sci/physics/research/astro/people/marsh/software/
[2]https://github.com/trmrsh/trm-doppler

are also apparent at λ6867Å. I find no absorption features in the averaged spectrum which might be identified with the secondary star.

5.3.1 Companion star features

N14 presented evidence of 'unidentified' narrow absorption and emission features in the spectrum of Swift J1753.5-0127, which showed a sinusoidal modulation over their claimed 2.85h $P_{\rm orb}$. They concluded that the features, the strongest of which were observed at λ5193Å, λ5279Åand λ5356.1Å, were associated with the companion star and therefore the observed modulation was due to its orbital motion.

In order to investigate this claim, I phase-folded my spectra on the ephemeris calculated by N14. I created a trailed spectrum of the region where such features were noted by N14 ($\lambda\lambda 5100-5400$Å), and present this in Fig. 5.2. Studying the trails in Fig. 5.2, we see no evidence for any of the moving features seen by N14 in our WHT spectra. I also note that there is also no evidence for such features when I phase-fold the data on the $P_{\rm orb}$ determined by Zurita et al. (2008). To further examine the spectra for the presence of the features I also attempted to fit a number of Gaussians centred on the wavelengths of the observed lines to each spectrum. This was a repeat of the analysis of N14, but found that the fits did not converge with sensible results, confirming the non-detection of these features.

5.3.2 Cross-correlation

Cross-correlation was performed using the MOLLY task XCOR as detailed above. The resultant cross-correlation function (CCF) spectra were then phase-folded on the $P_{\rm orb}$ and ephemeris of N14, for comparison. I created trailed CCF spectra for each arm, which are presented in Fig. 5.3. The trailed spectra show no large deviations from 0 km s^{-1} and the sinusoidal modulation as seen by N14 is absent. I also note that there is no obvious modulation when the data are folded on $P_{\rm orb} = 3.24$h (Zurita et al., 2008).

I also cross-correlated the spectra of Swift J1753.5-0127 with four spectral type standards observed on the same night. I find no correlation with any of the spectral type templates, indicating that there are no features present in the spectrum of Swift J1753.5-0127 that can be associated with the range of late-type stars (K and M-type) most likely to be donors in this system.

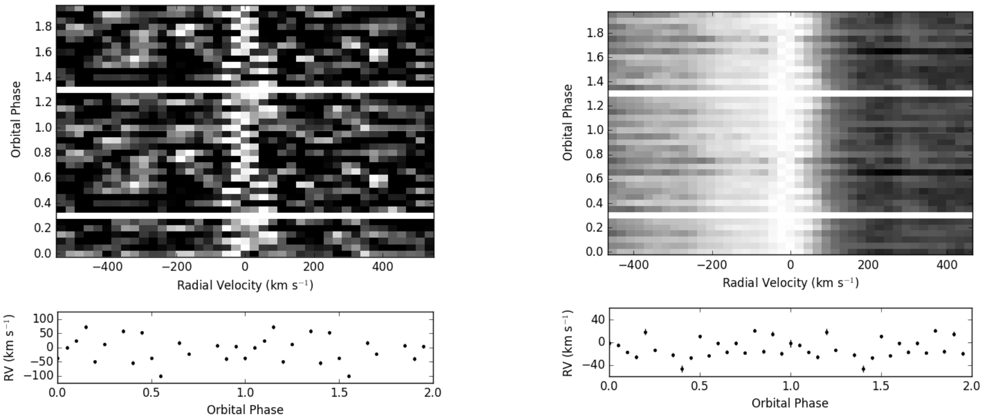

FIGURE 5.3: Left: Trailed, phase-folded CCF spectra from the blue arm. Right: Trailed, phase-folded CCF spectra from the red arm. Both datasets have been folded on the $P_{\rm orb}$ determined by N14. The lower panels of each trailed spectrum show the peak radial velocity obtained from the CCFs for each phase. Two phases are shown for clarity.

5.3.3 Disc emission lines

The optical spectrum exhibits He II $\lambda4686$ and H_α emission lines. The lines are very broad and both exhibit a double-peaked structure, very typical of emission features originating in an accretion disc (Smak, 1981; Horne & Marsh, 1986), however they are weak (EW $\sim$ 4Å for a double Gaussian fit to each line). To examine the line profiles, first I fit a double Gaussian to the emission lines in the phase-averaged spectrum, adopting a non-linear least-squares approach. From this I can obtain an estimate of the rotational velocity at the outer rim of the disc, $v_D \sin i$, by measuring half the observed peak-to-peak separation (Smak, 1981; Warner, 1995). Taking H_α, as this originates in the outermost regions of the accretion disc, I estimate $v_D \sin i = 865 \pm 25$km s^{-1}. For comparison, from the double-peaked He II $\lambda4686$ emission I calculate $v_D \sin i = 1115 \pm 29$km s^{-1}, as expected since He II is formed closer in to the compact object.

The double-peak separation of the H_α line profile can be used to estimate the radial velocity semi-amplitude, K_2 of the companion star in BHXRTs (Orosz et al., 1994; Orosz & Bailyn, 1995). In quiescent BHXRTs, the ratio v_D/K_2 has been shown to be $\simeq 1.1 - 1.25$. For Swift J1753.5-0127, I therefore find a very conservative lower limit of $K_2 = 692 \pm 20$ km s^{-1}. It must be noted that this value is likely underestimated due to the source not yet being in quiescence. In outburst, the accretion disc expands to a radius larger than that in quiescence, therefore v_D is smaller in outburst. K_2 can be used to constrain the mass of the compact object, M_1, by calculating the mass function:

$$f(M_1) = \frac{P_{\rm orb} K_2^3}{2\pi G} = \frac{M_1^3 \sin^3 i}{(M_1 + M_2)^2} \tag{5.1}$$

where i is the inclination of the system and M_2 is the mass of the donor (see section 1.3.4). In the case of Swift J1753.5-0127, which is a LMXB, then the mass function represents a firm lower limit to M_1. Using $K_2 = 692 \pm 20$ km s^{-1} and $P_{\rm orb} = 3.2443 \pm 0.0010$h (actually the superhump period, only slightly larger than $P_{\rm orb}$; Zurita et al. 2008), I obtain $M_1 > 4.6 \pm 0.3 M_\odot$. This again strongly indicates that the compact object in Swift J1753.5-0127 is a BH. The fact that this is a very conservative lower limit on the mass reinforces the case for a BH primary.

Recently, Casares (2015) discovered that the FWHM of a single Gaussian fitted to the H_α line profile is tightly correlated with $K_2 = 0.233(13) \times$FWHM in quiescent BHXRTs. As above, this relation is only valid for quiescence, but as the accretion disc expands during an outburst, the FWHM gets smaller, thus $\text{FWHM}_{(\text{outburst})} < \text{FWHM}_{(\text{quiescence})}$. I find FWHM $= 3470 \pm 214$ km s^{-1}, which translates to $K_2 > 808 \pm 67$ km s^{-1}. When combined with $P_{\rm orb}$ I find $M_1 > 7.4 \pm 1.2 M_\odot$. This again provides a conservative lower limit on the mass of the compact object, higher than that calculated from the double peak separation.

Another way of constraining the mass of the compact object in Swift J1753.5-0127 is by scaling the FWHM of the H_α line with that of another system with well determined system parameters, such as XTE J1118+480. Since FWHM scales with $\sin i \left(\frac{M_1}{P_{\rm orb}}\right)^{1/3}$ then:

$$M_1 \sin^3 i_{(\text{J1753})} = M_1 \sin^3 i_{(\text{J1118})} \left(\frac{\text{FWHM}_{(\text{J1753})}}{\text{FWHM}_{(\text{J1118})}}\right)^3 \times \left(\frac{P_{\text{orb}(\text{J1753})}}{P_{\text{orb}(\text{J1118})}}\right) \tag{5.2}$$

Adopting for XTE J1118+480 the following parameters: $M_1 = 7.5 M_\odot$, $i = 73°$ (Khargharia et al., 2013), $P_{\rm orb} = 0.170$d (González Hernández et al., 2012) and FWHM=2850 km s^{-1} (Casares, 2015), and combining these values with my parameters for Swift J1753.5-0127, the scaling yields $M_1 \sin^3 i_{(\text{J1753})} \approx 9.4 M_\odot$ and even $\approx 8.3 M_\odot$ if $P_{\rm orb} = 2.85$h (from N14) is assumed. Again, these values are lower limits because the FWHM has been measured in outburst and hence is an underestimate of the quiescent value. Therefore, the scaling of FWHM with XTE J1118+480 suggests that, in contrast with N14, the BH in Swift J1753.5-0127 is actually rather massive, even in the extreme case of an edge-on system.

I can also use the disc emission lines to investigate the motion of the compact object around the centre of mass, i.e. K_1. To do this I cross-correlated the individual spectra with the phase-averaged spectrum, masking all but the He II and H_α lines. However, the resultant CCFs were consistent with 0 km s^{-1} within 1σ statistical uncertainties of 22 km s^{-1}, indicating that the orbital motion of the BH could not be detected. This is contrary to N14, who claimed a value of $K_1 = 52 \pm 10$ km s^{-1} by measuring the centroid of the

He II $\lambda4686$ emission feature, although N14 cautioned that the parameters obtained are plagued with systematic errors. I conclude that, though the WHT spectra are higher resolution than those of N14, the orbital motion of the BH cannot be detected as my analysis is limited by the signal-to-noise ratio of the individual spectra. Furthermore, the overall emission line profile may not accurately trace the motion of the primary (see eg. Orosz et al., 1994).

5.3.3.1 Doppler Tomography

One can study the line profiles in more detail by examining the trailed spectra, which show variations of the blue and red peaks of the double-peaked line profiles. The orbital variation of the lines enables one to study the disc structure using the technique of Doppler tomography. Doppler tomography is a technique which uses the information encoded in line profiles as a function of orbital phase to calculate the strength of emission as a function of velocity. The end result is a visual representation of the emission regions of certain spectral features in velocity space. A phase-resolved series of a particular emission line (for example He II $\lambda4686$) is equivalent to a series of projections in velocity space at different orbital phases, enabling one to reconstruct the emission region of the particular line.

I utilised the maximum entropy implementation of Doppler tomography using Tom Marsh's DOPPLER software package in which the image of maximum entropy for a given goodness-of-fit (measured with χ^2) is sought (see Marsh & Horne 1988 for technical details). The resultant tomograms are presented in Fig. 5.4, where I have marked the Roche lobe of the compact object (dashed line) and the secondary (solid line) using the system parameters of Zurita et al. (2008). The system parameters are not well known for Swift J1753.5-0127, so the plotted Roche lobes are estimates; nevertheless, they represent typical values for LMXB BH systems (see Casares & Jonker 2014), which I believe to be more appropriate for Swift J1753.5-0127 than those of N14 (see section 5.4.3). The associated observed and reconstructed trailed spectra are presented in Fig. 5.5.

The tomograms show clearly the disc structure where the double peaked emission line profiles originate. The radii of the annuli are different for He II and H_α, with H_α exhibiting smaller velocities - indicative of the smaller peak-to-peak separation in the line. The emission for both lines is roughly symmetric, showing none of the enhanced structure seen by N14. I also constructed tomograms using the system parameters calculated by N14, also presented in Fig. 5.4. However, they do not exhibit the same

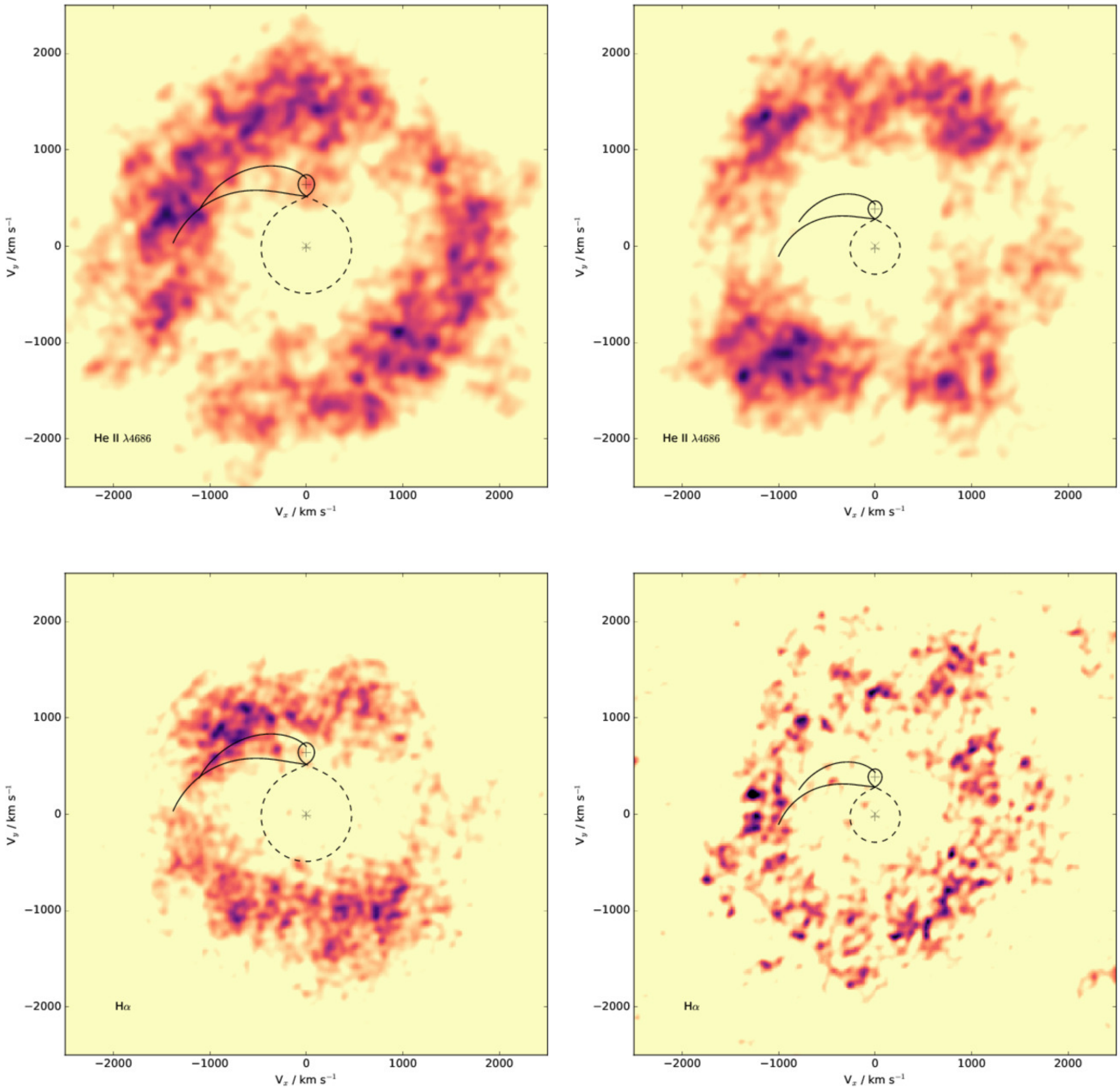

FIGURE 5.4: Doppler tomograms for the He II $\lambda4686$ (upper) and H_α (lower) emission lines. The two left panels were constructed utilising the system parameters of Zurita et al. (2008), the two right panels were constructed using those of N14.

'clean' disc structure, instead showing four distinct regions of enhanced 'clumpy' emission rather than the uniform disc seen using the parameters from Zurita et al. (2008).

It is important to note that the tomograms computed with the system parameters of N14 in Fig. 5.4 show a disc constrained to emit only from an inner fraction of its Roche lobe. With ongoing mass transfer (for this very extended outburst) it is far more likely that emission extends out to velocities associated with the orbit of the donor. Such structure is then seen in the tomograms calculated using the parameters of Zurita et al. (2008) as is also clear in those of XTE J1118+480 (see Fig. 5 of Torres et al. 2002).

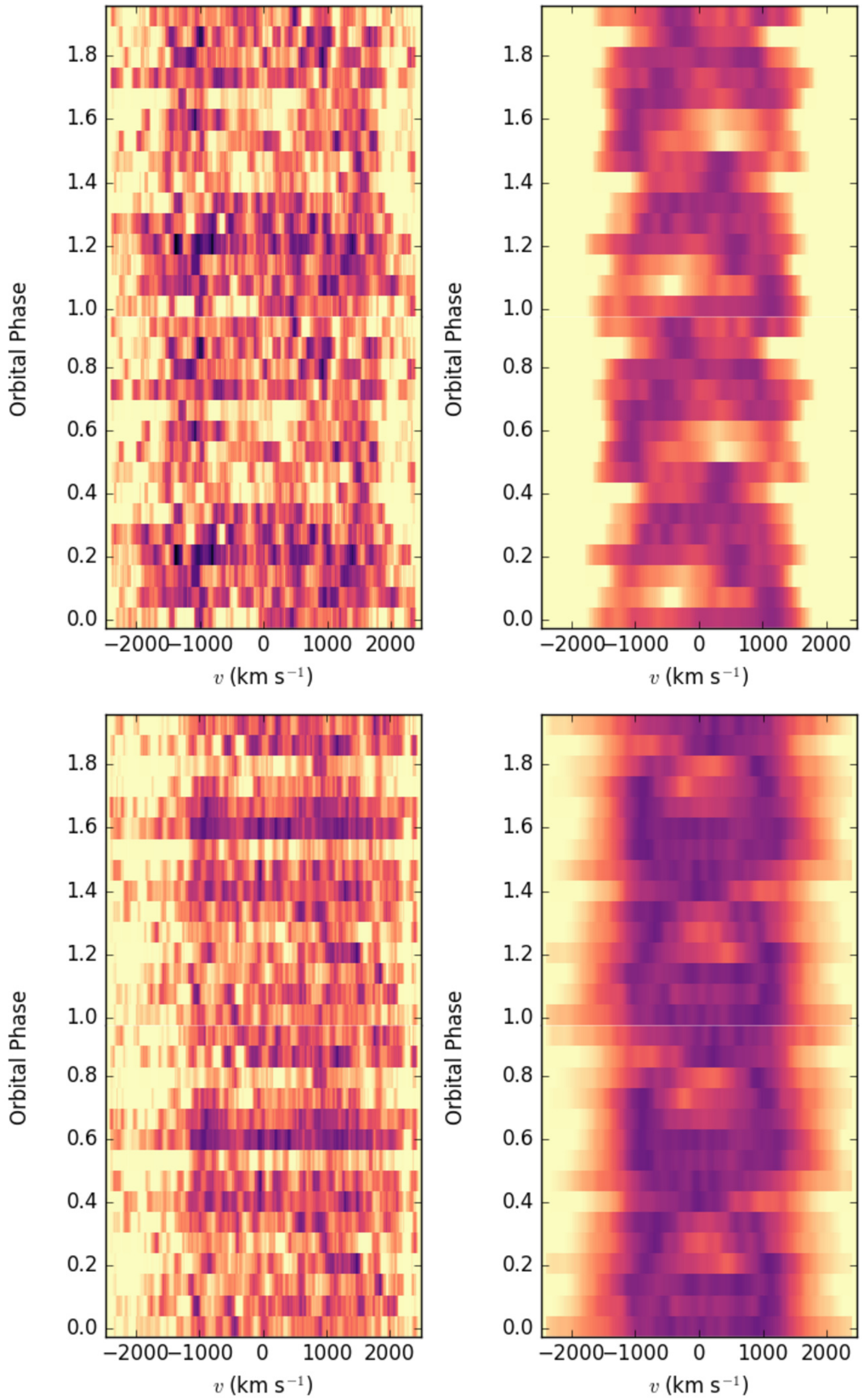

FIGURE 5.5: Observed and reconstructed trailed spectra for the He II $\lambda4686$ (upper) and H_α (lower) emission lines. The trails were constructed using the system parameters of Zurita et al. (2008).

5.4 Discussion

5.4.1 Orbital Period

N14 determined a period of 2.85h by performing time-series analysis on both their spectroscopic and photometric data. The source is known to show strong modulations in its optical light curve (Zurita et al., 2008), but N14 also found similar variability to be present in their time-resolved spectroscopy. The Lomb-Scargle (Lomb, 1976; Scargle, 1982) periodograms for both their photometric and spectroscopic data show the strongest peaks at $\sim$ 8.4 cycles d^{-1}, leading to their proposed $P_{\mathrm{orb}} = 2.85 \pm 0.01$h to be the true orbital period. However, it is evident from their periodograms that there are a number of significant peaks close to the chosen frequency, one of which is the previously determined superhump period of 3.24h (Zurita et al., 2008). It is clear that the timing analysis performed by N14 suffers from aliasing, which is most likely due to the low number of photometric observations obtained, many of which do not cover a complete orbital cycle. Zurita et al. (2008) obtained 20 photometric observations of $\sim$ 6h per night, of significantly greater phase coverage. In addition, the variability of the nightly light curves is non-sinusoidal, meaning the phase-dispersion minimisation technique (PDM; Stellingwerf 1978) allowed a more accurate determination of the periodicities present than Lomb-Scargle time-series analysis. I therefore choose $P_{\mathrm{orb}} \approx 3.24$ h as the orbital period of Swift J1753.5-0127.

To further investigate this disagreement over which is the correct value of P_{orb}, I re-examined the light curves presented by Zurita et al. (2008). I selected R-band photometry from four consecutive nights (27-30 Jun 2007) of observations, in order to compare with the variability demonstrated in the spectroscopy of N14. A subset of the Zurita et al. (2008) light curves was chosen such that each night of photometry matched the observation duration of the corresponding spectroscopic observation of N14. For example, the 27 Jun 2007 observation was cut from 5.09h to 1.97h to match the length of the Aug 06 2013 spectroscopic observation by N14. I then calculated the PDM and Lomb-Scargle periodograms, separately, for the photometry that matched the sampling of the N14 spectroscopy, and these are presented in Fig. 5.6. The upper two panels show that when the data has the same sampling as that of N14, aliasing becomes a serious problem.

The Lomb-Scargle periodogram (Fig. 5.6; middle panel) shows a very similar structure to N14's Fig. 4, with a number of peaks showing high power, including those corresponding to periods of $\approx$ 3.24h and $\approx$ 2.85h. The morphology of the periodograms in Fig. 5.6 highlights the difficulty of disentangling which is the correct periodicity. The longer timebase and more extensive dataset of Zurita et al. (2008) removes this problem by including many more complete orbital cycles, with $\approx$ 3.24h emerging as the most likely value of $P_{\rm orb}$.

This is further illustrated in the bottom panel of Fig. 5.6, which shows the Lomb-Scargle periodograms of two simulated light curves. These have the same filtering applied to them as discussed above (i.e. the same sampling and duration as the N14 spectroscopy) but are simulated as a perfect sine curve with periodicities of 3.24h and 2.85h. The periodograms of the simulated data are almost indistinguishable from one another, highlighting the problem of aliasing. Indeed, the periodogram of the $P_{\rm orb}$ = 2.85h exhibits the highest peak at 3.24h, making it difficult to identify which is the true periodicity. Only with a longer data-set, such as that of Zurita et al. (2008), will the effects of aliasing be reduced and the true value of $P_{\rm orb}$ become more apparent. This is seen in Fig. 5.7, which shows the Lomb-Scargle periodograms of two sine curves with periodicities of 3.24h and 2.85h, created using the same sampling as the full light curves (i.e. 20 nights of photometry) presented by Zurita et al. (2008). It is clear from Fig. 5.7 that with a longer data-set, though aliasing is still apparent, it is more straightforward to determine which is the true period.

Contrary to N14, $P_{\rm orb} \approx$ 3.24h puts Swift J1753.5-0127 outside the so-called 'period gap' of binary systems in the range 2.15–3.18h. In the more numerous accreting white dwarf (AWD) binaries, the well-determined period gap (Knigge et al., 2011) is explained by the switching off of the magnetic braking mechanism (which slows down the spin period of the companion star and hence reduces $P_{\rm orb}$). This causes the donor star to shrink and mass-transfer stops due to the companion not filling its Roche lobe. It is not clear if there is the same period gap in BHXRTs as in AWDs (see e.g. King et al. 1996). Nevertheless, I find that the $P_{\rm orb}$ of Swift J1753.5-0127 is close to the edge of this gap and thus may well be still filling its Roche lobe, which is evident from the persistent disc emission seen at optical and X-ray wavelengths. However, it is still unclear why the source has been persistent since its discovery as a transient in 2005.

5.4.2 Companion Star Features

I do not find the lack of features associated with the companion star to be surprising. Swift J1753.5-0127 has been a persistent X-ray source since its initial outburst in 2005 and is much brighter than the pre-outburst limit of the DSS (R$\lesssim$ 21), hence the donor must be fainter than this. Furthermore, the optical spectrum is typical of that of an accretion disc, exhibiting very few features other than the broad, double-peaked He II λ4686 and H_α emission lines. The apparent companion features present in the optical spectrum of N14 remain unidentified, as (a) they are not at the wavelengths of any

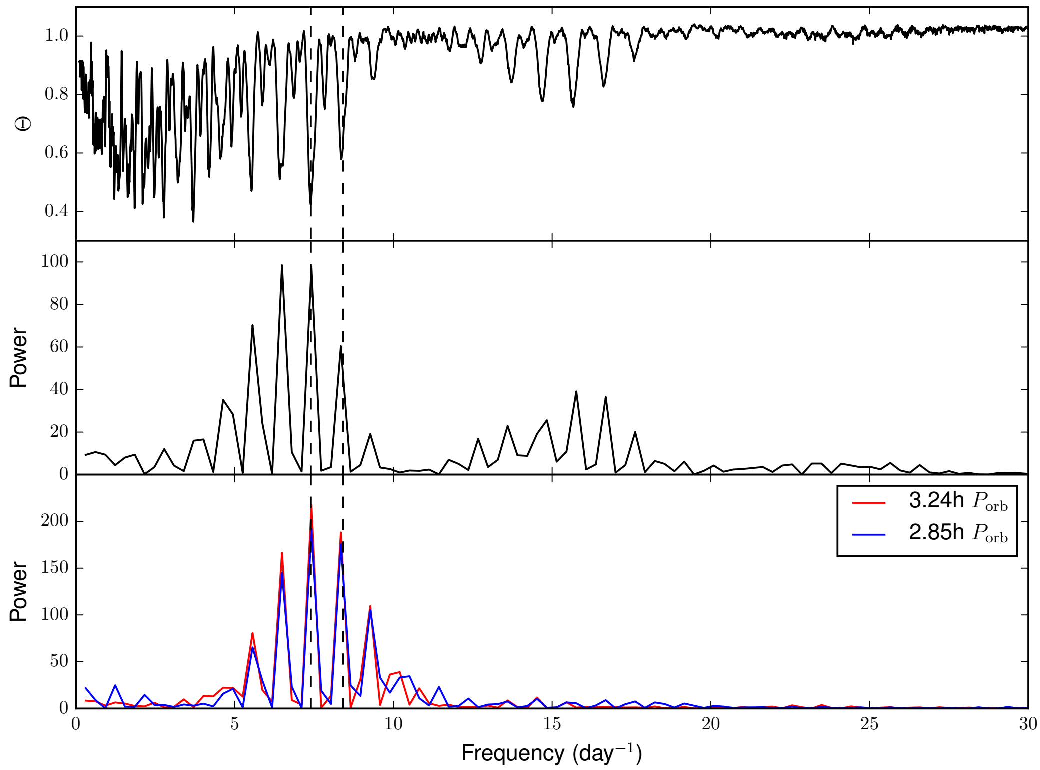

Figure 5.6: *Top*: PDM periodogram of the R-band nightly photometry from Zurita et al. (2008) which has been filtered to match the duration of the spectroscopic observations of N14 (see text for full description). *Centre*: Lomb-Scargle periodogram of the same photometry. *Bottom*: Lomb-Scargle periodograms of light curves created by simulating a sine curve with a period of 3.24h (Red) and 2.85h (Blue) using the same sampling as the filtered photometry in the upper two panels. The vertical dashed lines represent the two determined values of $P_{\rm orb}$; 3.24h (left) and 2.85h (right).

normal late-type stellar features and (b) I find no evidence for their presence in the higher resolution WHT spectrum (Fig. 5.2). Furthermore, the lack of any significant correlation with a wide range of late-type stellar template spectra suggests that any companion star features are washed out by the accretion disc.

However, it could be possible that the spectral templates I used do not accurately represent the spectral type of the companion star in Swift J1753.5-0127. For this reason I also cross-correlated each spectrum with templates created by averaging all the spectra, apart from the target spectrum of the cross-correlation. However, the CCFs showed none of the signals seen by N14 (Fig. 5.3). I therefore conclude that there are no spectral features associated with the companion present in the WHT spectra of Swift J1753.5-0127.

The noise in the mean spectrum (Fig. 5.1) indicates that normal (∼G-K star) absorption features should have been detected had they been present at the $\sim 2\%$ level with respect to the continuum (as with N14's spectrum). Since Swift J1753.5-0127 had $V \sim 17$ at

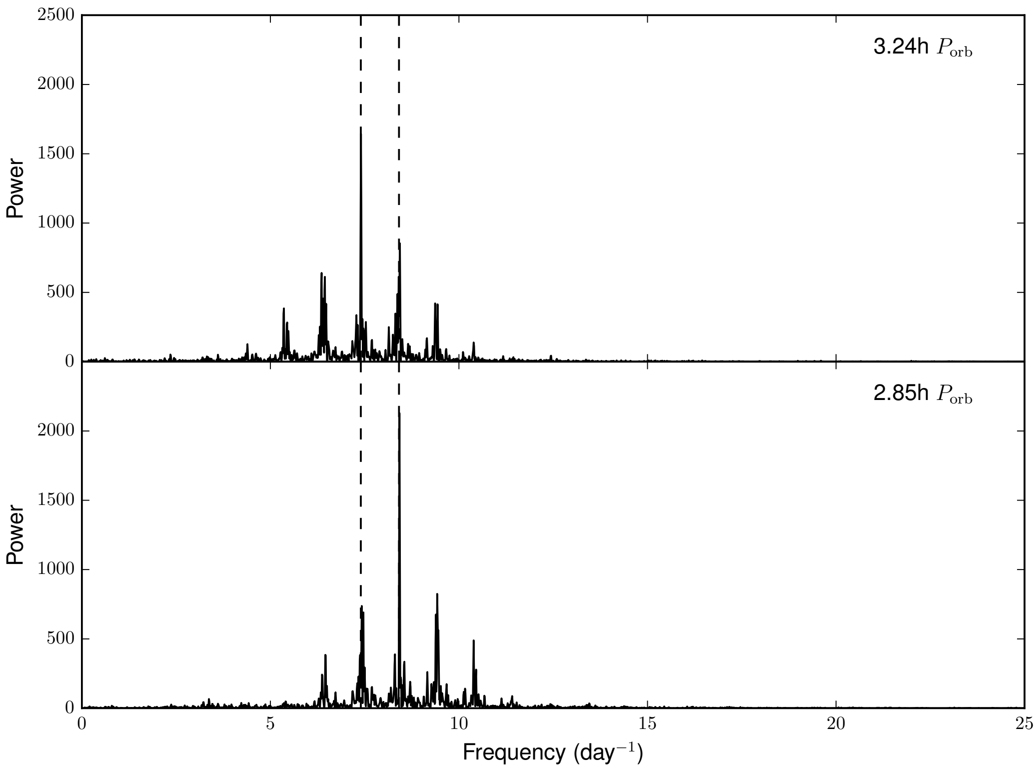

FIGURE 5.7: Lomb-Scargle periodogram of light curves created by simulating a sine curve with a period of 3.24h (*Top*) and 2.85h (*Bottom*) using the same sampling as the light curves presented by Zurita et al. (2008). The vertical dashed lines represent the two proposed values of $P_{\rm orb}$; 3.24h and 2.85h at frequencies of ~ 7.4 and ~ 8.4 day^{-1}.

the time of my observations (Neustroev et al., 2015), this implies that the donor must be fainter than $V \sim 21$, which is consistent with its non-detection in the DSS as noted earlier. I again point out that the so-called absorption features detected by N14 do not correspond with those of any normal late-type star and imply a donor that is brighter than this limit.

What could explain the apparently moving features seen by N14? The Boller and Chivens spectrograph on the 2.1m telescope at the Observatorio Astronómico Nacional in Mexico was used to obtain the results presented by N14. They chose a wide slit width of 2.5" despite the reported much better seeing conditions ($\sim$ 1") during the time of the observations. Seeing variations and imperfect telescope pointing can lead to variations in the illumination profile of the source on the CCD. In particular, the 2.5" slit corresponds to 65μm at the spectrograph's plate scale of 38.4" mm^{-1}, which represents a wavelength spread of 8.1Å with their 400 lines mm^{-1} grating. If the seeing is much better than 2.5", then velocity shifts approaching 600 km s^{-1} could be induced by telescope tracking errors causing a shift of the stellar image within the slit.

However, this movement within the slit would only cause the variability seen if the N14 absorption features are real, yet I have been unable to confirm their existence. One explanation for this is to note that, when performing the cross-correlation, N14 appear to mask only the disc emission and night sky lines, which suggests that the interstellar absorption lines such as the DIBs and Na D were included in the calculation of the CCF. Therefore, telescope tracking errors could have given the impression of these features moving and could be responsible for the apparent RV variability that is seen by N14.

I also note that Fig 2. of N14 shows that the blue portion of the spectrum exhibits dramatic variability ($\sim 2\times$ in flux) over the course of the observations, and this may also be a manifestation of the source drifting within the wide slit. Indeed, this interpretation is strongly supported by the stability of B-band observations, which have only ever shown very low level variability (< 0.2mag).

5.4.3 Mass of the primary

Using the recently derived FWHM(H_α)-K_2 correlation (Casares, 2015), I can obtain an independent estimate of the likely mass, M_1, of the primary. I find, conservatively, $M_1 > 7.4 \pm 1.2 M_\odot$, which is a strong indication that the primary is almost certainly a BH, as also indicated by its spectral properties. N14 claim that it is a low mass BH ($< 5M_\odot$) based on their companion star radial velocity curve yielding a K_2 velocity of ~ 380 km s^{-1}, significantly lower than the estimates I present in this work (section 5.3.3). However, I am not able to replicate the results of N14 with the WHT spectra presented here. Therefore I suggest that the mass of the BH is much higher than previously suggested by N14 and hence there is no spectroscopic evidence for a low-mass BH in Swift J1753.5-0127.

N14 claim that Swift J1753.5-0127 lies in the so-called 'mass gap,' a gap in the distribution of known compact object masses in the range $2 - 5M_\odot$ (Bailyn et al., 1998; Özel et al., 2010). The presence of sources in the mass gap may give an indication of the formation scenario of such systems, with BH masses in the range $2-5M_\odot$ suggestive of a delayed supernova explosion scenario (Belczynski et al., 2012). However, with the mass estimate inferred from the H_α FWHM, I instead place Swift J1753.5-0127 well outside the mass gap, instead falling in the canonical BH mass distribution around $\sim 7M_\odot$ (Özel et al., 2010).

5.5 Conclusions

Swift J1753.5-0127 has now been active for >10 years, which has made it difficult to calculate the system's parameters using the normal methods applied to LMXB BH systems. I have obtained and analysed medium resolution spectroscopy in order to compare my results to those of N14, who claim a very low-mass BH ($< 5M_{\odot}$) and a short (2.85h) orbital period. I find that I cannot replicate any of the results of N14, finding no spectroscopic evidence of the companion star. Instead, I derive a much higher compact object mass ($M_1 > 7.4 \pm 1.2M_{\odot}$), leaving no doubt that the source contains a BH. I also find that the shorter $P_{\rm orb} = 2.85$h preferred by N14 is likely a result of aliasing, and my analysis supports the $P_{\rm orb}$ of 3.24h found by Zurita et al. (2008), even though it is likely the (fractionally longer) superhump period. It is clear that the search for a BH in the so-called "mass gap" must continue.

Chapter 6

Testing the DIM: The 2015 outburst of V404 Cyg

"We'll simply set a new course for that empty region over there, near that black-ish, hole-ish thing."

Zapp Brannigan - Futurama (A Flight to Remember)

In this chapter, I present optical spectroscopy of the BHXRT V404 Cyg taken ~ 13 hours before the 2015 outburst was detected by X-ray telescopes, representing the first ever 'pre-outburst' spectrum of a BHXRT. Combined with long-term optical monitoring of the source obtained by collaborators, which exhibits an optical precursor to the fast rise, I present a test of the DIM. Together with collaborators I propose that the outburst of V404 Cyg was produced by a thermal-viscous instability triggered close to the inner edge of a truncated disc. An X-ray delay of a week is consistent with the time needed to refill the inner region and hence move the inner edge of the disc inwards, allowing matter to reach the central BH, finally initiating the X-ray emission.

In this chapter, sentences using active voice describe the work I have done, whereas sentences using passive voice describe work undertaken by my collaborators Federico Bernardini and Dave Russell.

6.1 Introduction

GS 2023+338 was discovered in 1989 by the *GINGA* X-ray satellite (Makino, 1989) and quickly associated with the previously known variable star V404 Cyg (hereafter V404;

Wagner et al., 1989), making it the first SXT with a previously known optical ID (as Nova Cyg 1938). As one of the closest known LMXBs (2.39 ± 0.14 kpc; Miller-Jones et al., 2009), V404 is well studied and is known to contain a $9^{+0.2}_{-0.6} M_{\odot}$ BH (Khargharia et al., 2010) with $P_{\rm orb} = 6.4714 \pm 0.0001$ (Casares & Charles, 1994). The BAT aboard *Swift* triggered on V404 on 2015 June 15 18:31:38 UTC (Barthelmy et al., 2015) when a new outburst was detected. The outburst was detected across multiple wavelengths (Negoro et al., 2015; Mooley et al., 2015; Ferrigno et al., 2015a; Gazeas et al., 2015) and the light curve exhibited multiple flaring episodes, with luminosities reaching near-Eddington values (Ferrigno et al., 2015b; Rodriguez et al., 2015).

Due to the well-studied nature of V404 and the global multi-wavelength effort to observe it, the 2015 outburst represents the ideal opportunity to test theories of accretion, in particular the Disc Instability Model (DIM; see section 1.3.1). The DIM can broadly explain the outburst cycle of LMXBs, but only if the inner disc is truncated during quiescence (Dubus et al., 2001). The DIM predicts that in LMXB transients with low mass transfer rates, only 'inside-out' outbursts can occur (see Equation (51) of Lasota, 2001), i.e. the thermal-viscous instability is triggered well inside the accretion disc and will propagate outwards. The heating front does not start exactly at the inner edge of the disc and instead propagates both ways. The 1996 outburst of GRO J1655-40 was described as an 'outside-in' outburst due to an observed delay in X-ray emission with respect to the optical rise (Orosz et al., 1997). However, subsequent modelling of the rise of the outburst (Hameury et al., 1997) determined that the outburst was in fact inside-out. In this model, the disc is truncated at a radius much larger than $R_{\rm ISCO}$ and the outburst starts at the inner edge of this cold, truncated disc, far from the BH. The thermal-viscous instability propagates outwards from the inner edge of the disc, initiating the optical rise whilst the inner 'hole' is filled in with an Advection Dominated Accretion Flow (ADAF; Narayan & Yi, 1995a,b) on a viscous timescale. Since the disc X-ray emission is mainly emitted in the innermost regions of the disc, a delay of several days in the X-ray rise with respect to the optical emission is expected. In the case of a non-truncated disc the delay would be at most 1 day (Dubus et al., 2001).

An optical precursor to the X-ray detection of V404 was detected a week before the BAT trigger (Bernardini et al., 2015). Combining this with optical spectroscopy obtained ~ 13 hours before the BAT trigger, collaborators and I were able to test the DIM in the context of BHXRTs.

6.2 Observations and Data Reduction

6.2.1 Optical photometry

Observations of V404 were taken with the robotic 2m Faulkes Telescope North (FTN) at Haleakala, Maui, USA. Imaging was obtained in Bessell V, R and Sloan Digital Sky Survey i' filters since 2006 April, as part of a monitoring campaign of $\sim$ 40 LMXBs (Lewis et al., 2008). More than nine years of data (from 2006 April 8 to 2015 June 9) is presented here. Observations were typically made once per week when V404 was visible, and exposure times are 200 s in each filter. Automatic pipelines de-bias and flat-field the FTN science images.

There is a field star of magnitude $V = 18.90 \pm 0.02$, $R = 17.52 \pm 0.01$, $i' = 16.92 \pm 0.01$ $1.4''$ north of V404 (Udalski & Kaluzny, 1991; Casares et al., 1993; Barentsen et al., 2014). The two stars are blended in all images, so my collaborators performed aperture photometry using PHOT in IRAF (Tody, 1986) adopting an optimum fixed aperture radius of 12 pixels ($3.6''$) to encompass the flux of both stars. The same aperture was used for photometry on four comparison stars $13 - 34''$ from V404. These were used for flux calibration, and themselves calibrated using field stars of known magnitudes listed in Udalski & Kaluzny (1991) for V-band, Casares et al. (1993) for R-band and the second data release of the IPHAS (INT Photometric H_α Survey of the Northern Galactic Plane catalog; Barentsen et al. 2014) for i'. Magnitudes of V404 were obtained in total from 392 usable images.

6.2.2 Optical Spectroscopy

I observed V404 on 2015 June 15 05:07:29 UTC (MJD 57188.214) with the Intermediate dispersion Spectroscopic Imaging System (ISIS) on the 4.2m William Herschel Telescope (WHT) at Observatorio del Roque de Los Muchachos, La Palma, Spain. I obtained two 600s exposures covering a total spectral range $\lambda 4173 - 7153$Åutilising the R600B and R600R gratings and a $1''$ slit in photometric conditions of good ($\sim 1''$) seeing. I used IRAF (Tody, 1986) to perform standard reduction techniques to extract the 1-dimensional spectra and perform wavelength calibration. CuAr+CuNe comparison arcs were obtained to calibrate the wavelength scale using a low-order polynomial fit to the pixel-wavelength data, achieving a central dispersion of 0.43 and 0.49Å pixel^{-1} in the blue and red arms, respectively. A spectral resolution of 1.55 and 1.66Å (FWHM) is achieved in the blue and red arms, respectively. The spectrum was flux-calibrated using the nearby flux standard star BD +25 4655 (Oke, 1990). The WHT observations were previously reported by (Munoz-Darias et al., 2015) but are presented here in greater detail.

6.3 Results

6.3.1 Optical Photometry

Fig. 6.1 shows the optical light curve in the 3 optical bands, from 2006 up to the time of the BAT trigger in 2015 (MJD 57188.772). The red points in Fig. 6.1 represent observations from a week before the BAT trigger and exhibit the highest magnitudes recorded throughout the entire 9 year period.

With the $\sim$ 9 years of FTN data, an orbital light curve was also generated using the orbital ephemerides of Casares & Charles (1994). Adopting $P_{\rm orb} = 6.4714 \pm 0.0001$ day and $T_0 = 2448813.873 \pm 0.004$ HJD, the orbital light curve is presented in Fig. 6.2 and exhibits the typical variability associated with the tidally distorted face of the donor (the ellipsoidal modulation; see Fig. 1.18). Low amplitude flaring, likely due to residual accretion activity, is also present and has been documented before in V404 (Shahbaz et al., 2003; Hynes et al., 2004, 2009b; Zurita et al., 2004; Bernardini & Cackett, 2014).

The orbital light curves are fit (apart from the last two points) with a constant plus double sinusoid function, whose phases are allowed to vary so as to account for unequal minima and maxima (see Section 1.3.4) as has been seen in V404 (Zurita et al., 2004). On 2015 June 8 (MJD$\sim$ 57181.5, phase $\phi \sim 0.11$), and 9 (MJD$\sim$ 57182.5, $\phi \sim 0.25$) the optical magnitude in all bands is significantly brighter than the average quiescent modulation level by $0.1 - 0.3$ mag, and above the low amplitude flaring behavior (where Δ mag $\lesssim 0.1$).

The best-fit model is then subtracted from the light curves in Fig. 6.1, resulting in the residual light curves (Fig. 6.3). The last two points of the residual light curves have the highest residuals and there appears to be a long-term (years) trend present in the form of a slow decay followed by a rise. To characterise this trend a Spearman's rank test is performed on the R and i' band residual light curves, where the signal-to-noise ratio (S/N) was higher compared to the V-band observations. The Spearman's rank coefficient is found to be $\rho = 0.78$, and the null hypothesis probability $P = 3.5 \times 10^{-27}$, indicating that the residuals are positively correlated.

The strong positive correlation, coupled with the small uncertainties on each data point suggest that the observed variability is intrinsic to the source and is likely accretion

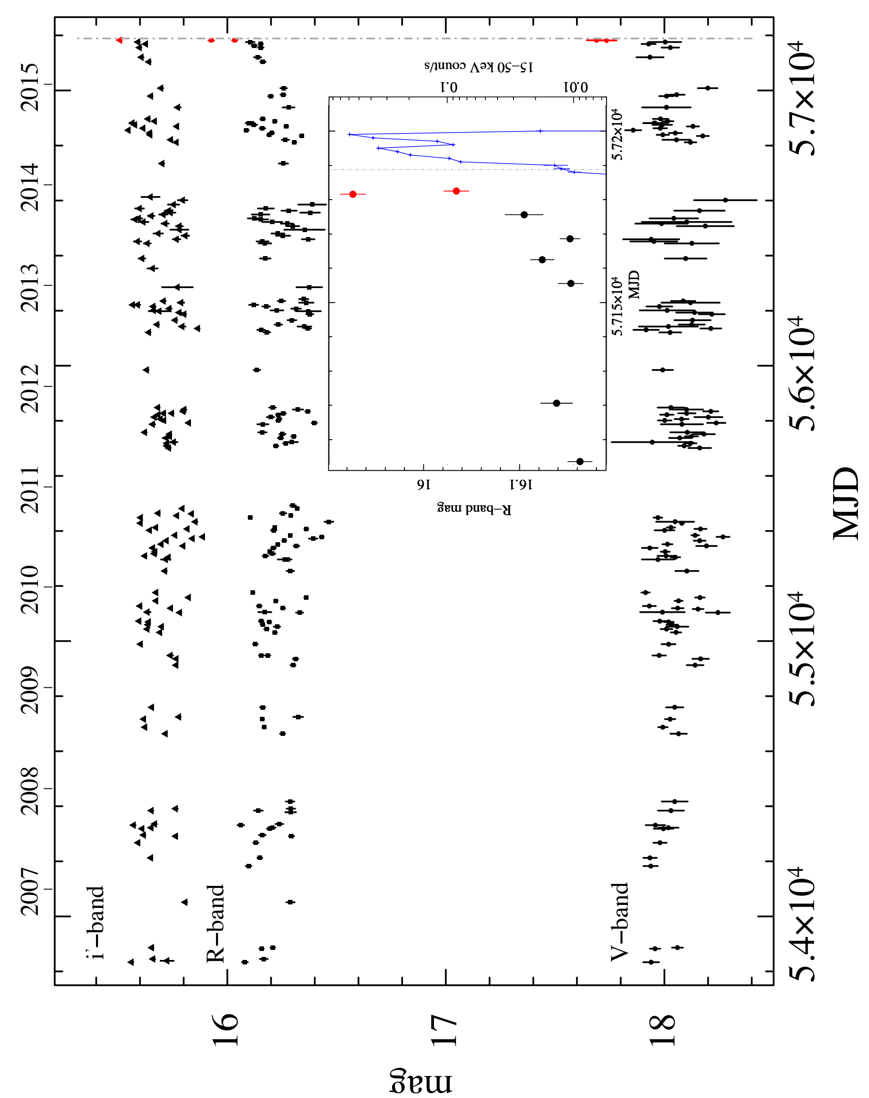

FIGURE 6.1: Optical light curve in i' (triangles), R (squares) and V (circles) bands from 2006 to 2015. Magnitudes include flux from the nearby contaminating star. The dot-dashed line at MJD 57188.772 shows the time of the X-ray trigger with *Swift*-BAT. The red points are 2015 June 8 (MJD 57181.5) and 9 (MJD 57182.5). No observation in i' band was performed on 2015 June 8. *Inset:* a zoom-in of the 2015 R-band data compared with the 3σ BAT detections (blue crosses). Figure kindly provided by Federico Bernardini.

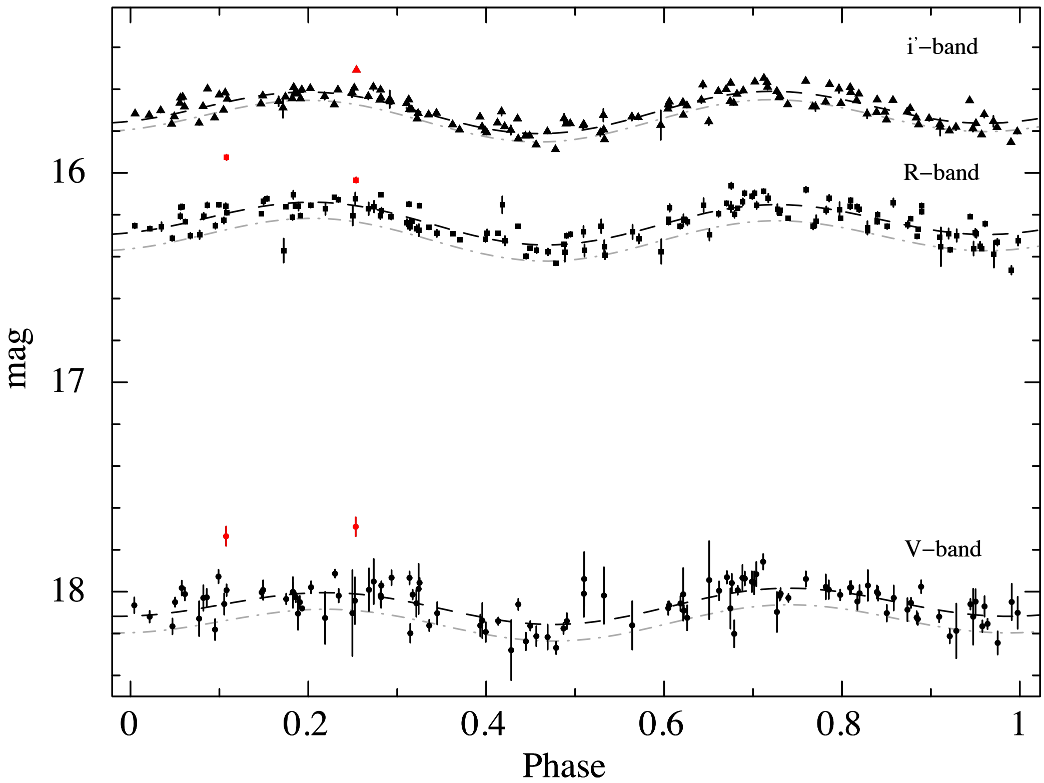

Figure 6.2: Orbital light curves. The dashed line is a constant plus two sines best fitting model. The dot-dashed line is the lower envelope. Colours and symbols are the same as Fig. 6.1. Figure kindly provided by Federico Bernardini.

activity on timescales of longer than timescales of minutes (the time resolution of consecutive exposures). The bottom panel of Fig. 6.3 shows the average of the R and i'-band residuals, $\langle \Delta\, i', \Delta\, R \rangle = 0.5(\langle \Delta\, i' \rangle + \langle \Delta\, R \rangle)$, using three points per bin. The decreasing–increasing trend is now clearer. The first part of the light curve (up to MJD 55834.5) is fit with a constant plus a linear function giving a decrease of ~ 0.02 mag yr^{-1} is measured between MJD 53860 and 55834.5.

The slow rise from MJD 55834.5 culminates in a sudden increase in flux (highlighted by the red points in Fig. 6.3), which is interpreted as an optical precursor to the first X-ray flare registered by *Swift*-BAT. Assuming the rise of the X-ray flare is monotonic, the delay in the rise of the X-ray flux (MJD$\sim$ 57188.5) compared to the optical (MJD$\sim$ 57181.5) is estimated to be at least 7 days. It could be as long as 13 days, considering that the optical flux may have started rising immediately after the pointing before the precursor (MJD$\sim$ 57175.6). The length of this optical–X-ray delay is similar to those seen in a number of other LMXBs which showed this behaviour (Orosz et al., 1997; Shahbaz et al., 1998; Jain et al., 2001; Wren et al., 2001; Uemura et al., 2002; Buxton & Bailyn, 2004; Zurita et al., 2006).

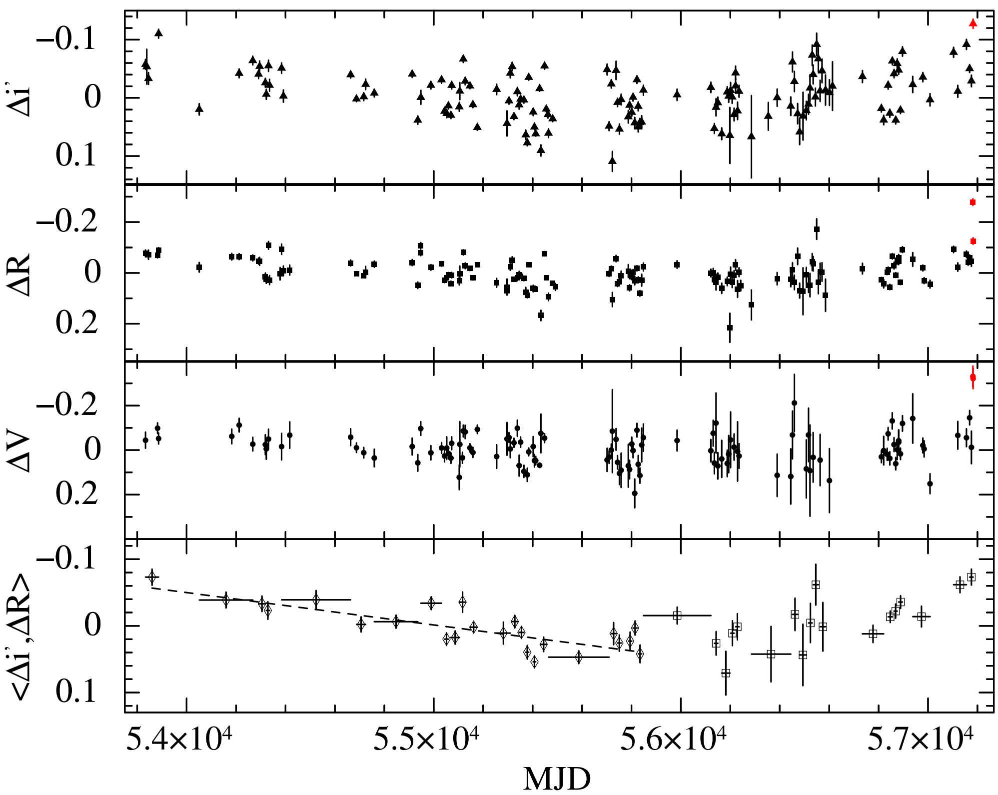

FIGURE 6.3: Residual light curves obtained by subtracting the model shown in Fig. 6.2 from the data in Fig. 6.1. The bottom panel shows the average of the residuals in the i' and R bands. The dashed line is a fit made with a constant plus a linear component. Colours and symbols are the same as in Fig. 6.1. Figure kindly provided by Federico Bernardini.

6.3.2 Optical Spectroscopy

The optical spectrum is presented in Fig. 6.4 and is dominated by a strong H_α emission line. Also present are H_β and multiple He I emission lines. However, He II λ4686, typical of X-ray illuminated discs in outburst, is absent. At first sight, the absorption features of the companion also appear to be absent, but a closer look reveals features hidden within the noise (see Fig. 6.5). A cross-correlation of the pre-outburst spectrum with the spectrum of the radial velocity template HR 8857 yields a peak at 193.7 ± 3.6 km s^{-1} (after correcting for the radial velocity of the template), consistent with that of the donor star at the orbital phase of the WHT spectra. However, it must be noted that the $\sim 7\times$ increase in H_α flux compared with the quiescent level (Casares & Charles, 1992) suggests that the accretion disc is much brighter than in *true* quiescence.

The inner radius of the truncated disc, ($R_{\rm in} = 0.5(c \sin i / v_{\rm in})^2$; Narayan et al., 1996), can be estimated by studying the H_α emission line profile. By measuring the half-width at zero intensity (HWZI), the velocity at the inner edge of the disc, $v_{\rm in}$, can be estimated. I used a non-linear least squares algorithm to fit a low-order polynomial to the continuum (masking H_α) and then subtracted it. I then fit a double Gaussian to the H_α profile,

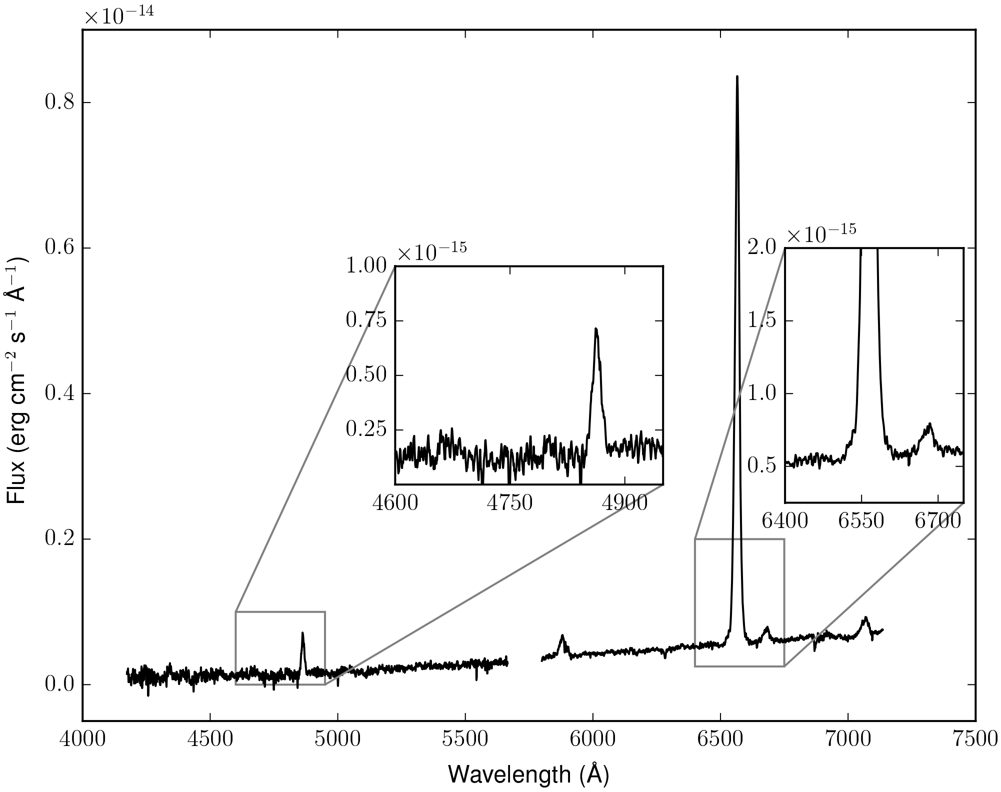

FIGURE 6.4: Averaged optical spectrum (smoothed using a 5-point boxcar algorithm) of V404 obtained with WHT/ISIS on 2015 June 15. The spectrum has been flux calibrated using the flux standard star BD+25 4655. The left and right insets show the zoomed in region around H_β and the base of H_α, respectively.

finding it more accurate than a single Gaussian due to a broader component being present at the base of the line (Fig. 6.4). Utilising the lower amplitude, broader Gaussian, I then estimated the HWZI and hence $v_{\rm in}$ by measuring the 5σ of the Gaussian.

From the fits I find a slightly redshifted H_α peak at 6564.3 ± 0.1 Å . This does not agree with the derived systemic velocity of V404 (-0.4 ± 2.2 km s^{-1} Casares & Charles, 1994) but a redshifted H_α centroid has been measured during the early evolution of the 2015 outburst (Muñoz-Darias et al., 2016). I measure HWZI 54.0 ± 0.5Å from the fits, which translates to $v_{\rm in} = 2468 \pm 23$ km s^{-1}. This is actually a lower limit on $v_{\rm in}$, as higher velocity structure is present around the base of the line profile, though it is difficult to fit. Using the derived inclination of $i = 67°$ (Khargharia et al., 2010), the inner radius is derived to be $R_{\rm in} < 6200 R_{\rm S}$ at MJD 57188.208, where $R_{\rm S}$ is the Schwarzschild radius (see section 1.1.3).

For comparison, using the same methods, the HWZI of the average H_α line profile in quiescence is found to be $\lesssim 1500$ km s^{-1}, implying $R_{\rm in} \gtrsim 17000\ R_{\rm S}$. Therefore, the inner disc radius appears to have decreased by a factor ~ 3 by the time of the 'pre-outburst'

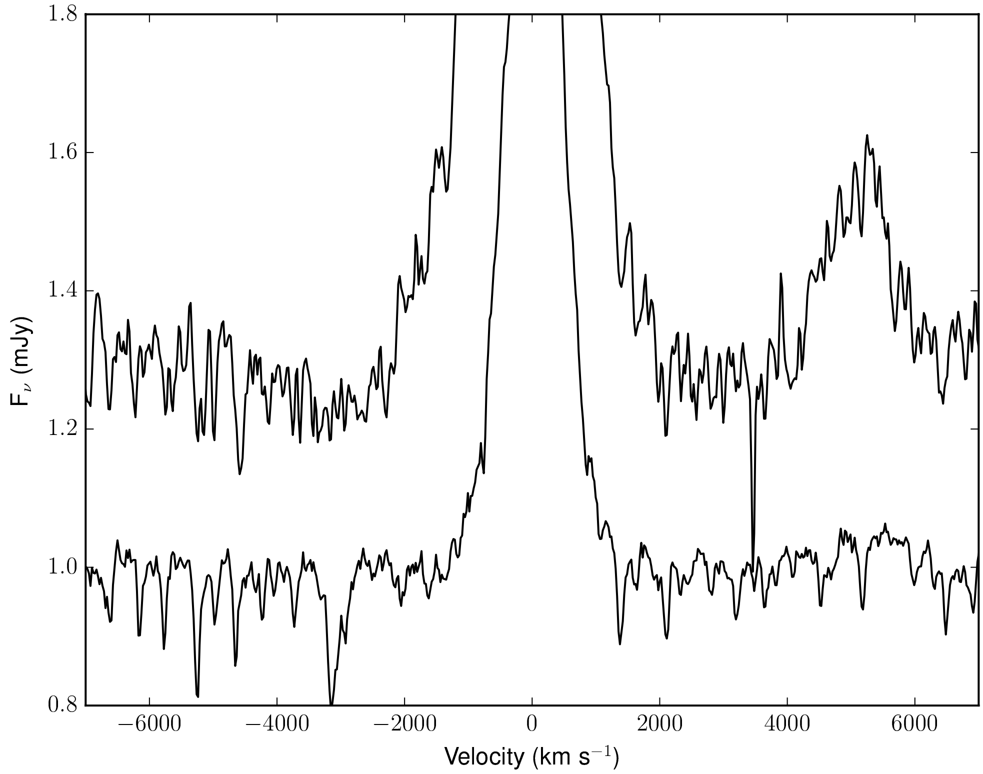

FIGURE 6.5: June 15 pre-outburst spectrum (offset by 0.3 mJy and smoothed with a Gaussian kernel of FWHM = 2 pixels) compared with the 20 year average quiescent spectrum (bottom), zoomed in on the region surrounding H_α. Spectra have been averaged in the rest frame of the companion.

spectroscopic observations with respect to quiescence, indicating that the disc's evolution towards outburst is well underway.

6.3.3 Spectral Energy Distribution (SED)

To construct the SED of the optical precursor, the lower-envelope of the modulation is measured in each filter (see Zurita et al., 2004), which represents the donor contribution at each phase (Fig. 6.2). Subtracting the lower envelope flux from the combined June 8 and 9 images in each band leaves the SED of V404, which is then de-reddened using $A_V = 4$ (Casares et al., 1993; Hynes et al., 2009b) and the extinction law of Cardelli et al. (1989). The spectral index for the optical precursor is measured to be $\alpha = -0.35 \pm 0.32$, where $F_\nu \propto \nu^\alpha$. This is consistent with a 7500 ± 1500 K blackbody which peaks in the visible band. These errors do not take into account any uncertainties in A_V, meaning that the spectral index can be strongly affected by the systematic uncertainties present (Hynes et al., 2009b).

The precursor SED could be consistent, within 1σ confidence level, with both optically thin synchrotron emission with $\alpha \sim 0.7$, or optically thick (flat) synchrotron emission with $\alpha \sim 0$. However, Bernardini et al. (2016) showed that during the 1989 outburst of V404, the jet dominates the optical flux in the hard state, but makes marginal contributions in quiescence.

I also measured a de-reddened spectral index from the pre-outburst spectrum of $\alpha = -1.85 \pm 0.08$ for the continuum, by removing the hydrogen lines from the red arm spectrum. This is similar to the spectral index of some of the flares seen in quiescence (Shahbaz et al., 2003) and some of the fastest flares in the 2016 outburst (Gandhi et al., 2016); this suggests a variable spectrum during the initial rise into outburst.

6.4 Discussion and Conclusions

After an outburst is triggered in a SXT, the inner radius of the thin disc decreases until its minimum value, $R_{\rm min}$ is reached. The time the disc needs to reach $R_{\rm min}$ is a viscous timescale ($t_{\rm vis}$; Dubus et al., 2001). In the context of V404, $t_{\rm vis}$ represents the difference between the time t_V, when the outburst starts at some radius $R(V)$ of the truncated disc and the time t_X, when the inner disc edge reaches $R(X)$, where $R(V) > R(X)$, attaining the temperature that allows emission of X-rays. The delay between the observed X-ray and optical emission (Δt_{V-X}) corresponds to the difference between the two radii.

From Equation (16) of Dubus et al. (2001), $R(V)$ can be estimated as follows:

$$\Delta t_{V-X} = 15.3\ M_{10}^{1/2}\ \alpha_{0.2}^{-1}\ T_5^{-1}\ (R_{10}^{1/2}(V) - R_{10}^{1/2}(X))\ \text{days} \tag{6.1}$$

where $M_{10} = M_{\rm BH}/10\ M_{\odot}$, $\alpha_{0.2} = \alpha/0.2$ is the viscosity parameter, $R_{10} = (R/10^{10}\ \text{cm})$ is the inner disc radius and $T_5 = (T/10^5\ \text{K})$ is the midplane temperature, where $T \gtrsim (3-4) \times 10^4$ K at the start of the outburst (see Lasota et al., 2008). Using $T = (30-50) \times 10^3$ K, $\alpha = 0.1 - 0.2$ and $R(X) = 5 \times 10^8$ cm (Dubus et al., 2001), along with $M_{\rm BH} = 9 M_{\odot}$ as derived by Khargharia et al. (2010), I find that the instability corresponding to the outburst precursor may have been triggered at $R(V) \sim (0.9 - 2.2) \times 10^9$ cm ($\sim 340 - 830\ R_{\rm S}$). Note that this calculation assumes the disc is hot enough to emit X-rays when the inner radius reaches 5×10^8 cm (see Dubus et al., 2001). However, if $R(X)$ is higher, (as I discuss below) then $R(V)$ will be further from the BH.

In section 6.3.2 I also derive a direct constraint on $R(V)$ from the HWZI of the H_α emission line. At MJD 57188.208, 13 hr before the first X-ray detection and ~ 6.5 days after the detection of the optical precursor, $R(V) < 6200\ R_{\rm S}$. This is an upper limit to

$R(X)$, since $R(X) < R(V)$, and so it represents a constraint on the size of the inner edge of the truncated disc ($R_{\rm in}$) close to the onset of the X-ray outburst. If $R(X) = 6200\ R_{\rm S}$, then $R(V)$ is calculated to be $\sim (2.0 - 2.7) \times 10^{10}$ cm ($\sim 7500 - 10000\ R_{\rm S}$). This represents the absolute upper limit that $R(V)$ can have.

All versions of the DIM predict a constantly increasing flux during quiescence (Lasota, 2001), while observed quiescent fluxes of dwarf novae and LMXBs are constant or decreasing (hower, see Wu et al., 2016, for an example of a steady increase). As seen in Fig. 6.3, V404 exhibits a long-term trend in its optical magnitude; a 0.1 mag decrease followed by a 0.1 mag increase over the ~ 10 years of monitoring. The source is known to show year-to-year optical variability of similar amplitude (Zurita et al., 2004). Most of the variability detected above the orbital modulation is likely due to accretion activity and occurs at all orbital phases (Fig. 6.2).

It is known that accretion is happening at a low level in quiescence (short term variability has been seen in X-ray, optical and radio). Small changes in accretion rate from year to year likely explain the long-term optical variations. The rise in optical flux from April 2015 may reflect a recent rise in mass accretion rate $\dot{M}$ eventually culminating in the outburst. The disc becomes progressively hotter as matter builds up and when the temperature reaches the H ionisation level, the inside-out heating wave quickly propagates from the trigger site, close to the inner edge of a truncated disc, through the whole disc (in both directions). Then, the inner edge of the truncated disc moves inwards, on the longer viscous timescale, and a week after the optical precursor, when $R_{\rm in} < 6200\ R_{\rm S}$ (a factor of ~ 3 smaller than in quiescence), it is hot enough to generate X-ray emission and the first X-ray flare is observed.

Chapter 7

On the orbital period of the Galactic transient MAXI J1305-704

"The bowler's Holding, the batsman's Willey."

Brian Johnston (alleged) - Test Match Special

In this chapter I will present work which is ongoing. I present optical and X-ray observations of the SXT MAXI J1305-704, which was discovered in April 2012 but whose system parameters are relatively unknown. I reanalyse data from a 2012 *Suzaku* observation of the source and find evidence for a $\sim$ 5h periodicity in the X-ray light curves. I tentatively associate this with the orbital period of the system, much lower than the previous determination ($P_{\rm orb}$ = 9.74h), which was determined using the same data. I also present optical spectroscopy and attempt to place a lower limit on the mass of the compact object.

All work presented in this chapter is my own.

7.1 Introduction

MAXI J1305-704 is a SXT discovered in April 2012 (Sato et al., 2012) with the Gas Slit Camera of the *Monitor of All-Sky X-ray Image* (*MAXI*/GSC; Matsuoka et al. 2009) on board the International Space Station. Optical follow up revealed a new source not present in archival DSS images, suggesting the source was a new SXT (Greiner et al., 2012) and optical spectroscopy with the Southern African Large Telescope (SALT; Buckley et al., 2006) revealed spectral features also typical of a LMXB (Charles et al., 2012). Pointed observations of the source with *Swift* reported a soft, disc-dominated spectrum, suggesting that MAXI J1305-704 was a new BH candidate (Kennea et al., 2012a). MAXI J1305-704 represents another high-latitude ($b \sim -8°$) SXT, joining an increasing population of such sources, all of which appear to have short periods ($P_{\rm orb} \lesssim 5$ h; Table 2.1 in chapter 2). This raises questions about the formation scenario of this particular subclass of LMXBs.

The $P_{\rm orb}$ of MAXI J1305-704 has been subject to much debate. *Swift* observations of the source during its initial outburst revealed dips in the X-ray light curves accompanied by spectral hardening. The dips occurred at irregular times and made determining the exact periodicity difficult, but $P_{\rm orb}$ has been suggested to be 1.5h and 2.7h (Kennea et al., 2012b). Subsequently, Shidatsu et al. (2013) reported $P_{\rm orb} = 9.74 \pm 0.04$h based on the discovery of deep dips in *Suzaku* light curves. However, there was no significant timing analysis (e.g. periodograms) to support this. The discovery of dips in multiple X-ray observations indicate that MAXI J1305-704 has a high inclination angle and hence is an important system for study, but as yet detailed constraints on the inclination have not been obtained.

7.2 Observations & Analysis

7.2.1 X-ray observations

I used archival *Suzaku* observations of MAXI J1305-704 from 2012 July 20 18:10:29 UT to 22 00:30:23 for a net on-source time of ∼40ks (OBSID: 907001010). *Suzaku* consists of the X-ray Imaging Spectrometer (XIS), an X-ray CCD camera operating over an energy range of 0.2-12keV, and the Hard X-ray Detector (HXD), a non-imaging instrument with an energy range 10-600keV. For the purposes of this study I used the XIS chips only, in order to compare with the analysis of Shidatsu et al. (2013). The observation took place whilst the source was in the hard state, displaying an average count rate of ≈ 5 cts s^{-1} so pileup effects are negligible and can be ignored.

I reduced the cleaned event data for all three operational XIS chips with HEASOFT version 6.16. Emulating the analysis performed by Shidatsu et al. (2013), a circular region with a radius of $1.9'$ was used to extract events from the source position, whilst a circular region with the same radius in a source-free area was used to extract the background. The HEASOFT task XSELECT was used to extract and bin source and background light curves in the 0.7-2 keV and 2-10 keV energy bands. Subtraction of the background light curve was performed by the task LCMATH.

7.2.2 Optical observations

MAXI J1305-704 was also observed on the nights of 2012 April 15–16 with the Robert Stobie Spectrograph (RSS) on SALT at the SAAO, obtaining 2.25 hours of continuous spectroscopy on each night. The G2300 VPH grating was used with individual integration times of 600s. A slit width of 0.6″ was used, covering the wavelength range $\lambda 4040 - 5110$Åwith a resolution of 105 km s^{-1} (FWHM). Arc lamp exposures for wavelength calibration were obtained before and after each science exposure.

Primary reduction of the data (gain correction, cross-talk correction, etc.) was done with the SALT science pipeline (Crawford et al., 2010). IRAF (Tody, 1986) was then used to perform further standard reduction techniques to achieve wavelength calibration, cosmic ray removal using the external task "lacos" (van Dokkum, 2001), and extraction of the 1-dimensional spectra. CuAr comparison arcs were obtained to calibrate the wavelength scale, achieving a central dispersion of 0.17 Å pixel^{-1} and spectral resolution of 1 Å (FWHM).

To fit the emission line profiles in the averaged spectrum I used a PYTHON based non-linear least squares algorithm to fit a double Gaussian to the double-peaked Balmer emission and a triple Gaussian to the region containing the Bowen blend and the double peaked He II λ4686. In order to study the motion of the He II peaks, the same fitting approach as above was applied to each individual spectrum, however the peak-to-peak separation and width of each Gaussian were fixed to the values obtained from the fit to the average spectrum.

7.2.3 X-ray Light Curves

The 128s binned *Suzaku* light curves are presented in Fig. 7.1 along with the hardness ratio light curve. I chose to plot the XIS-3 data as there were more data points available from this chip, however the light curves from the XIS-0 and XIS-1 chips are almost identical. The light curves exhibit significant variability in both bands, with deep dips appearing at irregular intervals accompanied by notable increases in the hardness ratio.

It is difficult to estimate the periodicity of the dips by eye due to gaps in the data, which are mostly due to the low-Earth orbit of the spacecraft. I therefore determined the periods and errors by performing a Lomb-Scargle analysis on both the light curves and the HR to determine a central peak frequency and then performing a Monte-Carlo

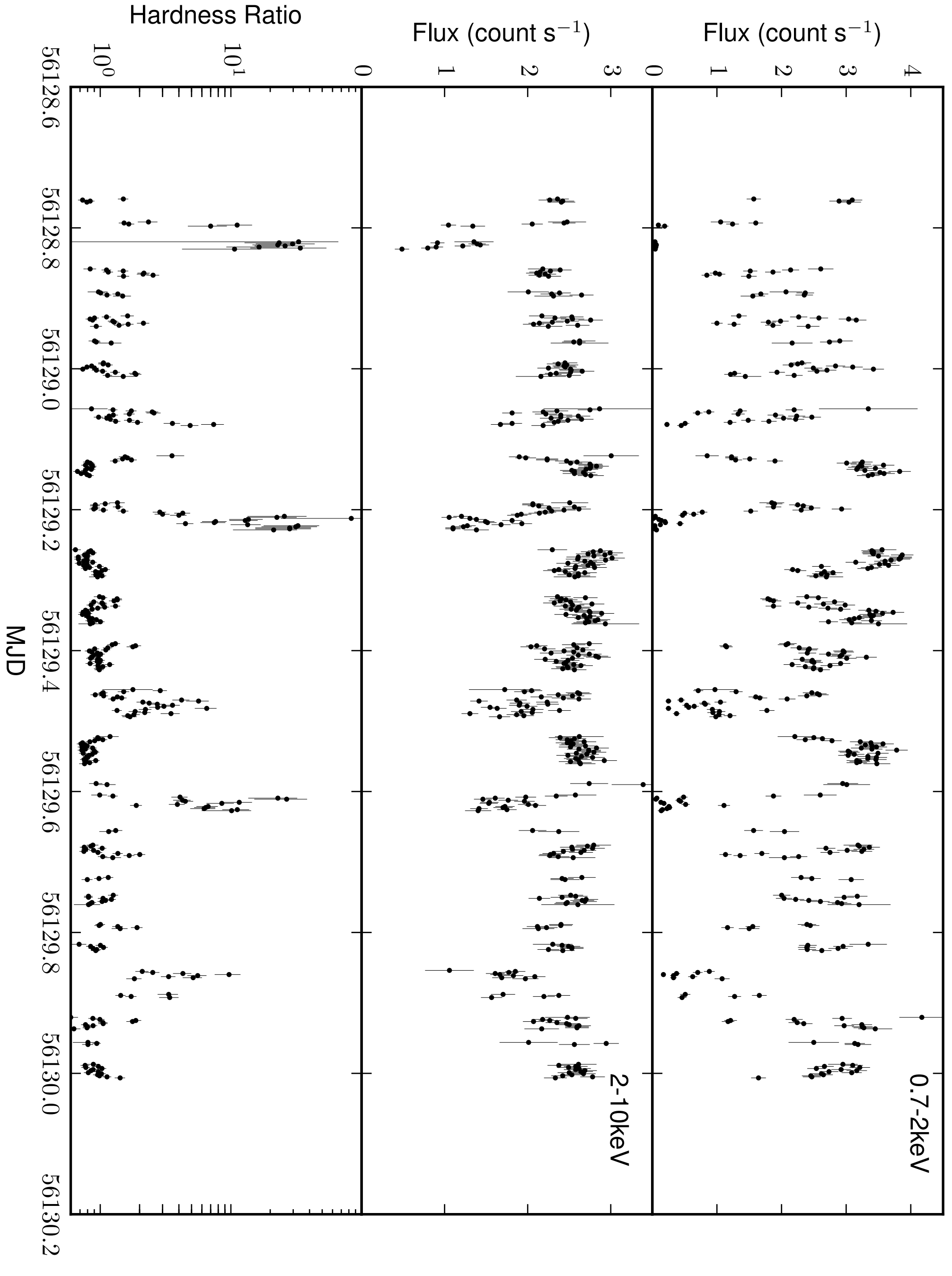

FIGURE 7.1: *Suzaku* XIS-3 light curves in 128s time bins. Plotted are the 0.7-2keV (S; Top) and 2-10keV (H; Centre) energy bands and the hardness ratio, defined as H/S (Bottom).

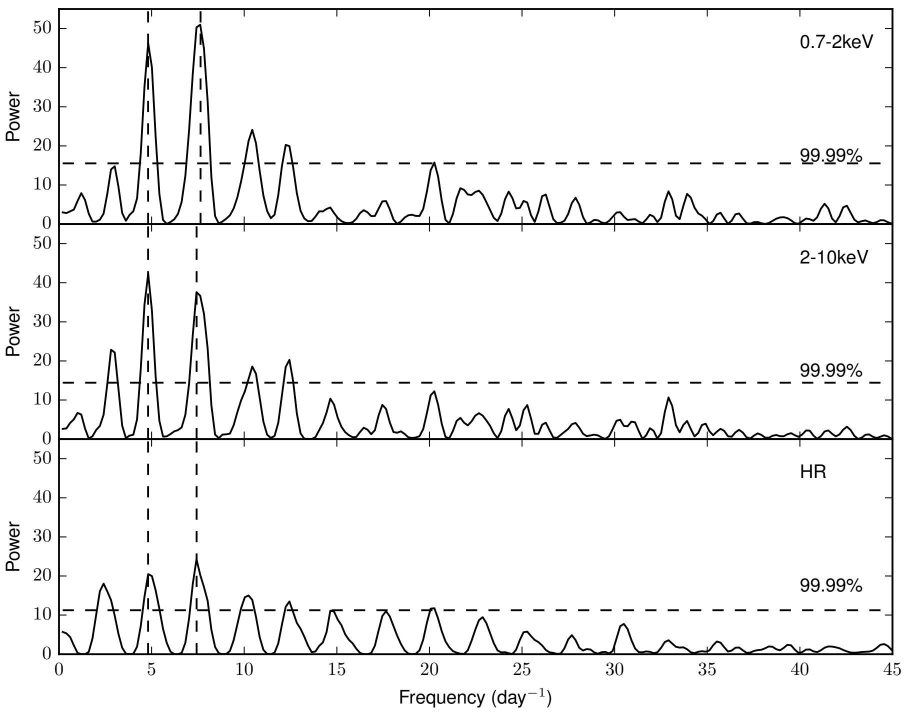

FIGURE 7.2: Lomb-Scargle periodograms of the *Suzaku* light curves in the 0.7-2keV (Top) and 2-10keV (Centre) energy bands and of the HR (Bottom). The two most significant periodicities seen in the periodograms are marked in each panel with vertical dashed lines. The horizontal dashed lines in each panel represent the 99.99% significance level.

simulation based on 'bootstrap-with-replacement' (see chapter 2). The distribution of peak frequencies resulting from 10000 iterations of this process is used to determine the error on the peak frequency. The periodograms are presented in Fig 7.2 and exhibit a number of periodicities, making it difficult to determine the true $P_{\rm orb}$. The most significant peaks correspond to periods of 3.14 ± 0.06h (3.23 ± 0.05h) and 4.98 ± 0.05h (4.99 ± 0.04h) in the 0.7-2keV (2-10keV) energy band, but there is also a large amount of power at 2.30 and 1.93h. Similar periodicities are also seen in the HR periodogram but at lower power. The measured periodicities for each peak are consistent (within errors) between bands and the HR.

The significance of the peaks was tested by applying a randomisation algorithm to the data. The flux positions within the light curves were randomised, but the points retained the time stamps and sampling pattern, and a Lomb-Scargle analysis was then performed on the randomised data. Multiple iterations of this algorithm allowed me to determine the 99.99% confidence limits for the periodograms. In 99.99% of 100000 runs, the highest power recorded for both energy bands was $\lessapprox 15.5$ and $\lessapprox 11.24$ for

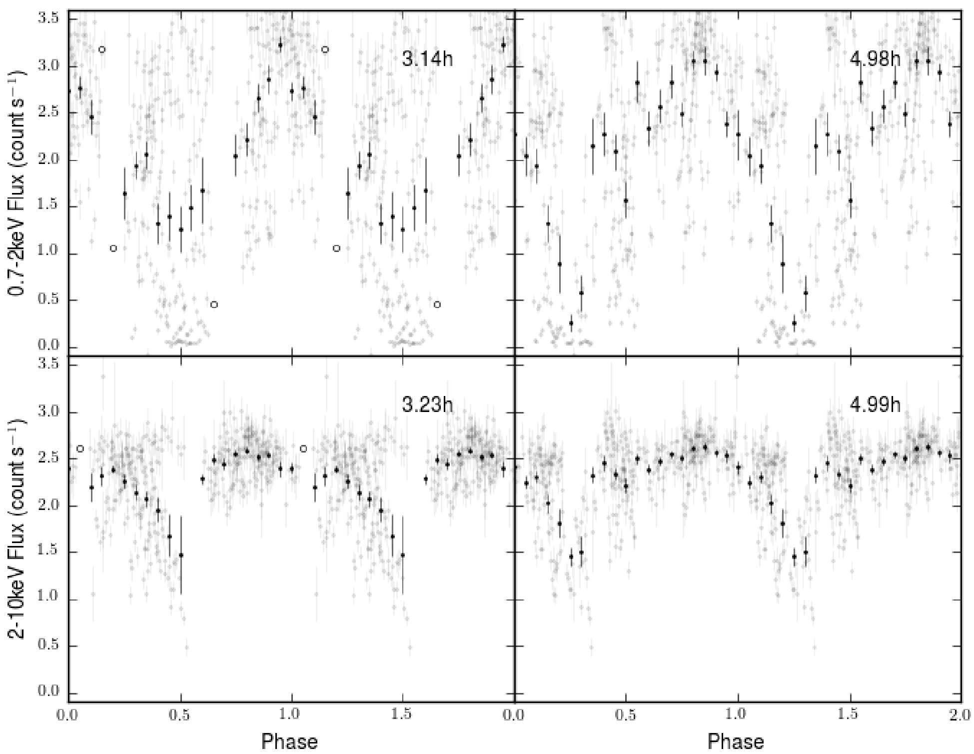

FIGURE 7.3: Suzaku light curves of MAXI J1305-704, folded on the two most significant periods (from the periodograms in Fig. 7.2). The top two panels are folds of the 0.7-2keV light curves and the bottom two panels are folds of the 2-10keV light curves. Open points represent data which have no estimated uncertainties due to only one unbinned point being available for binning. Also shown in light grey are the unbinned phase-folded light curves in each energy band. The periods used for folding are designated in each panel.

the HR periodogram. It is therefore obvious that the two most significant peaks (at $P = 3.14/3.23$ and 4.98/4.99h) are extremely unlikely to have occurred by chance.

I folded the *Suzaku* light curves on the two most significant peaks present in Fig. 7.2 and the results are shown in Fig. 7.3. When the light curves are folded on the central peak (3.14h and 3.23h in the 0.7-2keV and 2-10keV bands, respectively), the sharp nature of the dips is not revealed in the 0.7-2keV band, instead exhibiting more of a sinusoidal morphology. However the dipping structure appears to be present in the 2-10keV folded light curves, though with large uncertainties. The dipping structure is evident in both bands of the $\sim$ 5h folded light curves, with a deep dip occurring at phase 0.25, followed almost immediately by a shallower dip at phase 0.5. The folded light curves are explored further in Section 7.3.1.

Line (Å)	λ_C (Å)	Separation (km s^{-1})
He II 4686	4685.4±0.6	960±44
H_β 4861.3	4860.7±0.6	783±37
H_γ 4340.5	4338.9±0.9	952±88

TABLE 7.1: Results of double Gaussian fits to the observed emission lines in the averaged spectrum of MAXI J1305-704. Tabulated here are the position of the centroid (λ_C) and the separation of the peaks.

7.2.4 Optical Spectroscopy

The averaged optical spectrum of MAXI J1305-704 is presented in Fig. 7.4. As was already reported by Charles et al. (2012), the spectrum exhibits strong double-peaked Balmer emission (H_β, H_γ and H_δ) and He II, indicative of a high inclination binary. Also evident is strong emission in the Bowen region ($\lambda 4640 - 4660$), a blend of narrow, high-excitation NIII and CIII emission lines arising from the irradiated surface of the donor star. Furthermore I note an absorption feature just redward of H_β, something that has been observed in several other LMXBs including GR Mus (Barnes et al., 2007) and X 1822-371 (Casares et al., 2003).

I also present a close-up of the Bowen/He II region for each individual night in Fig. 7.5, with the spectra being normalised in this instance. It is immediately clear that these lines are extremely broad and are in fact blended together, making any estimation of the emission line properties (e.g. equivalent width and FWHM) highly uncertain, and is therefore not attempted. He II appears to show large variability in the double-peaked line profiles from night to night and during the night. On the first night (Apr 15) the blue wing appears to dominate, whilst on night two (Apr 16) the two wings appear comparable. This could perhaps indicate that at least some of the He II emission could originate either on the X-ray heated face of the secondary star or the stream/disc impact region (i.e. the hotspot). Finally I note the absence of narrow emission components in the Bowen blend. During the second night there might be some structure present close to 4640 Å, but the low S/N of the spectra does not allow us to unambiguously conclude this.

In order to study the emission lines further I fitted a double Gaussian to the Balmer emission and a triple Gaussian to the Bowen/He II emission. The results of the fits to the average spectrum are presented in Table 7.1 (I did not include H_δ due to its poorer S/N).

I can also fit the He II line profiles in the individual spectra and study the motion of the line centroid about its rest wavelength ($\lambda_0 = 4686$Å). I applied the same fitting routine as with the averaged spectrum, however, using the fit parameters from Table 7.1, I kept

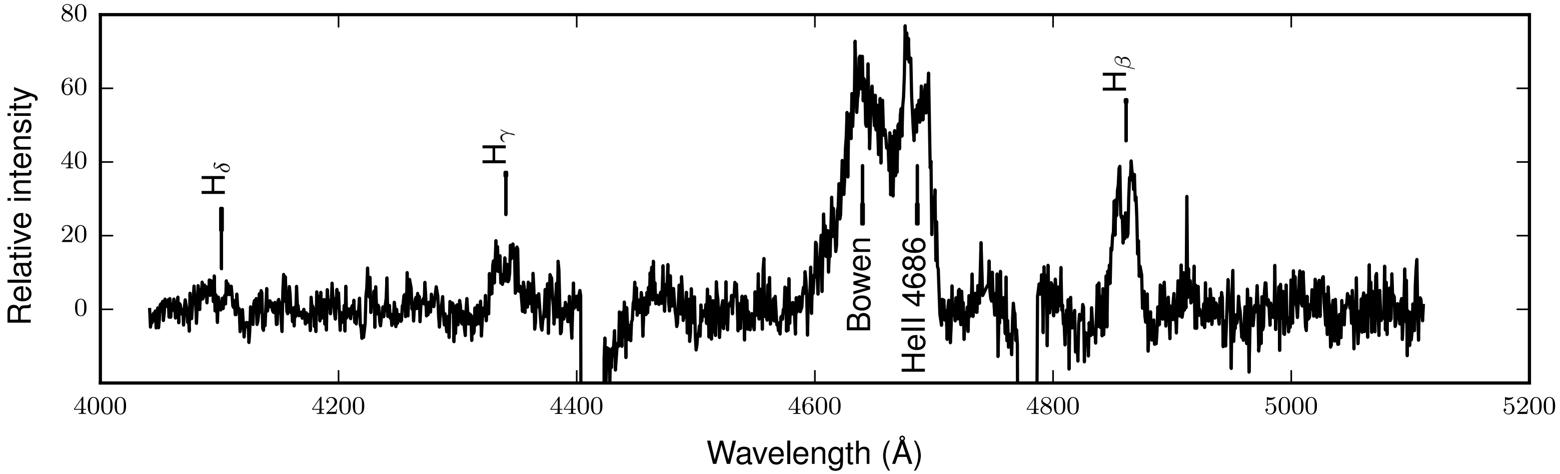

FIGURE 7.4: Averaged optical spectrum of MAXI J1305-704 obtained with SALT on the nights of 2012 April 15 - 16. The spectrum has been continuum subtracted and notable features have been annotated.

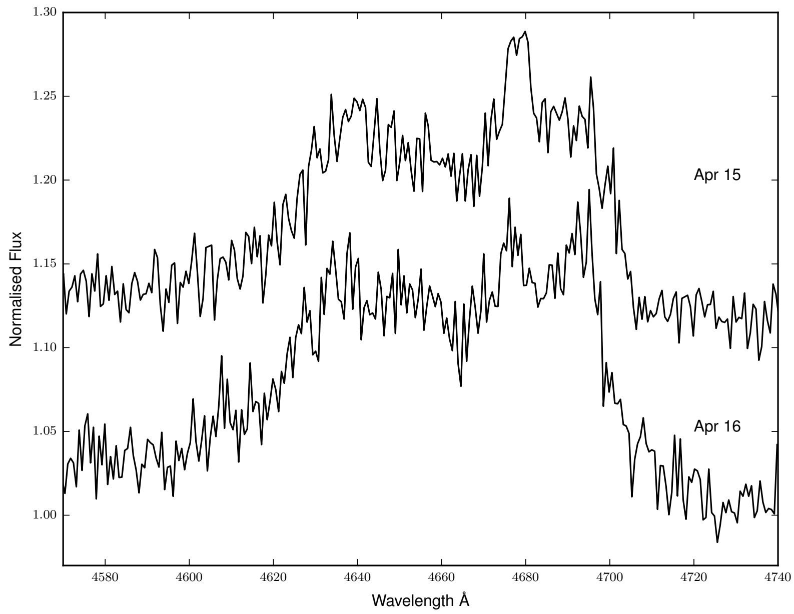

FIGURE 7.5: Close up of the normalised average He II $\lambda4686$ region for MAXI J1305-704 for each individual night, showing the night to night variability in the He II profile. The two nights have been offset by 0.1 for clarity.

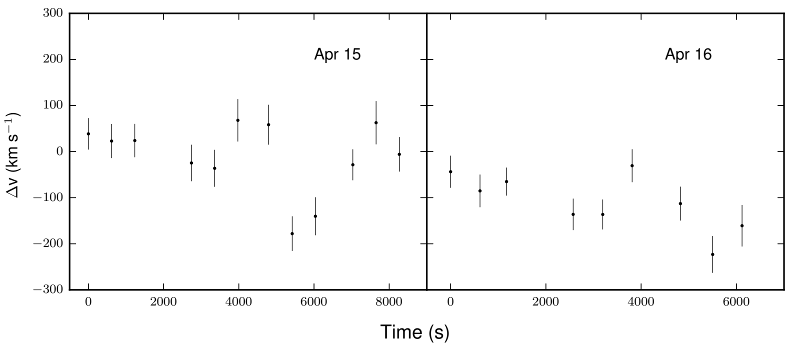

FIGURE 7.6: The radial velocity of the centroid of the double peaked He II emission line over the course of the two nights of SALT spectroscopy. On Apr 15 time T=0 is at MJD=56032.86548611 and on Apr 16 T=0 is at MJD=56033.86768519.

the peak separation and width (σ) of the individual Gaussian components constant. Fig. 7.6 shows that there is no intrinsic motion of the He II line about its rest wavelength, a result to be expected from a candidate BH system, as the motion of the compact object due to the low-mass companion is negligible (typically $\ll$50km s^{-1}).

7.3 Discussion

7.3.1 The Orbital Period

To investigate the multiple periodicities present in the periodograms in Fig. 7.2 I must study the light curves folded on these periods. The phase-folded X-ray light curves in Fig. 7.3 display differing morphology dependent on the period used in the folding. The dipping structure is seen in Fig. 7.1 recovered in both bands of the $\sim$ 5h folded light curves. Deep dips are seen in the 0.7-2keV band, whilst shallower dips appear in the 2-10keV folded light curve, echoing the apparent dichotomy in dipping structure in the two energy bands as seen in Fig. 7.1.

When folded on the other major peak in Fig. 7.2 (3.14/3.23h), the dipping structure is not at all clear in the 0.7-2keV band, though it is visible in the 2-10keV energy band. There are also empty bins in the folded data on these periods. It is possible that the $\sim$3.2h period can be attributed to double the $P_{\rm orb}$ (1.6h; Mitsuda et al. 2007) of the *Suzaku* spacecraft. There are no peaks in the periodogram at 1.6h, but this could be due to an irregular observing pattern of the source over the total $\sim$30.5h observation. The fact that the dipping structure is only revealed in both bands of the 4.98/4.99h folds of the *Suzaku* light curves implies that this is likely the true $P_{\rm orb}$ of MAXI J1305-704.

7.3.2 System Parameters

As well as determining $P_{\rm orb}$ from the *Suzaku* light curves, I can use the optical spectra to determine a number of other system parameters. The most uncertain of these is an estimate for the radial velocity semi-amplitude of the secondary (K_2). One way to estimate K_2 is via the projected velocity of the outer accretion disc v_D, with half the peak-to-peak separation of the H_α often used as an indicator (Warner, 1995). Orosz et al. (1994) and Orosz & Bailyn (1995) showed that there is a relation ($v_D/K_2 = 1.1$ - 1.25) between this velocity and K_2 for quiescent SXTs. Furthermore, this relation provides a lower limit for K_2 for SXTs in outburst, as the accretion disc expands to a radius larger than that in quiescence, therefore v_D is smaller in outburst. Although I do not have an estimate for v_D from H_α, observations of GRO J0422+32 (Casares et al., 1995) and MAXI J1659-152 (Kaur et al., 2012) have shown that it is very similar to the peak-to-peak separation of H_β. Therefore using the peak-to-peak separation of H_β = 783$\pm$37 km s^{-1}, I derive an absolute lower limit of $K_2 \geq 313$ km s^{-1}.

Combining the preferred $P_{\rm orb}$ with the conservative lower limit on K_2 obtained from the double peak separation, I derive an absolute lower limit on the mass function for MAXI

J1305-704 of $f(M_1) = M_1 \sin^3 i/(1+q)^2 = K_2^3 P_{\rm orb}/2\pi G \geq 0.66 M_\odot$, where M_1 is the mass of the compact object, i is the inclination and q is the mass ratio M_2/M_1, where M_2 is the mass of the companion. Since both $\sin i$ and q must be positive, the mass function truly provides an absolute lower limit on the mass of the compact object in MAXI J1305-704. However, this mass function is well below $1.4 M_\odot$, the canonical value for the mass of a neutron star, and therefore does not allow as yet a determination of the true nature of the compact object.

7.4 Conclusions and Future Work

Using archival *Suzaku* data I have determined $P_{\rm orb}$ of the SXT MAXI J1305-704 to be 4.98±0.05h based on the presence of deep dips in both the 128s binned and folded *Suzaku* light curves. Though this is the preferred period, I cannot completely rule out other periods suggested by the Lomb-Scargle periodogram analysis. I also placed a lower limit on the mass of the compact object $M_1 \geq 0.66 M_\odot$, however this does not yet constrain the nature of the compact object.

The work in the chapter is ongoing. In order to complete this study I need to perform Doppler Tomography on the individual spectra, with the intention of ruling out the other periodicities seen in Fig. 7.2. Doppler Tomography will also allow me to search for a signature of the irradiated face of the donor, providing a better estimate of K_2. To truly determine the compact object mass, I need to obtain spectroscopy of the source in quiescence in order to detect the orbital motion of the companion. However, the source was not detected in the Digitised Sky Survey, and hence is very faint in quiescence. Therefore, detection of the donor may require the next generation of optical telescopes such as the European Extremely Large Telescope (E-ELT).

Chapter 8

Conclusions & Future Work

"Workers of the earth! I bring... good tidings of peanuts! And beer!"

Ford Prefect - The Hitchhiker's Guide to the Galaxy

In this chapter I will summarise my work and identify key areas where my results can be used as the basis for future projects.

In chapter 2, I presented evidence for a precessing accretion disc in the candidate BHXRT Swift J1753.5-0127. This precession manifested as a long term, super-orbital periodicity of $\sim$ 420 days present in both X-ray and optical light curves of Swift J1753.5-0127. I interpreted this precession as being due to a large difference between the mass of the compact object and the donor. If this is indeed the case then the companion must be highly evolved, possibly a brown dwarf. I also reported on the discovery of two hard X-ray dips in the *Swift*-BAT light curves, with a related weak feature in the lower energy MAXI light curves. These dips are separated by the super-orbital periodicity and have recently been attributed to failed transitions to an intermediate state (Soleri et al., 2013; Yoshikawa et al., 2015). I note that the dips appeared to be periodic at first glance, but an extended observation campaign around the time of the next predicted dip did not reveal any evidence for another state change.

In chapter 3, I showed that Swift J1753.5-0127 finally entered a soft accretion state, after spending > 10 years existing in a hard state, aside from the brief excursions to an intermediate state as discussed above. It was found to be at one of the lowest luminosities (in terms of Eddington fraction) seen in soft state sources, at 0.72% L_{Edd}. The X-ray spectrum was well constrained with a multi-temperature disc with kT_{in} = 0.252 keV which is scattered into a steep power law ($\Gamma = 6.39$), plus an additional, hard ($\Gamma = 1.79$) power law tail. I investigate the possibility of a reflection component but find no evidence for Fe emission at 6.4 keV (a 90% confidence upper limit equivalent width of < 40 eV), nor for a reflection component in the best fit model. I also find that the inner disc edge has moved closer to the BH compared to previous studies, consistent with the dominance of a disc component in the X-ray spectrum.

Chapter 4 introduces radio observations of Swift J1753.5-0127 during the soft state, as well as reporting on continuous radio monitoring of the source with AMI-LA. I study the X-ray/radio correlation and report the first deep limits on the soft state radio flux of a source with a known hard state radio flux. The source's soft state radio flux was found to be significantly less (3σ) than 21μJy, the deepest radio quenching of a transient BH XRB (a factor of $\gtrsim 25$). The power law relationship of the X-ray/radio correlation scales as $\zeta = 0.96 \pm 0.06$, i.e. slightly closer to what has been considered for radiatively inefficient accretion disks. The quenching of the jet at such a low luminosity (0.72% $L_{\rm Edd}$) suggests that the mechanism behind the cessation of jet production is not linked to accretion rate.

Chapter 5 focusses on optical spectroscopy of Swift J1753.5-0127, in particular the apparent evidence of spectral features associated with the donor star reported by Neustroev et al. (2014). These features led to claims of a low-mass ($< 5M_{\odot}$) BH in the system. I present higher resolution spectroscopy of Swift J1753.5-0127 in response to these claims and find that there is no evidence for such features. Instead I find evidence, based on measurements of the H_{α} emission line, that the BH is much more massive ($> 7.4 \pm 1.2M_{\odot}$), noting that this is a conservative lower limit so in reality the actual mass of the BH is likely to be higher.

Chapter 6 discusses the 2015 outburst of V404 Cyg in the context of the Disc Instability Model. Combining my pre-outburst optical spectrum with long-term photometric monitoring, it was concluded that the outburst started from a thermal-viscous instability near the inner edge of a truncated accretion disc. The resultant heating wave propagated through the disc in both directions, whilst the innermost, empty regions of the disc refilled on the viscous timescale. This refilling manifested as a 7 day delay between a precursor optical rise seen in the long-term optical light curves and the triggering of the X-ray outburst, which happened when the inner edge of the disc reached $R_{\rm in} < 6200\ R_{\rm S}$ (a factor of ~ 3 smaller than in quiescence).

Finally, in Chapter 7 I presented my attempt to measure the orbital period of the SXT MAXI J1305-704. I utilised archival data from the long *Suzaku* observation of the source in 2012 and applied timing techniques to measure the periodicities present in the X-ray light curve. I find that the most sensible periodicity, and likely $P_{\rm orb}$ of the system, is 4.98 ± 0.05h due to the presence of X-ray dips in both the raw light curves and the light curves folded on this period. This measurement represents the first estimate of $P_{\rm orb}$ supported by timing analysis. I also estimate the mass function by measuring the lines in the optical spectrum of MAXI J1305-704 and find the mass of the compact object $M_X > 0.66 M_{\odot}$. This unfortunately does not constrain the nature of the compact object.

8.1 Future Work

With such unusual properties, it is hardly a surprise that there is still a lot of work to be done before we fully understand Swift J1753.5-0127. The source was discovered as a transient > 11 years ago and is yet to return to quiescence, for reasons which are not yet understood. If the source does decay into quiescence, it will be possible to gain an accurate estimate of the mass of the compact object, finally allowing its formal identification as a BH. However, this may be difficult, as the source does not appear on the Digitised Sky Survey (DSS), which has a limiting magnitude of ~ 21 in the R-band. Detecting the companion may require the future generation of large telescopes currently in production. The European Extremely Large Telescope (E-ELT), for example, will have a limiting magnitude of ~ 29 in the K-band,[1] ideal for infra-red studies of the donor, should it be much fainter than the limiting magnitude of the DSS. Such telescopes will be required to measure the true orbital period via the ellipsoidal modulation, as well as detect features associated with the companion, enabling an identication of its spectral type and the mass of the compact object.

Another major unknown about the system parameters is the true distance to the source. Cosmic distances are difficult to measure without a standard (or standardisable) candle (e.g Type Ia Supernovae; Perlmutter et al., 1997; Riess et al., 1998). However, distances can be measured to Galactic sources using the method of parallax. Parallax measures the apparent change in position of a nearby source as the Earth orbits the Sun. The angle subtended by the source as it it viewed from different points in the Earth's orbit can be used to calculate the distance to the source. This angle is very small, (a shift of $1''$ for a distance of 1 pc) so can only be accurately measured for nearby sources (see e.g. the Gaia mission; Jordan, 2008). Recently, with the advent of large baseline radio interferometry networks, it became possible to accurately determine the position of sources with radio telescopes, opening up the possibility of performing radio parallax measurements of XRBs which show persistent radio activity.

Using astrometric Very Long Baseline Interferometry (VLBI) observations, Miller-Jones et al. (2009) measured the parallax to V404 Cyg, finding a distance of 2.39 ± 0.14 kpc. This corresponds to the first ever accurate determination of the distance to a BH and the method has since been applied to Cyg X-1 ($1.86^{+0.12}_{-0.11}$ kpc; Reid et al., 2011) and GRS 1915+105 ($8.6^{+2.0}_{-1.6}$ kpc; Reid et al., 2014). It is the success of this technique that

[1] https://www.eso.org/sci/facilities/eelt/science/doc/drm_report.pdf

has led to the submission and subsequent acceptance of a Very Long Baseline Array (VLBA) proposal to observe Swift J1753.5-0127. Collaborators and I intend to measure the parallax of Swift J1753.5-0127 in order to accurately determine the distance, which is currently only estimated from modelling of the UV spectrum (Froning et al., 2014). A well constrained distance measurement will allow us to accurately quantify the true luminosity of the soft state (chapter 3) as well as anchor the source on the radio/X-ray luminosity plane (chapter 4). Not only will we be able to answer the questions pertaining to the work in this thesis, but we will also be able to constrain the natal kick which the system received when the BH was formed in a supernova. The kick velocity can be determined by measuring the three-dimensional space velocity of the system and can also constrain the formation scenario of the system.

In chapter 6, I reported on the discovery of an optical precursor to the X-ray outburst of V404 Cyg. Such a discovery highlights the importance of long-term observations of quiescent XRBs, as we were able to constrain the events that led up to the outburst in June 2015. The optical precursor was only discovered after re-examining data once the source had outburst, and the accompanying optical spectrum, taken 13 hours before the outburst, was obtained by pure chance on an observing run whose main focus was Swift J1753.5-0127. To uncover similar results, sophisticated pipeline software needs to be developed which will automatically detect an optical rise like the one seen in V404. This requires regular monitoring of known LMXBs, which is already ongoing with the Faulkes Telescope Project (Lewis et al., 2008). An optical rise, defined as a significant increase in flux above the normal quiescent level of a source will allow us to trigger optical spectroscopy as well as pointed multi-wavelength observations in order to pre-empt an X-ray outburst. This will provide more data for testing outburst scenarios such as the DIM and enable us to build up a complete picture of the pre-outburst state of LMXBs.

Finally, to truly determine the mass of the compact object in MAXI J1305-704 I need to observe the source in quiescence. This will enable me to measure the orbital velocity of the companion and hence measure K_2 and $v_{\rm rot}$. This will also enable me to confirm $P_{\rm orb}$ by observing the ellipsoidal modulation (as well as measuring $P_{\rm orb}$ independently from optical spectroscopy) and place the tightest constraints on the mass of the system. Attempting this may require the next generation of telescopes, as the source is very faint in quiescence, with no optical counterpart visible in the DSS.

Bibliography

Abbott B. P., et al., 2016, Physical Review Letters, 116, 061102

Antoniadis J., et al., 2013, Science, 340, 448

Arnaud K. A., 1996, in Jacoby G. H., Barnes J., eds, Astronomical Society of the Pacific Conference Series Vol. 101, Astronomical Data Analysis Software and Systems V. p. 17

Bailyn C. D., Jain R. K., Coppi P., Orosz J. A., 1998, ApJ, 499, 367

Balbus S. A., Hawley J. F., 1991, ApJ, 376, 214

Balbus S. A., Hawley J. F., 1998, Rev. Mod. Phys., 70, 1

Bardeen J. M., Petterson J. A., 1975, ApJ, 195, L65

Barentsen G., et al., 2014, MNRAS, 444, 3230

Barnes A. D., Casares J., Cornelisse R., Charles P. A., Steeghs D., Hynes R. I., O'Brien K., 2007, MNRAS, 380, 1182

Barthelmy S. D., et al., 2005, Space Sci. Rev., 120, 143

Barthelmy S. D., D'Elia V., Izzo L., Kennea J. A., Lien A. Y., Markwardt C. B., Page K. L., Siegel M. H., 2015, GRB Coordinates Network, 18785

Belczynski K., Wiktorowicz G., Fryer C. L., Holz D. E., Kalogera V., 2012, ApJ, 757, 91

Belloni T., Homan J., Motta S., Ratti E., Méndez M., 2007, MNRAS, 379, 247

Bernardini F., Cackett E. M., 2014, MNRAS, 439, 2771

Bernardini F., Russell D. M., Lewis F., 2015, The Astronomer's Telegram, 7761

Bernardini F., Russell D. M., Koljonen K. I. I., Stella L., Hynes R. I., Corbel S., 2016, preprint, (arXiv:1604.08022)

Bildsten L., Chakrabarty D., 2001, ApJ, 557, 292

Blandford R. D., Payne D. G., 1982, MNRAS, 199, 883

Boella G., Butler R. C., Perola G. C., Piro L., Scarsi L., Bleeker J. A. M., 1997, A&AS, 122

Bondi H., Hoyle F., 1944, MNRAS, 104, 273

Buckley D. A. H., Charles P. A., Nordsieck K. H., O'Donoghue D., 2006, in Whitelock P., Dennefeld M., Leibundgut B., eds, IAU Symposium Vol. 232, The Scientific Requirements for Extremely Large Telescopes. pp 1–12, doi:10.1017/S1743921306000202

Burrows D. N., et al., 2005, Space Sci. Rev., 120, 165

Buxton M. M., Bailyn C. D., 2004, ApJ, 615, 880

Cadolle Bel M., et al., 2007, ApJ, 659, 549

Cannizzo J. K., 1993, ApJ, 419, 318

Cardelli J. A., Clayton G. C., Mathis J. S., 1989, ApJ, 345, 245

Carter P. J., et al., 2013, MNRAS, 431, 372

Casares J., 2015, ApJ, 808, 80

Casares J., Charles P. A., 1992, MNRAS, 255, 7

Casares J., Charles P. A., 1994, MNRAS, 271, L5

Casares J., Jonker P., 2014, Space Science Reviews, 183, 223

Casares J., Charles P. A., Naylor T., 1992, Nature, 355, 614

Casares J., Charles P. A., Naylor T., Pavlenko E. P., 1993, MNRAS, 265, 834

Casares J., Marsh T. R., Charles P. A., Martin A. C., Martin E. L., Harlaftis E. T., Pavlenko E. P., Wagner R. M., 1995, MNRAS, 274, 565

Casares J., Steeghs D., Hynes R. I., Charles P. A., O'Brien K., 2003, ApJ, 590, 1041

Casares J., Cornelisse R., Steeghs D., Charles P. A., Hynes R. I., O'Brien K., Strohmayer T. E., 2006, MNRAS, 373, 1235

Castor J. I., Abbott D. C., Klein R. I., 1975, ApJ, 195, 157

Chabrier G., Baraffe I., Leconte J., Gallardo J., Barman T., 2009, in Stempels E., ed., AIP Conf. Ser. Vol. 1094, The mass-radius relationship from solar-type stars to terrestrial planets: a review. pp 102–111 (`arXiv:0810.5085`), doi:10.1063/1.3099078

Chakrabarty D., Morgan E. H., 1998, Nature, 394, 346

Chandrasekhar S., 1931, MNRAS, 91, 456

Chandrasekhar S., 1935, MNRAS, 95, 207

Charles P. A., Coe M. J., 2006, in Lewin W. H. G., van der Klis M., eds, Compact stellar X-ray sources. Cambridge Univ. Press, p. 215

Charles P., Kotze M., Rajoelimanana A., 2010, in Kologera V., van der Sluys M., eds, AIP Conf. Ser. Vol. 1314, Long-Term Optical/X-ray Variability of CVs, LMXBs and BeX Sources. pp 303–311, doi:10.1063/1.3536392

Charles P., Cornelisse R., Foster D., Casares J., Kotze M., Zdziarski A., 2012, ATel, 4105, 1

Chiang C. Y., Done C., Still M., Godet O., 2010, MNRAS, 403, 1102

Conner J. P., Evans W. D., Belian R. D., 1969, ApJ, 157, L157

Corbel S., Nowak M. A., Fender R. P., Tzioumis A. K., Markoff S., 2003, A&A, 400, 1007

Corbel S., Coriat M., Brocksopp C., Tzioumis A. K., Fender R. P., Tomsick J. A., Buxton M. M., Bailyn C. D., 2013, MNRAS, 428, 2500

Corbet R. H. D., 1984, A&A, 141, 91

Coriat M., et al., 2011, MNRAS, 414, 677

Coriat M., Fender R. P., Dubus G., 2012, MNRAS, 424, 1991

Cornelisse R., Casares J., Muñoz-Darias T., Steeghs D., Charles P., Hynes R., O'Brien K., Barnes A., 2008, in Bandyopadhyay R. M., Wachter S., Gelino D., Gelino C. R., eds, AIP Conf. Ser. Vol. 1010, A Population Explosion: The Nature & Evolution of X-ray Binaries in Diverse Environments. pp 148–152 (arXiv:0801.3367), doi:10.1063/1.2945024

Corral-Santana J. M., Casares J., Muñoz-Darias T., Rodríguez-Gil P., Shahbaz T., Torres M. A. P., Zurita C., Tyndall A. A., 2013, Science, 339, 1048

Corral-Santana J. M., Casares J., Muñoz-Darias T., Bauer F. E., Martínez-Pais I. G., Russell D. M., 2016, A&A, 587, A61

Crawford S. M., et al., 2010, in Society of Photo-Optical Instrumentation Engineers (SPIE) Conference Series. p. 25, doi:10.1117/12.857000

Cumming A., 2003, ApJ, 595, 1077

Dauser T., García J., Parker M. L., Fabian A. C., Wilms J., 2014, MNRAS, 444, L100

Davidson K., Ostriker J. P., 1973, ApJ, 179, 585

Davis S. W., Hubeny I., 2006, ApJS, 164, 530

Díaz Trigo M., Migliari S., Miller-Jones J. C. A., Guainazzi M., 2014, A&A, 571, A76

Done C., Gierliński M., Kubota A., 2007, A&A Rev., 15, 1

Dubus G., Hameury J.-M., Lasota J.-P., 2001, A&A, 373, 251

Durant M., Gandhi P., Shahbaz T., Peralta H. H., Dhillon V. S., 2009, MNRAS, 392, 309

Elvis M., Page C. G., Pounds K. A., Ricketts M. J., Turner M. J. L., 1975, Nature, 257, 656

Esin A. A., McClintock J. E., Narayan R., 1997, ApJ, 489, 865

Evans P. A., et al., 2007, A&A, 469, 379

Fabian A. C., Miniutti G., 2005, ArXiv Astrophysics e-prints,

Fabian A. C., Ross R. R., 2010, Space Sci. Rev., 157, 167

Fabian A. C., Rees M. J., Stella L., White N. E., 1989, MNRAS, 238, 729

Farr W. M., Sravan N., Cantrell A., Kreidberg L., Bailyn C. D., Mandel I., Kalogera V., 2011, ApJ, 741, 103

Faulkner J., 1971, ApJ, 170, L99

Fender R., 2010, in Belloni T., ed., Lecture Notes in Physics, Berlin Springer Verlag Vol. 794, Lecture Notes in Physics, Berlin Springer Verlag. p. 115 (`arXiv:0909.2572`), doi:10.1007/978-3-540-76937-8˙5

Fender R., et al., 1999, ApJ, 519, L165

Fender R. P., Belloni T. M., Gallo E., 2004, MNRAS, 355, 1105

Fender R., Garrington S., Muxlow T., 2005, ATel, 558, 1

Fenimore E. E., Cannon T. M., 1978, Appl. Opt., 17, 337

Ferrigno C., et al., 2015a, The Astronomer's Telegram, 7662

Ferrigno C., Bozzo E., Boissay R., Kuulkers E., Kretschmar P., 2015b, The Astronomer's Telegram, 7731

Foulkes S. B., Haswell C. A., Murray J. R., 2006, MNRAS, 366, 1399

Foulkes S. B., Haswell C. A., Murray J. R., 2010, MNRAS, 401, 1275

Fragile P. C., Mathews G. J., Wilson J. R., 2001, ApJ, 553, 955

Fridriksson J. K., Homan J., Remillard R. A., 2015, ApJ, 809, 52

Froning C. S., Maccarone T. J., France K., Winter L., Robinson E. L., Hynes R. I., Lewis F., 2014, ApJ, 780, 48

Fryer C. L., Kalogera V., 2001, ApJ, 554, 548

Fürst F., et al., 2015, ApJ, 808, 122

Gallo E., 2015, in Contopoulos I., Gabuzda D., Kylafis N., eds, Astrophysics and Space Science Library Vol. 414, The Formation and Disruption of Black Hole Jets. p. 25, doi:10.1007/978-3-319-10356-3˙2

Gallo E., Fender R. P., Pooley G. G., 2003, MNRAS, 344, 60

Gallo E., Fender R. P., Miller-Jones J. C. A., Merloni A., Jonker P. G., Heinz S., Maccarone T. J., van der Klis M., 2006, MNRAS, 370, 1351

Gallo E., et al., 2014, MNRAS, 445, 290

Gandhi P., et al., 2016, MNRAS, 459, 554

García J., et al., 2014, ApJ, 782, 76

Gazeas K., Vasilopoulos G., Petropoulou M., Sapountzis K., 2015, The Astronomer's Telegram, 7650

Gehrels N., et al., 2004, ApJ, 611, 1005

Gelino D. M., Harrison T. E., 2003, ApJ, 599, 1254

George I. M., Fabian A. C., 1991, MNRAS, 249, 352

Giacconi R., Gursky H., Paolini F. R., Rossi B. B., 1962, Physical Review Letters, 9, 439

Giacconi R., Kellogg E., Gorenstein P., Gursky H., Tananbaum H., 1971, ApJ, 165, L27

Gierliński M., Done C., Page K., 2008, MNRAS, 388, 753

Gierliński M., Done C., Page K., 2009, MNRAS, 392, 1106

Glasser C. A., Odell C. E., Seufert S. E., 1994, IEEE Transactions on Nuclear Science, 41, 1343

González Hernández J. I., Rebolo R., Casares J., 2012, ApJ, 744, L25

Greiner J., Rau A., Schady P., 2012, The Astronomer's Telegram, 4030, 1

Gruber D. E., Blanco P. R., Heindl W. A., Pelling M. R., Rothschild R. E., Hink P. L., 1996, A&AS, 120, 641

Halpern J. P., 2005, ATel, 549, 1

Hameury J.-M., Lasota J.-P., McClintock J. E., Narayan R., 1997, ApJ, 489, 234

Harries J. R., McCracken K. G., Francey R. J., Fenton A. G., 1967, Nature, 215, 38

Harrison F. A., et al., 2013, ApJ, 770, 103

Hasinger G., van der Klis M., 1989, A&A, 225, 79

Hiemstra B., Soleri P., Méndez M., Belloni T., Mostafa R., Wijnands R., 2009, MNRAS, 394, 2080

Horne K., 1986, PASP, 98, 609

Horne K., Marsh T. R., 1986, MNRAS, 218, 761

Hynes R. I., et al., 2004, ApJ, 611, L125

Hynes R. I., Brien K. O., Mullally F., Ashcraft T., 2009a, MNRAS, 399, 281

Hynes R. I., Bradley C. K., Rupen M., Gallo E., Fender R. P., Casares J., Zurita C., 2009b, MNRAS, 399, 2239

Ingram A., Done C., Fragile P. C., 2009, MNRAS, 397, L101

Jain R. K., Bailyn C. D., Orosz J. A., McClintock J. E., Remillard R. A., 2001, ApJ, 554, L181

Jansen F., et al., 2001, A&A, 365, L1

Jethwa P., Saxton R., Guainazzi M., Rodriguez-Pascual P., Stuhlinger M., 2015, A&A, 581, A104

Jordan S., 2008, Astronomische Nachrichten, 329, 875

Kalemci E., Dinçer T., Tomsick J. A., Buxton M. M., Bailyn C. D., Chun Y. Y., 2013, ApJ, 779, 95

Kalogera V., Baym G., 1996, ApJ, 470, L61

Kaur R., et al., 2012, ApJ, 746, L23

Kennea J. A., et al., 2012a, The Astronomer's Telegram, 4034, 1

Kennea J. A., et al., 2012b, ATel, 4044, 1

Khargharia J., Froning C. S., Robinson E. L., 2010, ApJ, 716, 1105

Khargharia J., Froning C. S., Robinson E. L., Gelino D. M., 2013, AJ, 145, 21

King A. R., Kolb U., Burderi L., 1996, ApJ, 464, L127

Kirsch M. G. F., et al., 2006, A&A, 453, 173

Knigge C., Baraffe I., Patterson J., 2011, ApJS, 194, 28

Kochanek C. S., 2014, MNRAS, 444, 2043

Körding E. G., Fender R. P., Migliari S., 2006, MNRAS, 369, 1451

Kotze M. M., Charles P. A., 2012, MNRAS, 420, 1575

Kreidberg L., Bailyn C. D., Farr W. M., Kalogera V., 2012, ApJ, 757, 36

Krimm H. A., et al., 2008, ATel, 1599, 1

Kubota A., Tanaka Y., Makishima K., Ueda Y., Dotani T., Inoue H., Yamaoka K., 1998, PASJ, 50, 667

Kudoh T., Matsumoto R., Shibata K., 2002, PASJ, 54

Kuulkers E., 1998, New A Rev., 42, 1

Kuulkers E., et al., 2013, A&A, 552, A32

La Dous C., 1989, A&A, 211, 131

Lasota J.-P., 2001, New A Rev., 45, 449

Lasota J.-P., Dubus G., Kruk K., 2008, A&A, 486, 523

Lattimer J. M., Prakash M., 2005, Physical Review Letters, 94, 111101

Lépine S., Gaidos E., 2011, AJ, 142, 138

Lewis F., Roche P., Russell D. M., Fender R. P., 2008, in Bandyopadhyay R. M., Wachter S., Gelino D., Gelino C. R., eds, American Institute of Physics Conference Series Vol. 1010, A Population Explosion: The Nature & Evolution of X-ray Binaries in Diverse Environments. pp 204–206 (`arXiv:0712.2751`), doi:10.1063/1.2945042

Lewis F., Street R., Roche P., Stroud V., Russell D. M., 2010, Adv. Astron, 2010

Li L.-X., Zimmerman E. R., Narayan R., McClintock J. E., 2005, ApJS, 157, 335

Lightman A. P., White T. R., 1988, ApJ, 335, 57

Liu B. F., Meyer F., Meyer-Hofmeister E., 2006, A&A, 454, L9

Livio M., Pringle J. E., King A. R., 2003, ApJ, 593, 184

Lomb N. R., 1976, Ap&SS, 39, 447

Lynden-Bell D., 2003, MNRAS, 341, 1360

Maccarone T. J., 2003, A&A, 409, 697

Makino F., 1989, IAU Circ., 4782

Marsh T. R., Horne K., 1988, MNRAS, 235, 269

Marsh T. R., Robinson E. L., Wood J. H., 1994, MNRAS, 266, 137

Mata Sánchez D., Muñoz-Darias T., Casares J., Corral-Santana J. M., Shahbaz T., 2015, MNRAS, 454, 2199

Matsuoka M., et al., 2009, PASJ, 61, 999

McClintock J. E., Remillard R. A., 2006, in Lewin W. H. G., van der Klis M., eds, Compact stellar X-ray sources. Cambridge Univ. Press, p. 157

McClintock J. E., Canizares C. R., Tarter C. B., 1975, ApJ, 198, 641

McMullin J. P., Waters B., Schiebel D., Young W., Golap K., 2007, in Shaw R. A., Hill F., Bell D. J., eds, Astronomical Society of the Pacific Conference Series Vol. 376, Astronomical Data Analysis Software and Systems XVI. p. 127

Meier D. L., Koide S., Uchida Y., 2001, Science, 291, 84

Merloni A., Heinz S., di Matteo T., 2003, MNRAS, 345, 1057

Meyer-Hofmeister E., Liu B. F., Meyer F., 2012, A&A, 544, A87

Meyer F., Liu B. F., Meyer-Hofmeister E., 2007, A&A, 463, 1

Miller-Jones J. C. A., Jonker P. G., Dhawan V., Brisken W., Rupen M. P., Nelemans G., Gallo E., 2009, ApJ, 706, L230

Mitsuda K., et al., 1984, PASJ, 36, 741

Mitsuda K., et al., 2007, PASJ, 59, 1

Mooley K., Fender R., Anderson G., Staley T., Kuulkers E., Rumsey C., 2015, The Astronomer's Telegram, 7658

Morgan E., Swank J., Markwardt C., Gehrels N., 2005, ATel, 550, 1

Muñoz-Darias T., Casares J., Martínez-Pais I. G., 2005, ApJ, 635, 502

Muñoz-Darias T., et al., 2016, Nature, 534, 75

Munoz-Darias T., Sanchez D. M., Casares J., Shaw A. W., Charles P. A., Ferragamo A., Rubino-Martin J. A., 2015, The Astronomer's Telegram, 7659, 1

Narayan R., Yi I., 1995a, ApJ, 444, 231

Narayan R., Yi I., 1995b, ApJ, 452, 710

Narayan R., McClintock J. E., Yi I., 1996, ApJ, 457, 821

Negoro H., et al., 2009, ATel, 2341, 1

Negoro H., et al., 2015, The Astronomer's Telegram, 7646

Neustroev V. V., Veledina A., Poutanen J., Zharikov S. V., Tsygankov S. S., Sjoberg G., Kajava J. J. E., 2014, MNRAS, 445, 2424

Neustroev V. V., et al., 2015, The Astronomer's Telegram, 7697

Oda M., 1965, Appl. Opt., 4, 143

Ogilvie G. I., Dubus G., 2001, MNRAS, 320, 485

Oke J. B., 1990, AJ, 99, 1621

Onodera T., et al., 2015, The Astronomer's Telegram, 7196, 1

Oppenheimer J. R., Volkoff G. M., 1939, Physical Review, 55, 374

Orosz J. A., Bailyn C. D., 1995, ApJ, 446, L59

Orosz J. A., Bailyn C. D., 1997, ApJ, 477, 876

Orosz J. A., Bailyn C. D., Remillard R. A., McClintock J. E., Foltz C. B., 1994, ApJ, 436, 848

Orosz J. A., Remillard R. A., Bailyn C. D., McClintock J. E., 1997, ApJ, 478, L83

Orosz J. A., et al., 2001, ApJ, 555, 489

Özel F., Psaltis D., Narayan R., McClintock J. E., 2010, ApJ, 725, 1918

Özel F., Psaltis D., Narayan R., Santos Villarreal A., 2012, ApJ, 757, 55

Pacini F., 1967, Nature, 216, 567

Palmer D. M., Barthelmey S. D., Cummings J. R., Gehrels N., Krimm H. A., Markwardt C. B., Sakamoto T., Tueller J., 2005, ATel, 546, 1

Patterson J., et al., 2005, PASP, 117, 1204

Pauli W., 1925, Zeitschrift für Physik, 31, 765

Perley R. A., Butler B. J., 2013, ApJS, 206, 16

Perlmutter S., et al., 1997, ApJ, 483, 565

Perrott Y. C., et al., 2013, MNRAS, 429, 3330

Pfeffermann E., et al., 1987, in Soft X-ray optics and technology. p. 519

Ponti G., Fender R. P., Begelman M. C., Dunn R. J. H., Neilsen J., Coriat M., 2012, MNRAS, 422, L11

Ramadevi M. C., Seetha S., 2007, MNRAS, 378, 182

Reid M. J., McClintock J. E., Narayan R., Gou L., Remillard R. A., Orosz J. A., 2011, ApJ, 742, 83

Reid M. J., McClintock J. E., Steiner J. F., Steeghs D., Remillard R. A., Dhawan V., Narayan R., 2014, ApJ, 796, 2

Reis R. C., Fabian A. C., Ross R. R., Miller J. M., 2009, MNRAS, 395, 1257

Remillard R. A., Muno M. P., McClintock J. E., Orosz J. A., 2002, ApJ, 580, 1030

Reynolds C. S., Fabian A. C., Makishima K., Fukazawa Y., Tamura T., 1994, MNRAS, 268, L55

Riess A. G., et al., 1998, AJ, 116, 1009

Rodriguez J., et al., 2015, A&A, 581, L9

Roming P. W. A., et al., 2005, Space Sci. Rev., 120, 95

Ross R. R., Fabian A. C., 2005, MNRAS, 358, 211

Rushton A., Spencer R., Fender R., Pooley G., 2010, A&A, 524, A29

Rushton A., et al., 2012, MNRAS, 419, 3194

Russell D. M., Miller-Jones J. C. A., Maccarone T. J., Yang Y. J., Fender R. P., Lewis F., 2011, ApJ, 739, L19

Sato R., et al., 2012, ATel, 4024, 1

Scargle J. D., 1982, ApJ, 263, 835

Schreier E., Levinson R., Gursky H., Kellogg E., Tananbaum H., Giacconi R., 1972, ApJ, 172, L79

Schwarzschild K., 1916b, in Sitzungsberichte der Königlich Preussischen Akademie der Wissenschaften zu Berlin, Phys.-Math. Klasse, 424-434 (1916).

Schwarzschild K., 1916a, Sitzungsberichte der Königlich Preußischen Akademie der Wissenschaften (Berlin), 1916, Seite 189-196,

Seward F. D., Charles P. A., 2010, Exploring the X-ray Universe, 2 edn. Cambridge Univ. Press

Shahbaz T., Ringwald F. A., Bunn J. C., Naylor T., Charles P. A., Casares J., 1994, MNRAS, 271, L10

Shahbaz T., Bandyopadhyay R. M., Charles P. A., Wagner R. M., Muhli P., Hakala P., Casares J., Greenhill J., 1998, MNRAS, 300, 1035

Shahbaz T., Dhillon V. S., Marsh T. R., Zurita C., Haswell C. A., Charles P. A., Hynes R. I., Casares J., 2003, MNRAS, 346, 1116

Shakura N. I., Sunyaev R. A., 1973, A&A, 24, 337

Shaw A. W., et al., 2013, MNRAS, 433, 740

Shaw A. W., Charles P. A., Gandhi P., Altamirano D., 2015, The Astronomer's Telegram, 7216, 1

Shidatsu M., et al., 2013, ApJ, 779, 26

Shih I. C., Bird A. J., Charles P. A., Cornelisse R., Tiramani D., 2005, MNRAS, 361, 602

Shih I. C., Charles P. A., Cornelisse R., 2011, MNRAS, 412, 120

Shimura T., Takahara F., 1995, ApJ, 445, 780

Smak J., 1981, Acta Astron., 31, 395

Smartt S. J., Eldridge J. J., Crockett R. M., Maund J. R., 2009, MNRAS, 395, 1409

Smith J. F., Courtier G. M., 1976, Proceedings of the Royal Society of London Series A, 350, 421

Soleri P., et al., 2010, MNRAS, 406, 1471

Soleri P., et al., 2013, MNRAS, 429, 1244

Staley T. D., Anderson G. E., 2015a, chimenea: Multi-epoch radio-synthesis data imaging, Astrophysics Source Code Library (ascl:1504.005)

Staley T. D., Anderson G. E., 2015b, Astronomy and Computing, 13, 38

Steeghs D., Casares J., 2002, ApJ, 568, 273

Steiner J. F., Narayan R., McClintock J. E., Ebisawa K., 2009, PASP, 121, 1279

Stellingwerf R. F., 1978, ApJ, 224, 953

Still M., Roming P., Brocksopp C., Markwardt C. B., 2005, ATel, 553, 1

Strüder L., et al., 2001, A&A, 365, L18

Swank J. H., Becker R. H., Boldt E. A., Holt S. S., Pravdo S. H., Serlemitsos P. J., 1977, ApJ, 212, L73

Swinbank J. D., et al., 2015, Astronomy and Computing, 11, 25

Tanaka Y., Inoue H., Holt S. S., 1994, PASJ, 46, L37

Tauris T. M., van den Heuvel E. P. J., 2006, in Lewin W. H. G., van der Klis M., eds, Compact stellar X-ray sources. pp 623–665

Tody D., 1986, in Crawford D. L., ed., Society of Photo-Optical Instrumentation Engineers (SPIE) Conference Series Vol. 627, Instrumentation in astronomy VI. p. 733

Tolman R. C., 1939, Physical Review, 55, 364

Tomsick J. A., Heindl W. A., Chakrabarty D., Kaaret P., 2002, ApJ, 581, 570

Tomsick J. A., et al., 2008, ApJ, 680, 593

Tomsick J. A., et al., 2014a, ApJ, 780, 78

Tomsick J. A., Yamaoka K., Corbel S., Kalemci E., Migliari S., Kaaret P., 2014b, ApJ, 791, 70

Tomsick J. A., et al., 2015, ApJ, 808, 85

Torres M. A. P., et al., 2002, ApJ, 569, 423

Tudose V., Fender R. P., Linares M., Maitra D., van der Klis M., 2009, MNRAS, 400, 2111

Udalski A., Kaluzny J., 1991, PASP, 103, 198

Uemura M., et al., 2002, PASJ, 54, 285

Ugliano M., Janka H.-T., Marek A., Arcones A., 2012, ApJ, 757, 69

Uttley P., Klein-Wolt M., 2015, MNRAS, 451, 475

Vadawale S. V., Rao A. R., Naik S., Yadav J. S., Ishwara-Chandra C. H., Pramesh Rao A., Pooley G. G., 2003, ApJ, 597, 1023

Verner D. A., Ferland G. J., Korista K. T., Yakovlev D. G., 1996, ApJ, 465, 487

Wade R. A., Horne K., 1988, ApJ, 324, 411

Wagner R. M., Starrfield S. G., Cassatella A., Hurst G. M., Mobberley M., Marsden B. G., 1989, IAU Circ., 4783

Warner B., 1995, Camb. Astrophys. Ser., 28

Weisskopf M. C., Brinkman B., Canizares C., Garmire G., Murray S., Van Speybroeck L. P., 2002, PASP, 114, 1

Whitehurst R., King A., 1991, MNRAS, 249, 25

Wilkinson T., Uttley P., 2009, MNRAS, 397, 666

Wilms J., Allen A., McCray R., 2000, ApJ, 542, 914

Wiringa R. B., Fiks V., Fabrocini A., 1988, Phys. Rev. C, 38, 1010

Wolter H., 1952, Annalen der Physik, 445, 94

Woosley S. E., Taam R. E., 1976, Nature, 263, 101

Wren J., et al., 2001, ApJ, 557, L97

Wu J., Orosz J. A., McClintock J. E., Hasan I., Bailyn C. D., Gou L., Chen Z., 2016, ApJ, 825, 46

Yoshikawa A., Yamada S., Nakahira S., Matsuoka M., Negoro H., Mihara T., Tamagawa T., 2015, PASJ, 67, 11

Zurita C., et al., 2002, MNRAS, 333, 791

Zurita C., Casares J., Hynes R. I., Shahbaz T., Charles P. A., Pavlenko E. P., 2004, MNRAS, 352, 877

Zurita C., et al., 2006, ApJ, 644, 432

Zurita C., Durant M., Torres M. A. P., Shahbaz T., Casares J., Steeghs D., 2008, ApJ, 681, 1458

Zwart J. T. L., et al., 2008, MNRAS, 391, 1545

Życki P. T., Done C., Smith D. A., 1999, MNRAS, 309, 561

van Dokkum P. G., 2001, PASP, 113, 1420

van Paradijs J., McClintock J. E., 1994, A&A, 290

van den Heuvel E. P. J., 1975, ApJ, 198, L109

van der Klis M., 1989, in Ögelman H., van den Heuvel E. P. J., eds, NATO Advanced Science Institutes (ASI) Series C Vol. 262, NATO Advanced Science Institutes (ASI) Series C. p. 27

van der Klis M., 2006, in Lewin W. H. G., van der Klis M., eds, Compact stellar X-ray sources. p. 39